ULAB JOURNAL OF SCIENCE AND ENGINEERING

A RESEARCH PUBLICATION OF ULAB

November 2011 Vol. 2 ISSN: 2079-4398

CONTENTS

Editorial: State of ULAB JSE 1

Fuzzy Logic Based Intelligent Control of FSTP Inverter Fed PMSM Drive 2
Kalyan Kumar Halder, Md. Abdur Rafiq, B.C. Ghosh

Exprimental Analysis of Handover over UDP and TCP in the Integration of IEEE 802.16 and IEEE 802.11 9
Bikash Chandra Singh, Paresh Chandra Barman, Tapan Kumar Godder, Md. Sipon Miah, H M Abdul Awal

Transient Analysis of Commutatorless DC Shunt Motor 14
Mohammad Abdul Mannan, Md. Aminul Islam

Performance Comparison of Different Software Fault Tolerance Methods 20
Md. Nasim Adnan, Mohammod Akbar Kabir, Lutful Karim, Nargis Khan

A Modified and Cost Effective Approach to Extractions of Intersections from High Resolution Satellite Imagery in Different Road Areas 25
Boshir Ahmed and Md. Fayzur

Design and Development of Microcontroller Based Digital pH Meter 31
M. A. A. Mashud, M. A. Masud, Md. Serajul Islam

(Contents Continued on Back Cover)

School of Science & Engineering
UNIVERSITY OF LIBERAL ARTS
BANGLADESH

ULAB JOURNAL OF SCIENCE AND ENGINEERING

Vol. 2, November 2011

(Contents Continued from Front Cover)

Fast Holographic Image Reconstruction using Graphics Processing Unit 35
Mohammad Shorif Uddin, Madeena Sultana, Md. Ziarul Islam

Design and Development of Microcontroller Based Portable Digital Surface Contamination Monitor 42
M. A. A. Mashud, M. R. A. Bhuiyan, M. A. Masud, Md. Serajul Islam

Performance Analysis of Different Propagation Models and Its Correlation with Cellular Mobile Communication Systems 46
M. Mowrin Hossain and P. Mohan

Feature Extraction Clustering in Text Mining using NMF Basis Probability 50
Paresh Chandra Barman, Md. Sipon Miah, Bikash Chandra Singh

A Note for Contributors 57

Copyright Form 58

List of Reviewers 59

ULAB
UNIVERSITY OF LIBERAL ARTS BANGLADESH

House 56, Rd 4/A @ Satmasjid Road Dhanmondi, Dhaka-1209, Bangladesh
Phone: 966-1255, 966-1301, 0171-309-1936. Web: www.ulab.edu.bd

Editorial
State of ULAB JSE

WE are pleased to present the second volume of ULAB's Journal of Science and Engineering (JSE). It's been another successful year for us: this edition presents many exciting developments undertaken by JSE. Since 2010, ULAB's JSE has maintained its position as the most prestigious national publication in the field of science and engineering.

In 2010, 28 papers were submitted for publication, with 10 being accepted (acceptance rate: 35.71%). This year, the number of submissions increased to 30 and following rigorous peer review, 10 papers were accepted (acceptance rate: 33.33%). This year, the clarity of accepted journal papers has been enhanced by a native English speaking copy-editor.

We continuously strive to publish original research that contains elements of technical novelty. The journal's focus is on traditional theoretical and practical applications of physics, mathematics, environmental science, electronics, computer science, information and communication engineering. In addition, we shall gladly accept submissions on emerging technologies and other emerging areas related to the above fields.

In order to continue publishing a high-quality journal, JSE's editorial board seeks excellent contributions containing original research or reviews. Our editorial board works tirelessly to provide contributors with a prompt and thorough review process.

We would like to extend our heartfelt thanks to every author, reviewer and reader for your support and dedication to JSE. We strongly believe that together, we shall elevate this journal to even higher levels of quality, impact and reputation.

Mohammad Shorif Uddin
Editor-in-Chief

Sazzad Hossain
Associate Editor

A.H.M. Asadul Huq
Associate Editor

© 2011 ULAB JSE

Fuzzy Logic Based Intelligent Control of FSTP Inverter Fed PMSM Drive

Kalyan Kumar Halder, Md. Abdur Rafiq, B.C. Ghosh

Abstract— This paper presents an intelligent control system with the Fuzzy Logic Controller (FLC) for vector control of Permanent Magnet Synchronous Motor (PMSM) drive. A rule-based FLC scheme is designed and applied for the speed control of PMSM drive, using the Pulse Width Modulation (PWM) technique. In the proposed control scheme, a Four Switch Three Phase (FSTP) inverter is used instead of the usual Six Switch Three Phase (SSTP) inverter. This reduces the cost of the inverter, switching losses, and the complexity of the control board to generate six PWM signals. Two independent hysteresis current controllers with a suitable hysteresis band are utilized for inverter switching. The PMSM drive system has been developed, analyzed, and validated by simulation in the C++ environment. A comparison of the proposed FLC based PMSM drive with a conventional PI controller system is provided in terms of speed response. The simulation results demonstrate that the proposed system with FLC improves the dynamic performance of the PMSM drive. It also has a faster speed response than the PI controller. The drive system is robust in various operating conditions and perturbations of parameters.

Keywords— FSTP inverter, FLC, intelligent control, PI controller, PMSM

1 Introduction

WITH rapid developments in power electronics, software engineering and materials, PMSM has become a serious competitor to the induction motor and conventional wound rotor synchronous motor [1]. PMSM is widely used in areas such as traction, automobiles, robotics and aerospace technology [2]. It is receiving an increasing amount of attention as a result of its advantageous features, which include high power density, high efficiency, compact size and low noise. Permanent magnet motors are generally classified into two categories [3]: (1) the Surface Permanent Magnet (SPM) motor, where magnets are mounted on the rotor surface, and (2) the Interior Permanent Magnet (IPM) motor, where magnets are mounted inside the rotor. IPM motors have magnetic saliency with quadrature axis (q-axis) inductance higher than the direct axis (d-axis) inductance.

In recent years, research and development projects have focused on cost reduction of PMSM drives system. Reducing the number of power switches from six to four has improved cost-effectiveness, volume-compactness and the reliability of three phase inverters. An AC to AC converter with minimal hardware was developed [4] for the three phase Induction Motor (IM) drive. A cost effective FSTP inverter was proposed for IM drive in [5] and for IPM motor drive in [6]. The authors showed a performance comparison of the FSTP inverter fed drive with SSTP inverter fed drive in terms of speed response and total harmonic distortion of the stator currents. A complete vector control scheme for IM using FSTP inverter was presented [7] for high performance industrial drive systems. The authors verified the entire control scheme using simulation and experiments in a DSP environment.

Conventional PI and PID controllers are widely used as speed controllers in PMSM drives. However to obtain the best results from these controllers, the exact value of the d- and q- axis reactance of the PMSM must be known. In addition, conventional fixed gain PI and PID controllers are highly sensitive to step changes of command speed, parameter variations and load disturbance [8]. Therefore, an intelligent speed controller demands special attention in order to use the PMSM drive in high performance drive systems [9].

As an intelligent control technology, fuzzy logic control provides a systematic method of incorporating human experiences and implementing nonlinear algorithms. These are characterized by a series of linguistic statements into the controller [10]. The performance of a FLC based IM drive was investigated in [11], both theoretically and experimentally, in different dynamic operating conditions. The authors also provide a comparison of a FLC based drive with the conventional PI controller based drive. In [12] FLC was implemented using the field oriented control technique for speed control of the IM drive. This paper demonstrates that FLC offers superior control of motor torque and highly dynamic performance. A simulation study is carried out in [13] to optimize the FLC for PMSM drive. FLC based flux-weakening control of PMSM drive is proposed in [14]. The proposed strategy achieved fast dynamic control performance, as well as parameter insensitivity in the flux-weakening region.

- *Kalyan Kumar Halder, Department of Electrical & Electronic Engineering, Khulna University of Engineering & Technology, Khulna-9203, Bangladesh. E-mail: kalyan_kuet@yahoo.com.*
- *Md. Abdur Rafiq, Department of Electrical & Electronic Engineering, Khulna University of Engineering & Technology, Khulna-9203, Bangladesh. E-mail: mdabdurrafiq2003@yahoo.com.*
- *B.C. Ghosh, Department of Electrical & Electronic Engineering, American International University-Bangladesh, Dhaka-1213, Bangladesh. E-mail: bcgkuet@gmail.com.*

Manuscript received on 18 April 2011 and accepted for publication on 30 April 2011.

© 2011 ULAB JSE

This paper investigates the performance of the FLC based PMSM drive when fed from a FSTP inverter. FLC may improve the transient and steady-state performance of the drive system. In the control strategy, the *q*-axis command current is derived from a rule-based fuzzy controller. The hysteresis controller controls the current, allowing it to follow the command current as closely as possible to the sinusoidal reference. A performance comparison of speed response is provided between the proposed FLC and the conventional PI Controller. The performance of the proposed drive has also been observed for sudden changes in load torque, parameter variations and speed reversal conditions.

2 Mathematical Model of PMSM

A mathematical model of the PMSM is necessary for the proper simulation of the system. The dynamic model of the PMSM in the synchronously rotating *d-q* reference frame is expressed as follows [15]:

$$v_d = Ri_d + pL_d i_d - \omega_r L_q i_q \tag{1}$$

$$v_q = Ri_q + pL_q i_q + \omega_r \psi_f + \omega_r L_d i_d \tag{2}$$

$$\lambda_q = L_q i_q \tag{3}$$

$$\lambda_d = L_d i_d + \psi_f \tag{4}$$

The developed electromagnetic torque is:

$$T_e = \frac{3P_p}{2}(\psi_f i_q + (L_d - L_q) i_d i_q) \tag{5}$$

The mechanical motion of the PMSM is expressed as:

$$T_e = T_L + J_m p\omega_m + B_m \omega_m \tag{6}$$

For dynamic simulation, the model equations of the PMSM must be expressed in state space derivative form as:

$$L_q \frac{di_q}{dt} = v_q - Ri_q - \omega_r L_d i_d - \omega_r \psi_f \tag{7}$$

$$L_d \frac{di_d}{dt} = v_d - Ri_d + \omega_r L_q i_q \tag{8}$$

$$J_m \frac{d\omega_m}{dt} = T_e - T_L - B_m \omega_m \tag{9}$$

And,

$$\omega_r = p_p \cdot \omega_m \tag{10}$$

Where, v_d and v_q = the *dq*- axis stator voltages;
i_d and i_q = the *dq*- axis stator currents;
λ_d and λ_q = the *dq*- axis stator flux linkages;
L_d and L_q = the *dq*- axis inductances;
ψ_f = the permanent magnetic flux linkage;
R = the stator resistance;
ω_r = the angular speed of rotor;
ω_m = the mechanical speed of rotor;
T_e = the electromagnetic torque;
J_m = the motor inertia;
B_m= the motor friction coefficient;
P_p = the number of pole pairs;
$p \equiv d/dt$.

3 FSTP Inverter Model

In the four switch inverter shown in Fig. 1, a three phase system is obtained by connecting the phase 'c' terminal of the stator windings directly to the centre tap of the DC link capacitors. The single phase AC supply is rectified by the front-end rectifier. The capacitors level the output DC voltage. The three phase voltages of the PMSM are expressed as follows [5]:

$$V_a = \frac{V_{dc}}{3}[4S_a - 2S_b - 1] \tag{11}$$

$$V_b = \frac{V_{dc}}{3}[4S_b - 2S_a - 1] \tag{12}$$

$$V_c = \frac{2V_{dc}}{3}[-S_a - S_b + 1] \tag{13}$$

Where, V_{dc} is the maximum voltage across the DC link capacitors; S_a and S_b are the switching logic (either '0' or '1').

If S_a =1 then T_1 is on and T_2 is off
If S_a =0 then T_1 is off and T_2 is on
If S_b =1 then T_3 is on and T_4 is off
If S_b =0 then T_3 is off and T_2 is on

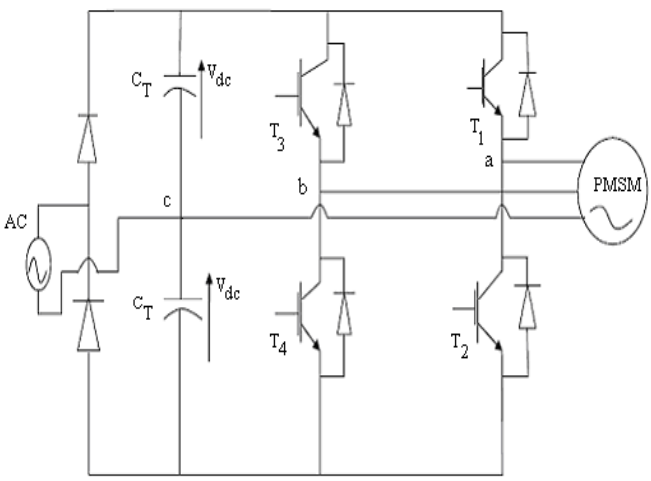

Figure 1: Power Circuit of the FSTP inverter fed PMSM drive

4 Proposed Fuzzy Logic Based Control Scheme

The concept of FLC utilizes the qualitative knowledge of a system to design a practical controller. For a process control system, a fuzzy control algorithm embeds the intuition and experience of an operator designer and researcher.

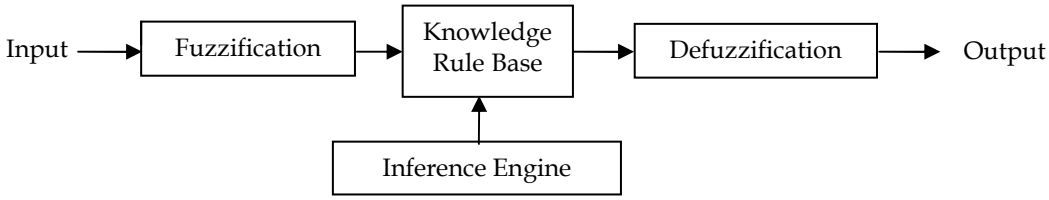

Figure 2: FLC topology

The control does not require an accurate mathematical model of a plant. It is therefore well suited to a process where the model is unknown or ill-defined and particularly to systems with uncertain or complex dynamics [10]. The structure of a complete fuzzy control system is composed of the following blocks: Fuzzification, Knowledge rule base, Inference engine, Defuzzification. Fig. 2 depicts a typical FLC structure.

Figure 3: FLC based command current estimator

The proposed FLC is designed to have two inputs linguistic variables and one output linguistic variable, as shown in Fig. 3. The normalized value of speed error $e_{\omega n}(k)$ and change in speed error $de_{\omega n}(k)$ are the inputs and the normalized value of q- axis reference current $i_{qn}^*(k)$ is the output variable. $e_{\omega n}(k)$ and $de_{\omega n}(k)$ are calculated as follows:

$$e_{\omega n}(k) = \omega_{ref} - \omega_m(k) \tag{14}$$

$$de_{\omega n}(k) = e_{\omega n}(k) - e_{\omega n}(k-1) \tag{15}$$

The crisp variables $e_{\omega n}(k)$ and $de_{\omega n}(k)$ are converted into fuzzy variables $e_{\omega n}$ and $de_{\omega n}$ using the triangular membership functions, as shown in Fig. 4 [11]. The FLC then executes the control rules (Positive Big (PB), Positive Medium (PM), Positive Small (PS), Zero (ZE), Negative Small (NS), Negative Big (NB), Positive (PE), Negative (NE)) shown in Table 1 [11] and processes the output quantity i_{qn}^*.

The complete close loop vector control scheme is contained in Fig. 5. The flux producing component of stator currents i_d^* is set to zero to make the torque equation linear. i_d^* and i_q^* then generate the command currents i_a^* and i_b^*. Two independent hysteresis current controllera with a suitable hysteresis band control the motor currents i_a and i_b follow the command currents. The hysteresis controllers also generate four switching signals, which fire the power semiconductor devices of the three phase inverter to produce the actual voltages to the motor.

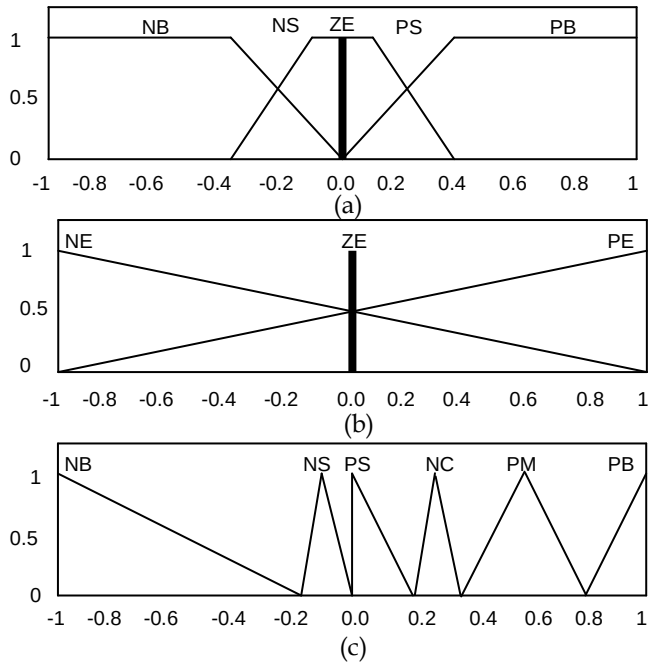

Figure 4: Membership functions for (a) speed error ($e_{\omega n}$) (b) change of speed error ($de_{\omega n}$) and (c) q-axis command current (i_{qn}^*).

TABLE 1
FUZZY CONTROL RULES FOR SPEED CONTROLLER

$de_{\omega n}$ \ $e_{\omega n}$	NB	NS	ZE	PS	PB
NE	NB	NS	NC	PM	PB
ZE	NB	NS	NC	PM	PB
PE	NB	NS	PS	PM	PB

5 SIMULATION RESULTS

Computer simulations were carried out to validate the effectiveness of the proposed drive system under different operating conditions. The system under consideration has been simulated in the C++ environment. The prototype PMSM used in this drive system is a three phase four pole machine, the parameters of which are reported in Table 2.

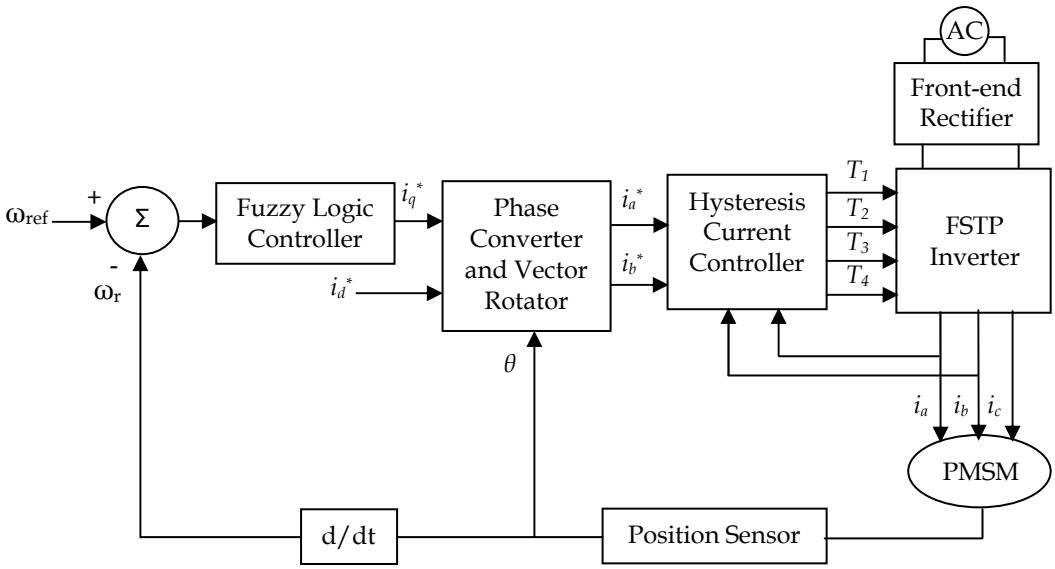

Figure 5: Proposed control scheme of the PMSM

TABLE 2
PMSM SPECIFICATIONS

Phase voltage	145 V
Phase current	3 A
Number of pole pair: P_P	2
Stator resistance: R	5.8 Ω
d-axis inductance: L_d	0.0448 H
q-axis inductance: L_q	0.1024 H
Motor inertia: J_m	0.0087 Kg-m²
Friction coefficient: B_m	0.0008 N-m/rad/sec
Magnetic flux constant: ψ_f	0.533 Volts/rad/sec

5.1 Starting Performance of the PMSM Drive

The motor started with a command speed of 1500 rpm and a load torque of 2.0 N-m from a standstill condition. The speed response curves of the PMSM drive system for both FLC and PI controller are shown in Fig. 6(a).

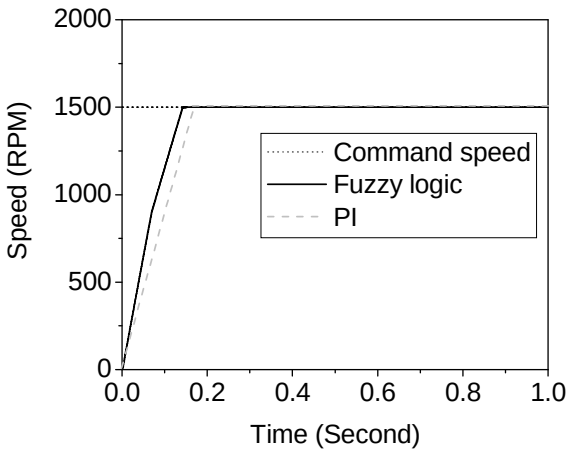

(a)

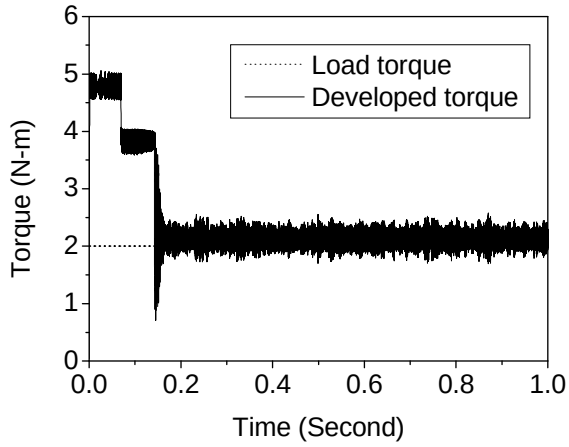

(b)

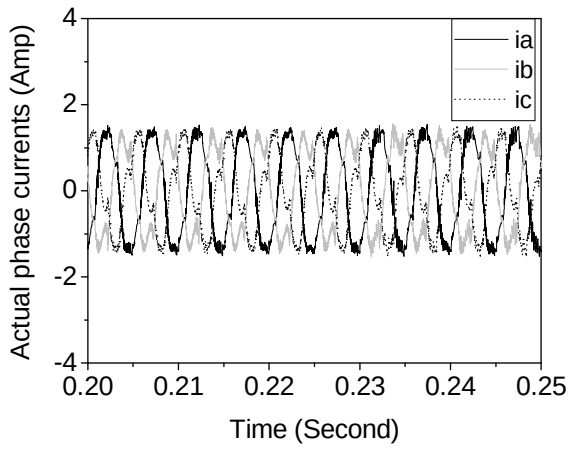

(c)

Figure 6: (a) Simulated speed response, (b) Developed electromagnetic torque, and (c) Steady-state three phase actual currents for the PMSM drive.

It is noted that the motor reached the command speed at t=0.15 second for FLC but at t=0.17 second for PI controller. Therefore FLC provides superior speed response than the conventional PI controller. The actual speed follows the command speed accurately, with negligible steady-state error and oscillations. Fig. 6(b) shows the developed electromagnetic torque of the drive under the starting condition. It is observed that a higher electromagnetic torque is generated during the motor acceleration. Some oscillations in electromagnetic torque are noticeable, due to switching the devices with hysteresis controller. The difference between developed and load torques is due to the viscous damping torque of the drive system. Fig. 6(c) illustrates the three phase actual currents under a steady-state condition.

5.2 Performance under Different Operating Conditions

The performance of the PMSM drive under different operating conditions was also investigated in order to verify the proposed control scheme's robustness. The load torque of the motor was suddenly increased from 2.0 N-m to 3.0 N-m at t=0.5 second. The speed response with change of load is provided in Fig. 7(a). No fall and oscillation in speed was observed as a result of the load torque disturbance. This indicates that the drive system is robust. Fig. 7(b) shows the three phase actual currents under load change conditions. The phase currents increased due to an increase of load torque.

To verify the effect of speed reversal on the drive, command speed was reversed from 1500 rpm to -1500 rpm at t=0.5 second and again to 1500 rpm at t=1.0 second. Fig. 8(a) shows the speed response for different speed sets. It is observed that the drive system follows a linear pattern and requires less time to reach from 1500 rpm to -1500 rpm in comparison to starting condition (0 to +1500 rpm). Fig. 8(b) shows the corresponding developed electromagnetic torque of the PMSM drive.

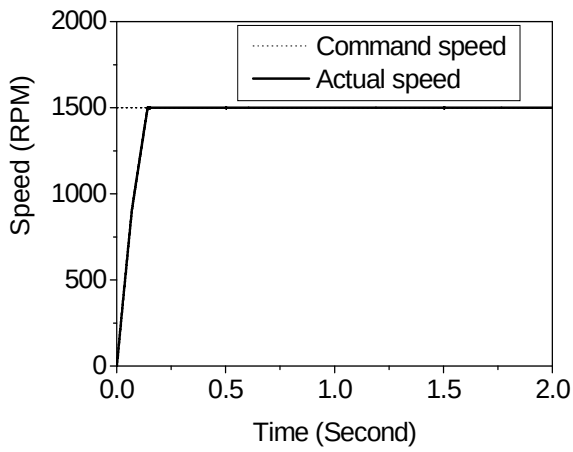

(a)

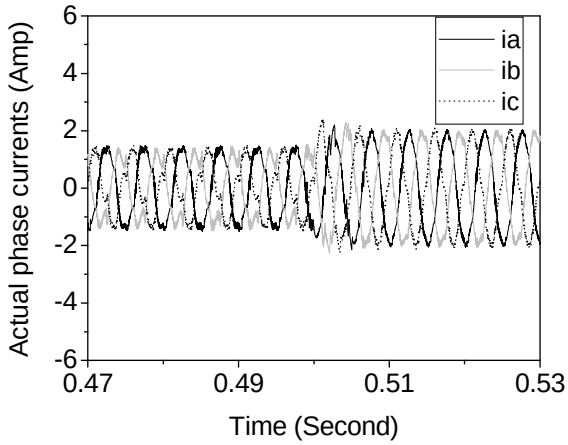

(b)

Figure 7: (a) Simulated speed response, and (b) Three phase actual currents for the PMSM drive for a change of load torque (2.0 N-m to 3.0 N-m).

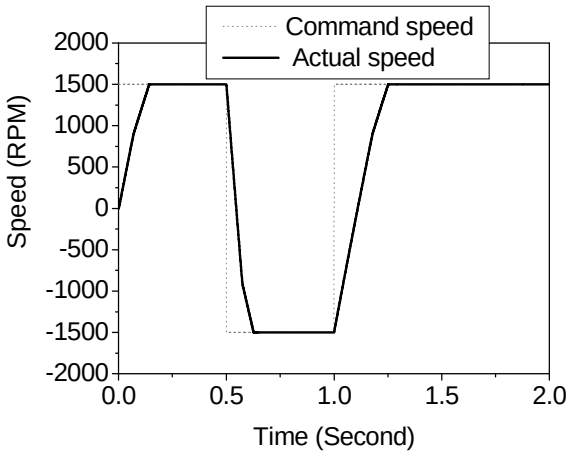

(a)

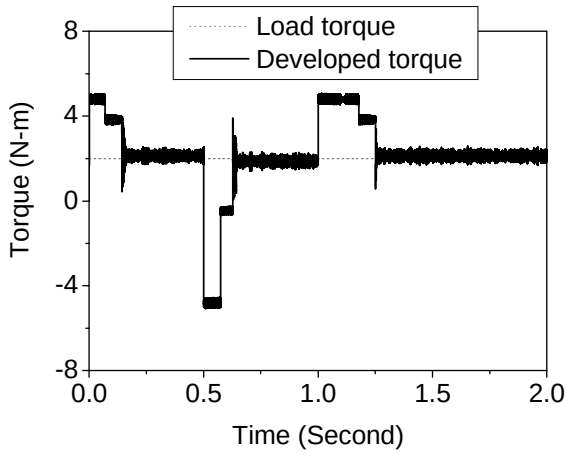

(b)

Figure 8: (a) Simulated speed response, and (b) Developed electromagnetic torque for the PMSM drive for speed reversal condition.

To observe the effects of parameter variations, the motor stator resistance was doubled at t=0.5 second. Fig. 9(a) shows the effect of stator resistance change on speed response. The speed did not drop whatsoever due to a change in stator resistance. Fig. 9(b) illustrates that the rotor angle does not alter due to a change of stator resistance. Thus the drive performance is insensitive to stator parameter variation.

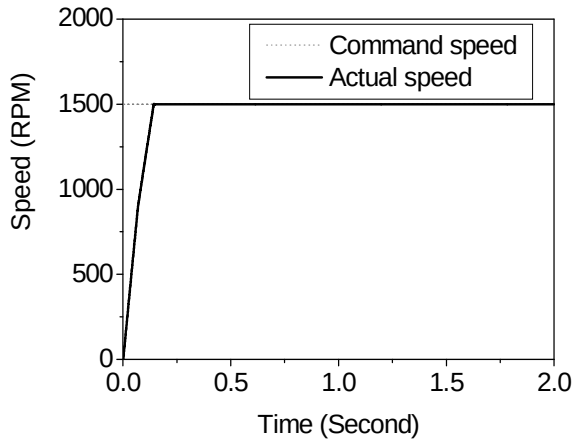

(a)

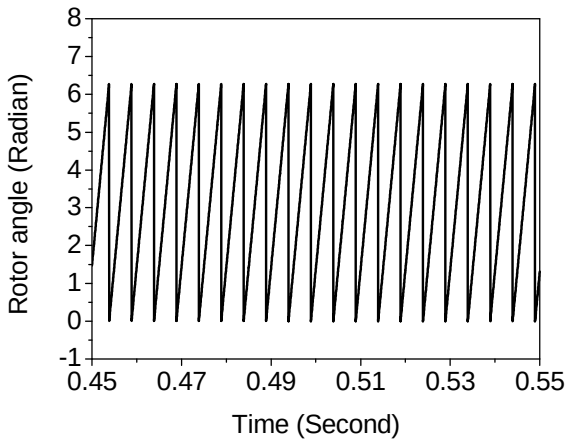

(b)

Figure 9: (a) Simulated speed response, and (b) Rotor angle for the PMSM drive for step change of stator resistance (R to 2R).

6 Conclusions

This study successfully developed a speed control strategy for FSTP inverter fed PMSM drive system. The speed response of the system is better with the FLC than the PI controller, because a fuzzy based control is not dependant on machine equations and performs on the basis of linguistic if-else decisions. The results presented in this work indicate that the proposed control scheme produces a strong dynamic response of the PMSM drive. The drive is also robust to load disturbances, speed reversal, and parameter variation conditions. Therefore, the proposed cost-effective control scheme fulfills the essential requirements for industry applications.

References

[1] M. Kadjoudj, N. Golea, and M.E.H. Benbouzid, "Fuzzy Rule-Based Model Reference Adaptive Control for PMSM Drives," *Serbian Journal of Electrical Engineering*, vol. 4, no. 1, pp. 13-22, June 2007.

[2] A.B. Dehkordi, A.M. Gole, and T.L. Maguire, "Permanent Magnet Synchronous Machine Model for Real-Time Simulation," *Proc. International Conference on Power Systems Transients*, paper no. IPST05-159, June 2005.

[3] B.K. Bose, "A High-Performance Inverter-Fed Drive System of an Interior Permanent Magnet Synchronous Machine," *IEEE Trans. on Industry Applications*, vol. 24, no. 6, pp. 987-997, Nov. /Dec. 1988.

[4] S. Saravanasundaram and K. Thanushkodi, "Compound Active Clamping Boost Converter-Three Phase Four Switch Inverter Fed Induction Motor," *International Journal of Computer Science and Network Security*, vol. 8, no. 8, pp. 358-361, August 2008.

[5] M.N. Uddin, T.S. Radwan, and M.A. Rahman, "Performance Analysis of a Cost Effective 4-Switch, 3-Phase Inverter Fed IM Drive," *Iranian Journal of Electrical and Computer Engineering*, vol. 5, no. 2, pp. 97-102, Summer-Fall 2006.

[6] M.N. Uddin, T.S. Radwan, and M.A. Rahman, "A Cost Effective 4-Switch, 3-Phase Inverter Fed PM Motor Drive," *Proc. International Conference on Electrical & Computer Engineering*, pp. 339-342, December 2004.

[7] P.Q. Dzung, L.M. Phuong, T.C. Binh, and N.M. Hoang, "A Complete Implementation of Vector Control for a Four-Switch Three-Phase Inverter Fed IM Drive," *Proc. International Symposium on Electrical & Electronics Engineering*, pp. 297-301, October 2007.

[8] M.A. Rahman and M.A. Hoque, "On-Line Self-Tuning ANN Based Speed Control of a PM DC Motor," *IEEE/ASME Trans. on Mechatronics*, vol. 2, no. 3, pp. 169-178, September 1997.

[9] M.N. Uddin and M.A. Rahman, "Fuzzy Logic Based Speed Control of an IPM Synchronous Motor Drive," *Journal of Advance Computational Intelligence*, vol. 4, no. 3, pp. 212–219, December 2000.

[10] A.G. Aissaoui, M. Abid, H. Abid, A. Tahour, and A.K. Zeblah, "A Fuzzy Logic Controller for Synchronous Machine," *Journal of Electrical Engineering*, vol. 58, no. 5, pp. 285–290, 2007.

[11] M.N. Uddin, T.S. Radwan, and M.A. Rahman, "Performances of Fuzzy-Logic-Based Indirect Vector Control for Induction Motor Drive," *IEEE Trans. on Industry Applications*, vol. 38, no. 5, pp. 1219–1225, Sep./Oct. 2002.

[12] V. Chitra and R.S. Prabhakar, "Induction Motor Speed Control using Fuzzy Logic Controller," *World Academy of Science, Engineering and Technology*, vol. 23, pp. 17-22, 2006.

[13] K.-C. Yu, S.-P. Hsu and Y.-H. Hung, "Optimization of Fuzzy Controller of Permanent Magnet Synchronous Motor," *Journal of Applied Sciences*, vol. 7, no. 19, pp. 2725-2735, 2007.

[14] X. Cao and L. Fan, "Flux-weakening Control Scheme Based on the Fuzzy Logic of PMSM Drive for Hybrid Electric Vehicle," *Proc. IITA International Conference on Control, Automation and Systems Engineering*, pp. 287-290, July 2009.

[15] D.Y. Ohm, J.W. Brown, and V.B. Chava, "Modeling and Parameter Characterization of Permanent Magnet Synchronous Motors," *Proc. Annual Symposium of Incremental Motion Control Systems and Devices*, pp. 81-86, June 1995.

Kalyan Kumar Halder received his B.Sc. degree in Electrical & Electronic Engineering from Khulna University of Engineering & Technology, Bangladesh in 2008. He is currently a Lecturer at the Department of EEE, KUET, Khulna-9203, Bangladesh. His research interests include power electronics, control system, ANN, fuzzy logic, power system, renewable energy and real time digital simulation.

Md. Abdur Rafiq received his B.Sc. and M.Sc. degrees in Electrical & Electronic Engineering from Bangladesh Institute of Technology (BIT), Khulna, Bangladesh in 1990 and 2001 respectively and Ph.D. degree in Electrical and Electronic Engineering from Khulna University of Engineering & Technology, Khulna, Bangladesh in 2009. He is currently working as a Professor of the Department of EEE, KUET, Khulna-9203, Bangladesh. His research interests include power electronics, machine drives, control system, ANN and fuzzy logic etc.

B.C. Ghosh received his B.Sc. degree in Electrical Engineering from Khulna Engineering College, Bangladesh in 1976, and M.Sc. degree in Electrical & Electronic Engineering from Bangladesh University of Engineering & Technology (BUET), Dhaka in 1986, and a Ph.D. degree in Electrical Engineering from IIT, Kharagpur, India in 1992. At present he is a Professor in the Department of EEE, AIUB, Dhaka-1213, Bangladesh. His research interests include power electronics, machine drives, control system, ANN and fuzzy logic.

Exprimental Analysis of Handover over UDP and TCP in the Integration of IEEE 802.16 and IEEE 802.11

Bikash Chandra Singh, Paresh Chandra Barman, Tapan Kumar Godder, Md. Sipon Miah, H M Abdul Awal

Abstract—One of the goals of a heterogeneous wireless network is to enable service mobility between different wireless networks. Thus this thesis presents seamless and efficient handover performance criteria to enable service mobility in hybrid multi-operator networks of standard technologies IEEE 802.11 (Wi-Fi) and IEEE 802.16 (WiMAX). We optimized the handover procedure for the mobile node using IEEE 802.21, which defines a Media Independent Handover (MIH) function and facilitates handover across heterogeneous access networks during mobility events. We investigated the performance of two handover approaches, one from WiMAX to Wi-Fi and another from Wi-Fi to WiMAX, by evaluating the metrics such as handover latency and throughput when transferring different types of flow, such as TCP (for non real time transmission) and UDP (for real time transmission).

Keywords—WiMAX, Wi-Fi, Heterogeneous Network, Media Independent Handover, TCP, UDP

1 Introduction

4G wireless networks (4GWN) [1] are envisioned as an Internet Protocol (IP) based infrastructure with the integration of various wireless access networks, such as IEEE 802.11 (WLANs), IEEE 802.16 (WMANs), GPRS and UMTS. Heterogeneous wireless networks need to cooperate in order to provide users with seamless mobility and high quality of service (QoS). For example, inexpensive high performance Wi-Fi [2] connectivity will be available within a limited range of "hot-spot" areas and will be complimented with more traditional cellular connectivity offering wide area coverage such as WiMAX [3]. The Transmission Control Protocol (TCP) is a connection oriented, reliable transport layer protocol. On the other hand, the User Datagram Protocol (UDP) is a connectionless protocol and it is less complex and reliable than TCP. The new standard developed by IEEE, explicitly 802.21, provides mobile users better performance during seamless handover than the Media Independent Handover (MIH) framework. Assuming applications can manage mobility and handover to the best network, how heterogeneous handover performs over TCP and UDP is an active area of research.

- *B.C Singh, Information & Communication Engineering Department, Islamic University, Kushtia-7003, Bangladesh. E-mail: bikashsingh18@ yahoo.com.*
- *P.C Barman, Information & Communication Engineering Department, Islamic University, Kushtia-7003, Bangladesh. E-mail: pcb@iceiu.info.*
- *T.K Godder, Information & Communication Engineering Department, Islamic University, Kushtia-7003, Bangladesh. E-mail: tkict@yahoo.com.*
- *Md. S Miah, Information & Communication Engineering Department, Islamic University, Kushtia-7003, Bangladesh. E-mail: mdsipon-miah@gmail.com.*
- *H.M.A Awal, Information & Communication Engineering Department, Islamic University, Kushtia-7003, Bangladesh. E-mail: linkoni-ceiu@gmail.com.*

Manuscript received on 30 July 2011 and accepted for publication on 31 October 2011.

2 Related Works

Research activities carried out on heterogeneous handover context suggests the need for modifications in underlying network architectures. Yongqiang Zhang proposed a vertical handover scheme in [4] between 802.11 and 802.16 wireless access network that performs well, with respect to signaling cost, handover delay, system throughput and packet delay. Z. Daia, R. Fracchiaa et al. [5] proposed a new, realistic approach for vertical handover. This algorithm combines data rate and channel occupancy and can be easily integrated in all 802.11 and 802.16 products. Masanori Yoshimoto et al. [6] has shown that the handoff in the heterogeneous network for TCP-based streaming services have more attention than UDP-based ones. This paper evaluates the handover performance using throughput and handover latency over TCP flow for non-real time data and over UDP for real time data transmission.

3 Wi-Fi and Wimax

3.1 Wi-Fi (IEEE 802.11)

Wi-Fi is established as the world-wide standard that incorporates the use of radio waves to link computers and other network devices. Two layers are defined in the 802.11 standard, the Physical layer and the MAC layer. The Physical layer is responsible for reliably transmitting

© 2011 ULAB JSE

data from one station to another. The MAC layer is used for transmission channel allocation, addressing of Protocol Data Units and frame formatting. Two different physical layer implementations are defined in the 802.11 standard: DSSS/FHSS and OFDM. DSSS/FHSS uses 2.4GHz unlicensed radio spectrum for data rate 11Mbps and OFDM uses 5 GHz radio spectrum for data rate 54 Mbps.

3.2 WiMAX (IEEE802.16)

The IEEE 802.16 Working Group created a new standard, WiMAX, for broadband wireless access at high speeds and low cost, which is easy to deploy. WiMAX original released the 802.16 standard addressed applications in licensed bands in the 10 to 66 GHz frequency range. From 2002 to 2004, the 802.16 working group focused on developing a fixed-broadband non-line-of-sight (NLOS) standard referred to as 802.16a/d. 802.16e standard was recently approved in December 2005. It builds on the 802.16d standard to provide low-mobility (60 Km/h or less) wireless Internet access that uses a Cellular-like handover mechanism to extend the system range.

4 Heterogeneous Seamless handover

4.1 Intregation of WiFi and WiMAX

Transparent roaming for multi-mode subscriber devices between WiMAX and Wi-Fi networks are typically implemented with functionality that includes: Control-plane network: Authentication, Authorization, and Accounting (AAA), AAA proxy and offline and online charging. Data-plane network: Access Service Gateway with DHCP, Foreign Agent (FA), Wireless Access Gateway (WAG), Home Agent (HA), and Packet Data Gateway (PDG) service functionality located in the service provider network. Fig. 1 shows this architecture.

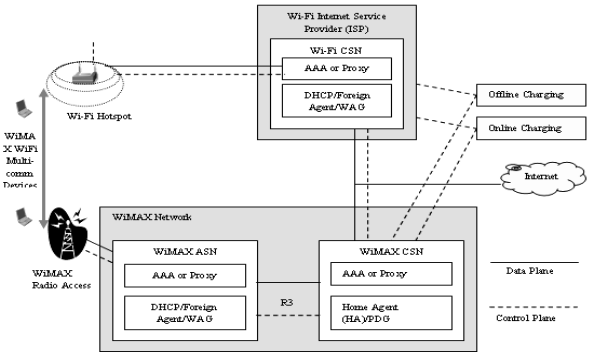

Figure 1: Architecture of roaming

4.2 Media Independent Handover (MIH)

The IEEE 802.21 framework [7] is intended to facilitate handover between heterogeneous access networks. The framework helps mobile devices to discover, characterize, and select networks within their neighborhoods by exchanging information about available link types, link identifiers, and link qualities of nearby network links. The heart of the 802.21 is the Media Independent Handover Function (MIHF) that communicates with access specific lower layer MAC and PHY components, including 802.16, 802.11 and cellular, as well as upper layer entities. In MIH Predictive triggers express a probability of a change in system properties in the future. Event triggers describe an exact event. Link Up and Link Down are examples of event trigger and Link Going Up (LGU) and Link Going Down (LGD) are examples of predictive triggers. Fig. 2 depicts the main triggers identified to assist the handoff process.

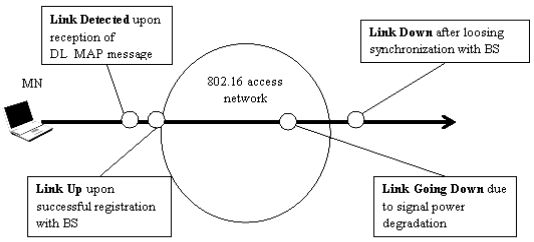

Figure 2: The main triggers in handover process

5 Implementation and Performance Analysis

5.1 Simulation Design

The all-in-one package of the NS-2 does not include support for Mobile WiMAX. Therefore two additional packets from the National Institute of Standards and Technology (NIST), the WiMAX [8] and the Mobility module [9], were installed to achieve simulations of mobile scenarios. The Neighbor Discovery (ND) [10] module provides movement detection for layer 3. Its task is to create IP addresses when a network changes. The scenario in Fig. 3 considered the simulation results, and consists of a Wi-Fi cell located inside a WiMAX cell.

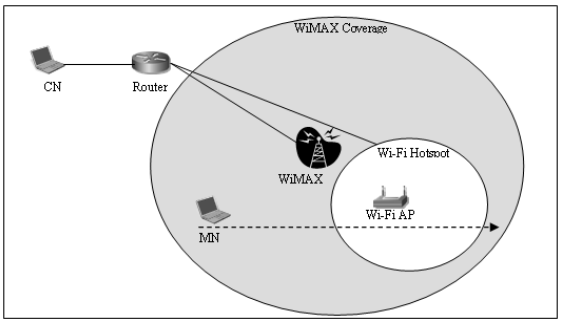

Figure 3: Simulation scenario

It is assumed that one mobile node (MN), equipped with multiple interfaces, is connected to WMAN before passing through the WLAN coverage area. If both the WLAN and the WMAN interfaces are available, it is assumed that the MN uses the WLAN interface for its application flows. Therefore in this scenario, the MN performs two handovers. The first handover from WiMAX to Wi-Fi when the MN enters the coverage area of the Wi-Fi AP and the other from Wi-Fi to WiMAX when the MN leaves the coverage the Wi-Fi AP. To evaluate handover performance we selected different applications. Table-1 summarizes the parameter values used by default in the

simulations. To compare the handover performance of TCP and UDP, we chose two parameters:

Handover Latency: The period during which the MN loses connectivity with its current link until it receives the first IP packet after connecting to the new link is known as handover latency.

Throughput: The ratio between the number of packets originated by the corresponding node and the packets are received by the MN after a handover process is complete.

TABLE1
SIMULATION PARAMETERS

Parameter	Value
WiMAX cell coverage	1000m
Wi-Fi cell coverage	20m
Velocity (m/s)	[1, 5, 10]
Path	Straight line
Application Type	TCP/UDP
Packet size (bytes)	Depends on application

5.2 Performance Analysis Using TCP

TCP uses parameters called congestion window (cwnd) and slow start threshold (ssthresh) to control congestion. The rate used in this simulation is adjusted to 1Mbit/s. Furthermore, the packet size of FTP is set to 1240 and the congestion window is set to 200. In Fig. 4 the left high peaks indicate the handover time from WiMAX to Wi-Fi. The right peaks indicate the handover time from Wi-Fi to WiMAX. From the curve in Fig. 5, we conclude that the higher the speed of the MN, the higher the handover latency. The handover from Wi-Fi to WiMAX also performs better. Here, the LGD generated earlier prevented the drop of the link before the mobile comes out from the AP boundary. This makes redirections of flows easier and faster, without losing the connection. However when the mobile roam with a 5m/s or 10m/s speed, the Link Down is triggered before the drop of the connection.

Fig. 6 establishes that the handover causes growth in packet loss through the indication of two peaks that correspond to the roaming periods. Fig. 7 shows that the throughput of WiMAX to Wi-Fi is lower than Wi-Fi to WiMAX because of WiMAX's higher bandwidth and the lower bandwidth of Wi-Fi.

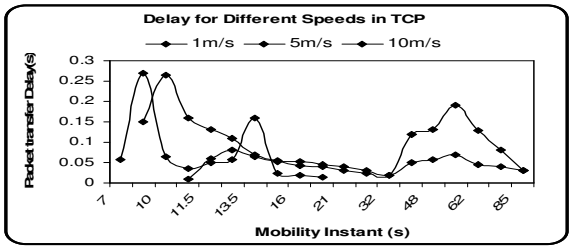

Figure 4. Packet Transfer Delay for TCP

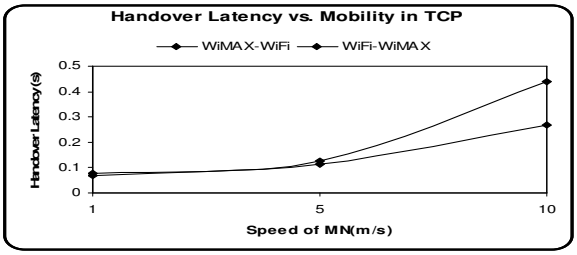

Figure 5: Handover Latency for TCP

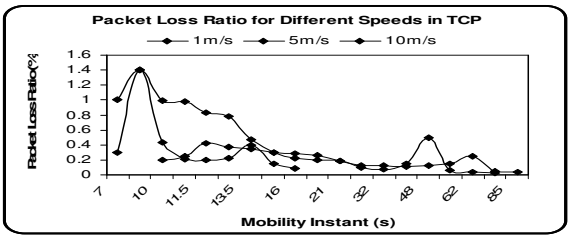

Figure 6: Packet loss Ratio for TCP

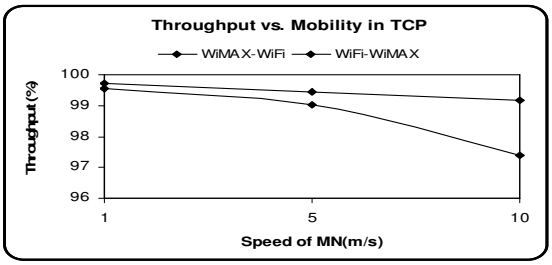

Figure 7: Throughput for TCP

5.3 Performance Analysis Using UDP

UDP performs multicast communications, which allows the development of applications such as network conferencing. In each test, UDP datagram of 1240 bytes was transmitted between the MN and the network. The CBR packet size is 512 bytes. In Fig. 8 the two peaks indicate the two handovers. In addition, the handover period when the MN moves at 1 m/s, grows slowly, while in the case of 5 and 10m/s it reaches a peak. The cause is described in the TCP section. Fig. 9 shows the average delay for a rate of varying MN velocity. We may observe that handover latency is still growing, as is the velocity of the mobile node. The Packet Loss Ratio is obtained in the same phase of simulation, as shown in Fig 10. At the time of the handover, the packet loss ratio is large. In Fig. 11 Wi-Fi to WiMAX handover performs well. UDP support multicast routing, so when MN goes from a small network to a high coverage network, the router can route a buffer packet through any route.

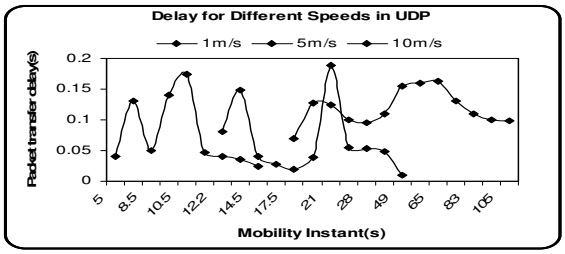

Figure 8: Packet Transfer Delay for UDP

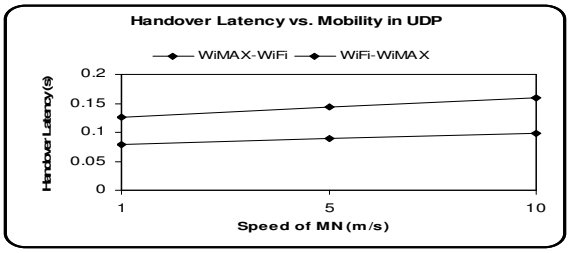

Figure 9: Latency for UDP

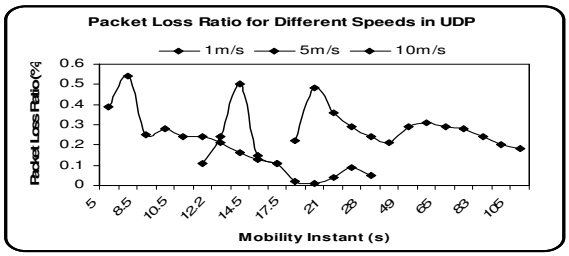

Figure 10. Packet loss Ratio for UDP

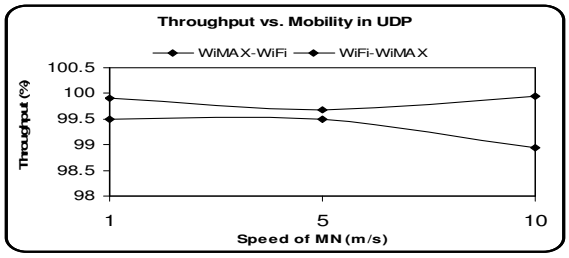

Figure 11. Throughput for UDP

5.4 TCP vs UDP Performance

In Fig. 12 we observe the latency is smaller for UDP flow than for TCP flow. This is because UDP is a much simpler protocol without connection setup delays, flow control, and retransmission. From the plot of Fig. 13 we see that throughput of TCP is not as good as UDP. In TCP, if the handover period is long enough, multiple timeouts will occur when the redirection of flow is complicated. Another effect of vertical handover is a change in the Bandwidth Delay Product (BDP). It is the product of the available bandwidth and latency. If a handover is made from a large BDP network to a small BDP network, congestion occurs because TCP uses a larger window size until congestion forces it to be reduced. On the other hand, a handover from a small BDP to a large BDP network will not take advantage of the large BDP and leads to lower utilisation for some time.

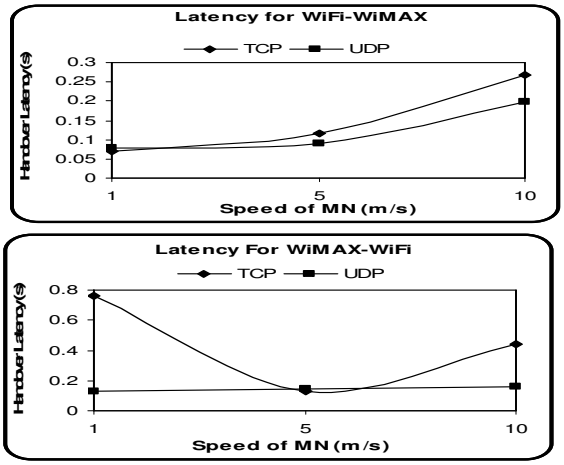

Figure 12. Handover Latency performance for TCP and UDP

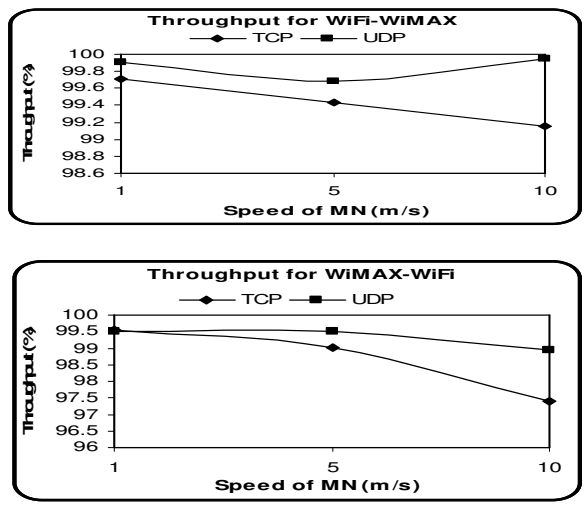

Figure 13: Throughput performance for TCP and UDP

6 Conclusion

For non real time transmission, time is not a factor i.e. the handoff latency is tolerated as the throughput must fulfill the expectation. However the results indicate that during heterogeneous handover, a TCP connection cannot deliver more packets. On the other hand, UDP is a connectionless, unreliable protocol for real time use. Here, the handover latency must be small for live telecast or video conferencing and the interrupted throughput can be ignored. Our analysis exposed UDP as a protocol that can be used for both real time and non-real time applications at vertical handover for heterogeneous networks of Wi-Fi and WiMAX. In future, we have to ensure better QoS in terms of reliability and eliminating jitters for a better performance measurement.

REFERENCES

[1] Allen H. Kupetz and K. Terrell Brown, "4G - A Look into the Future of Wireless Communications", *Rollins Business Journal*, Jan-Mar 2004.

[2] Hp event, "Understanding Wi-FiTM", January 2003.

[3] Caroline Gabriel, "WiMAX: The Critical Wireless Standard" Part of the BluePrint Wi-Fi subscription package.

[4] Yongqiang Zhang, "Vertical Hando_ between 802.11 and 802.16 Wireless Access Networks", *Applied Science in Electrical and Computer Engineering,Waterloo*, Ontario, Canada, 2008.

[5] Z. Dai, R. Fracchia, J. Gosteau, P. Pellati, G. Vivier, "Vertical handover criteria and algorithm in IEEE 802.11 and 802.16 hybrid networks".

[6] Yoshimoto, M.; Kawano, K.; Kinoshita, K.; Matsuda, T.; Murakami, K., "Handoff Performance Enhancement for TCP-based Streaming Services in Heterogeneous Networks" Local Computer Networks, 2007. LCN 2007. 32nd IEEE Conference on Volume , Issue , 15-18 Oct. 2007 Page(s):703 – 710, Digital Object Identifier 10.1109/LCN.2007.91.

[7] Ashutosh Dutta · Subir Das · David Famolari · Yoshihiro Ohba · Kenichi Taniuchi Victor Fajardo · Rafa Marin Lopez · Toshikazu Kodama · Henning Schulzrinne, "Seamless proactive handover across heterogeneous access Networks", *Wireless Pers Commun DOI 10.1007/s11277-007-9266-3, 22* January 2007.

[8] National Institute of Standards and Technology – Draft 1.2.1, "The Network Simulator NS-2 NIST add-on IEEE 802.16 model (MAC+PHY)", January 2009.

[9] National Institute of Standards and Technology, "The Network Simulator NS-2 NIST add-on IEEE 802.21 model (basedon IEEEP802.21/D03.00)", January 2007.

[10] National Institute of Standards and Technology, "The Network Simulator NS-2 NIST add-on Neighbor Discovery", January 2007.

Bikash Chandra Singh received the B.Sc and M.Sc degree in Dept. of Information & Communication engineering from Islamic University, Kushtia, Bangladesh, in 2005 and 2006 respectively. Currently, he is a Lecturer at the Dept. of Information & Communication Engineering, Islamic University, Kushtia, Bangladesh. He is pursuing research in the area of wireless communication. He has published eight international journal papers and one international Conference paper in communication field. His interests are in Wireless Communication, Network Security, WiMAX, and Sensor Network.

Paresh Chandra Barman received a Bachelor's, Master's degree in Applied Physics & Electronics from Rajshahi University, Rajshahi, in 1994 and1995 respectively. He received the Ph.D. degree from the department of Bio and Brain Engineering from Korea Advanced Institute of Science and Technology (KAIST) in 2008. Currently, he is an Associate Professor at the Dept. of Information & Communication Engineering, Islamic University, Kushtia, Bangladesh. His research interests include Neural Network Theory & Application, Pattern Recognition, Artificial Intelligence & Expert Systems, Mathematics for Engineering, Statistics for Communication Engineering, Calculus & Differential Equations and Bioinformatics.

Tapan Kumar Godder received a Bachelor's, Master's and M.Phil degree in Applied Physics & Electronics from Rajshahi University, Rajshahi, in 1994, 1995 and 2007, respectively. He is currently an Associate Professor at the department of ICE, Islamic University, Kushtia-7003, Bangladesh. He has published seventeen papers in international and national journals. His research interests include internetworking, AI & mobile communication.

Md. Sipon Miah received a Bachelor's and Master's Degree from the Department of Information & Communication Engineering from Islamic University, Kushtia, in 2006 and 2007, respectively. He is currently a Lecturer at the department of ICE, Islamic University, Kushtia-7003, Bangladesh. Since 2003, he has served as a Research Scientist at the Communication Research Laboratory, Department of ICE, Islamic University, Kushtia, where he is a member of a spread-spectrum research group. He is pursuing research in internetworking in wireless communication. He has published eight papers in international journals and one in a national journal in the same areas. His areas of interest include database systems, optical fiber communication, Spread Spectrum and mobile communication.

H M Abdul Awal received a B.Sc. and M.Sc. degree in Dept. of Information & Communication engineering from Islamic University, Kushtia, Bangladesh, in 2005 and 2006 respectively. Currently, he is an Assistant Programmer at Sonali Bank Limited Bangladesh. His interests are Wireless Communication, WiMAX, Sensor Network and Ad hoc Networking.

Transient Analysis of Commutatorless DC Shunt Motor

Mohammad Abdul Mannan and Md. Aminul Islam

Abstract − This paper presents a transient analysis of a line commutated inverter (LCI) fed synchronous motor (the equivalent of commutatorless d.c. shunt motor) using rotor position sensor technique. The firing pulses for thyristor of the inverter are generated in proper sequence, with the help of rotor position sensor of the synchronous machine.The transient analytical model of the system was developed using steady state equivalent circuit and vector diagram. The performance characteristic of LCI fed synchronous motor in shunt mode was computed from the mathematical model. The transient characteristics of step changes load (either load applied or load removed) are identified.

Keywords − Rotor Position Sensor, LCI, FORTRAN Power Station, Model of Commutatorless DC Shunt Motor

1 Introduction

RECENTLY, variable speed drives have been widely used in modern industrial fields. From the outset, the conventional DC motor was used as variable speed drives in many industrial applications [1]. However for a reliable system operation, DC motor drives are not recommended in many cases. DC motor drives have several drawbacks, such as brush and commutator wear, which occurs as a result of friction and sparking; power loss, due to both brush contact points; mechanical commutator needs regular maintenance; the commutator construction increases the cost of the DC motor drive; and the mica insulation limits the voltage between commutator segments.

A DC motor can be considered as an AC synchronous machine in which the field is stationary and the armature with its multiphase AC winding is rotating. The armature receives AC power from a DC source through brushes and commutators. The brushes and the commutator constitute an inverter sensitive to the rotor position. Similarly, a synchronous motor may be operated as a DC motor. In a synchronous machine, the field rotates, whereas the armature is stationary. However it should be supplied by an inverter controlled by rotor position sensing signals. The line commutated inverter with rotor position sensitive controller can well be regarded as an electronic commutator, serving the same function as the mechanical commutator. A line commutated inverter (LCI) fed synchronous motor is the most economical, as variable speed drives substitute conventional DC motor drives for a wide range of speeds [2-4]. A synchronous motor supplied by a line commutated inverter acts as a commutatorless DC motors. The drives have several advantages. Synchronous machines are strong, reliable and trouble free. A large volume of research has been undertaken on the series type commutatorless DC motors [6]. However the literature review finds that no steady state and transient analysis have been reported in the field of commutatorless DC shunt motor.

- *Mohammad Abdul Mannan, Department of Electrical and Electronic Engineering at Dhaka University, Gazipur. E-mail mannan489@yahoo.com*
- *Md. Aminul Islam, Department of Electrical and Electronic Engineering at Dhaka University, Gazipur. E-mail aminkeari@yahoo.com*

Manuscript received on 7 March 2011 and accepted for publication on 22 May 2011.

2 System Description

The block diagram of the commutatorless DC shunt motor is shown in Fig.1. It is comprised of an auto transformer, uncontrolled rectifier bridge, DC link smooth inductor, line commutated inverter and a three phase synchronous machine. The uncontrolled rectifier, together with the smoothing inductor, acts as a DC current source. Its output I_{DC} is impressed at the DC input of the machine voltage commutated inverter.

The synchronous machine is interfaced with a DC power supply by a self control variable frequency static inverter, which switches the power to the appropriate stator winding of the synchronous machine. The excitation winding of the synchronous machine is connected to shunt with extra resistance (r_i) to the input of inverter. Therefore the excitation winding is suitable for standard excitation voltages (i.e. 50 volts).To better understand the system operation, the major components are briefly discussed below:

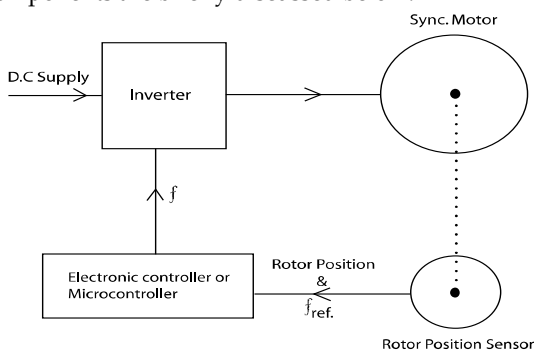

Figure 1: Block Diagram of Commutatorless D.C. Shunt Motor

© 2011 ULAB JSE

(i) Uncontrolled diode bridge

The diode bridge's function is to rectify the fixed frequency AC supply to DC voltage (V_D) and to supply the active power for the synchronous machine.

(ii) DC Link inductor

The variable voltage is applied to the DC link choke, which blocks the voltage ripple and smooths the DC link and suppress the harmonics contained in the output of the bridge rectifier. The DC link inductor acts as a current source.

(iii) Line commutated inverter (LCI)

This is a simple three-phase thyristor inverter bridge. The commutation of inverter thyristor is performed by the voltage induced in the stator winding of the synchronous machine, which is seen by the inverter as a three phase AC source of terminal voltage V_{SY}. The firing angle of the inverter is always greater than 90 degrees and it is measured from the instant of crossing point two phase voltages. It is a self-controlled inverter, which produces variable frequency in accordance to reference frequency (f_{ref}) of rotor position sensor.

(iv) Synchronous Machine

The synchronous machine is conventional and operated as a variable speed machine. The field winding of the machine is connected separately. The machine runs at a synchronous speed that corresponds with the rotor speed. Thus, the inverter frequency is a function of the machine speed. When a synchronous motor operates under steady-load conditions and an additional load is suddenly applied, the developed torque is less than that required by the load, so the motor begins to slow down. A gentle reduction in speed decreases the frequency of the induced e.m.f [3]. The firing control scheme generates the firing pulse for LCI at a new frequency.

(v) Rotor Position Sensor

Rotor position sensor measures the value of the displacement angle between stator pole axis and rotor pole axis of a synchronous machine. It produces an analog signal in respect to displacement angle, in between stator and rotor. The output signal is sent to the controller or microcontroller based firing circuit to produce inverter frequencies.

Brushless derives are basically synchronous motor drives in self-control mode. The armature supply frequency changes in proportion to rotor speed changes, so that the armature field always moves at the same speed as the rotor. Self-control ensures that in all operating points, the armature and rotor fields move at exactly the same speed. This prevents the motor from pulling out of step, hunting oscillations, and the instability which results from a step change in torque or frequency. Accurately tracking speed is usually obtained using a rotor position sensor [1].

(vi) Electronic Control Circuit based or Microcontroller based firing circuit

The rotor position signal is fed to electronic control circuit or microcontroller for firing control of the inverter thyristor in proper sequence.

3 ANALYSIS

In this paper, the steady state performance equation of a commutatorless DC motor is developed. Simple and effective equivalent circuits are presented for commutatorless DC shunt motor system during the conduction and commutation intervals. The performance equation of the commutatorless DC shunt motor was derived using the equivalent circuit (fig.2) and vector diagram (fig.3) [1].The block diagram of the system shown in fig.1 consists of an auto-transformer, an uncontrolled bridge rectifier, a DC link inductor, a line commutated inverter, rotor position sensor and a conventional synchronous machine. The average DC output voltage of the rectifier is controlled by an auto transformer. The three phase uncontrolled bridge rectifier and DC link inductor act as a DC current source for the line commutated inverter. The equivalent circuit diagram of commutatorless shunt motor shown in fig 2 finds the inverter input voltage.

Part−1 (Steady State Analysis)

$$V_{DC} = V_D - I_{DC}\, r_d \qquad (1)$$

General equation of synchronous motor

$$V_{SY} = E_{SY} + I_{sy}\,(R_{SY} + j\,X_S) \qquad (2)$$

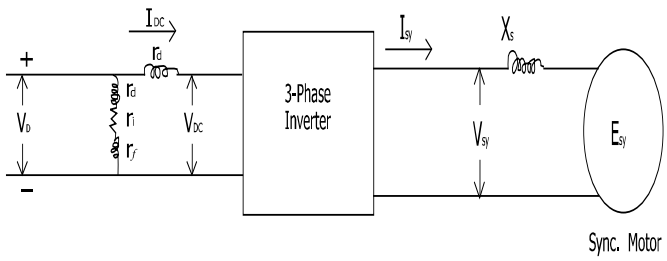

Figure 2: Equivalent Circuit Diagram of Commutatorless Motor

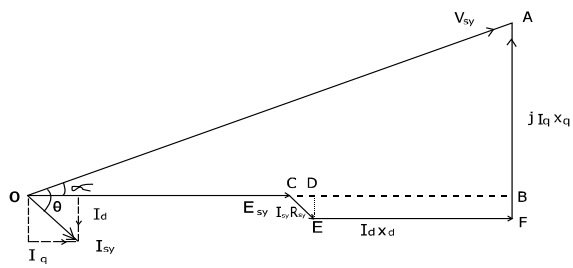

Figure 3 Vector Diagram of Commutatorless D.C Motor

From the vector diagram:

Δ OBA

$(OA)^2 = (OB)^2 + (BA)^2 = (OC+CD+DB)^2 + (FA-FB)^2$

If:

$\gamma = \theta - \alpha$, θ = p. f angle, α = Load angle, $I_d = I_{SY} \sin\gamma$, $I_q = I_{SY} \cos\gamma$

$OA = V_{SY}$, $OC = E_{SY}$, $CD = I_{SY}R_{SY} \cos\gamma$, $DB = EF = I_dX_d$, $FA = I_qX_q$, $FB = ED = I_{SY}R_{SY} \sin\gamma$

Now we get:

$(V_{SY})^2 = (E_{SY} + I_{SY} R_{SY} \cos\gamma + I_d X_d)^2 + (I_q X_q - I_{SY} R_{SY} \sin\gamma)^2$
$(V_{SY})^2 = (E_{SY} + I_{SY} R_{SY} \cos\gamma + I_{SY} X_d \sin\gamma)^2 + (I_{SY} X_q \cos\gamma - I_{SY} R_{SY} \sin\gamma)^2$

$$E_{SY} = \sqrt{(V_{SY})^2 - (I_{SY} X_q Cos\gamma - I_{SY} R_{SY} Sin\gamma)^2} - (I_{SY} R_{sy} Cos\gamma - I_{SY} X_d Sin\gamma) \quad (3)$$

Inverter Relationship [12] & [15]:

$$V_{DC} = \frac{3\sqrt{6}}{\pi} V_{SY} \cos\beta \quad (4)$$

(Commutation reactance is neglected here)

$\beta = 180 - \alpha/$ $\quad \frac{\pi}{2} \leqslant \alpha/ \leqslant \pi$ (for LCI)

Where, V_{DC} = Inverter input voltage
β= Inverter lead angle in electrical degree.
$\alpha/$ = Inverter firing angle in electrical degree.

$$I_{SY} = \frac{\sqrt{6}}{\pi} I_{DC} \quad (5)$$

$OA=V_{SY}$, $OC=E_{SY}$, $CD=I_{SY}R_{SY} \cos\gamma$, $DB=EF=I_dX_d$,

$FA=I_qX_q$, $FB=ED=I_{SY}R_{SY} \sin\gamma$

Now we get:

$(V_{SY})^2 = (E_{SY} + I_{SY} R_{SY} \cos\gamma + I_dX_d)^2 + (I_qX_q - I_{SY} R_{SY} \sin\gamma)^2$
$(V_{SY})^2 = (E_{SY} + I_{SY} R_{SY} \cos\gamma + I_{SY} X_d \sin\gamma)^2 + (I_{SY} X_q \cos\gamma - I_{SY} R_{SY} \sin\gamma)^2$

Here:

Motor capacity is 6 KW (400V, pf 0.8)
No load current of motor, I_{SY}=1.09 A
No Load Inverter input current, I_{DC}=1.40 A [From Eq. 5]
And full load current of motor I_{SY}=10.8253 A
Full load inverter input current I_{DC}=13.8840 A [From Eq. 5]

The speed or frequency of the commutatorless motor is dependent on the rotor position angle. The maximum displacement of the load angle is 20 degrees (elect) [13],[14]. The electronic controller controller circuit requires the calibration of inverter frequency in accordance with the load angle displacement.

Load angle (α)	Inverter output frequency (f)	Current (I_{DC})
0 Degree	50 Hz	1.40A
20 Degree	45 Hz	13.95A

Fig.4-A finds that the relation between inverter frequency (f) and load angle (α) is:

$$f=50-0.25\,\alpha \quad (6)$$

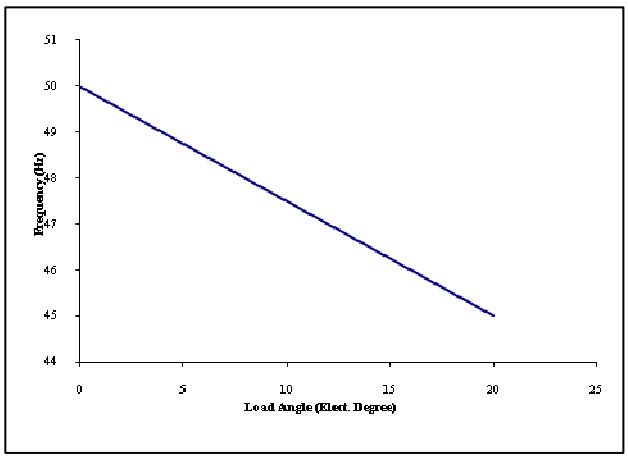

Figure 4.A: Relation between load angle and Frequency

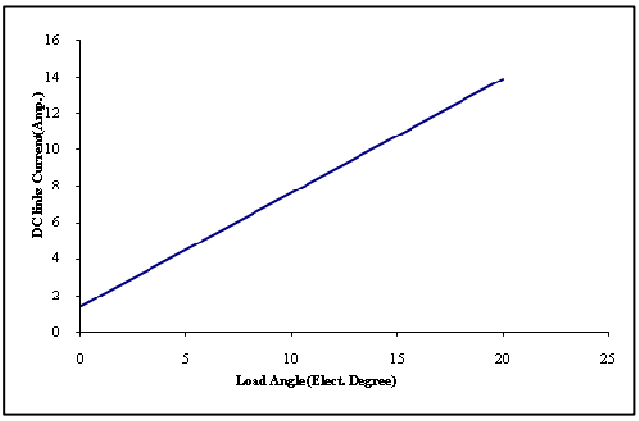

Figure 4.B: Relation between α and IDC

$$X_q = 2\pi f L_q = 2\pi(50 - 0.25\,\alpha)\, L_q \quad (7)$$
$$X_d = 2\pi f L_d = 2\pi(50 - 0.25\,\alpha)\, L_d \quad (8)$$

Where:
X_d = Direct axis reactance of synchronous machine.
X_q = Quadrature axis reactance of synchronous machine.

Fig.4-B finds that the relationship between current (I_{DC}) and load angle (α) is:

$$I_{DC}=1.40 + 0.6242\,\alpha \quad (9)$$

From equations 1 and 4, we have the new equation,

$$V_{SY} = \frac{\pi(V_D - I_{DC} r_d)}{3\sqrt{6} Cos\beta} \quad (10)$$

I_{DC} and V_{SY} are inserted in equation 3. We get:

$$E_{SY} = \sqrt{\frac{\pi^2 (V_D - I_{DC} r_d)^2}{(3\sqrt{6} Cos\ \beta)^2} - 6\left(\frac{I_{DC}}{\pi}\right)^2 (X_q Cos\ \gamma - R_{SY} Sin\ \gamma)^2} - \sqrt{6}\left(\frac{I_{DC}}{\pi}\right)(R_{SY} Cos\ \gamma - X_d Sin\ \gamma) \quad (11)$$

The inverter frequency (Equation 6) and the value of E_{SY} (Equation 9) varies with the load angle from 0 to 20 degrees. The results are presented in table-1.

Values of f & E_{SY} for different values of α

TABLE-1

Load Angle in Degrees (α)	Inverter Output Frequency(Hz) (f)	E_{SY} (Volts)
0	50	215.0195
1	49.75	208.53
2	49.5	202.22
3	49.25	196.10
4	49	190.16
5	48.75	184.40
6	48.5	178.82
7	48.25	173.42
8	48	168.1835
9	47.75	163.1218
10	47.5	158.2250
11	47.25	153.49
12	47	148.9090
13	46.75	144.4802
14	46.5	140.1971
15	46.25	136.06
16	46	132.0434
17	45.75	128.16
18	45.5	124.40
19	45.25	120.7395
20	45	117.18

The relationship between the frequency value (f) and the value of induced e.m.f. (E_{SY}), with the help of Table-1 is as follows:

(45,117.18), (50, 215.0195)

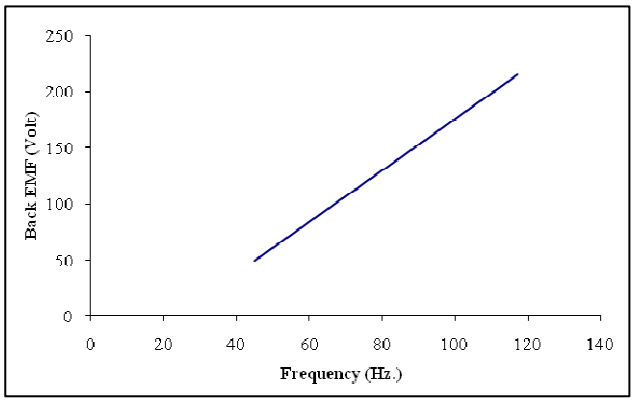

Fig.5: Relationship between f and E_{SY}

From Fig.5

$$f = 45 + \frac{5}{97.8395}(E_{SY} - 117.18)$$

We know that:
Motor speed, N = 120 f / P [where, no. of pole=4]

Motor speed, N = 120 f / P

$$N = 1350 + 1.53\left[\sqrt{\frac{\pi^2(V_D - I_{DC}r_d)^2}{(3\sqrt{6}Cos\beta)^2} - 6\left(\frac{I_{DC}}{\pi}\right)^2(X_q Cos\gamma - R_{SY}Sin\gamma)^2} - \sqrt{6}\left(\frac{I_{DC}}{\pi}\right)(R_{SY}Cos\gamma - X_d Sin\gamma) - 117\right] \quad (12)$$

Torque developed by the motor,

$$Tm = \frac{3E_{sy}I_{sy}Cos(\theta-\alpha)}{\omega}$$

$$Tm = \frac{3E_{sy}I_{sy}Cos(\theta-\alpha)}{2\pi N_{rps}} \qquad [\text{where } N_{rps} = \frac{N}{60}]$$

$$Tm = \frac{3x60xE_{sy}\sqrt{6}I_{DC}Cos(\theta-\alpha)}{2\pi N\ \pi}$$

$$Tm = \frac{22.34E_{sy}(1.40+0.6242\alpha)Cos(\theta-\alpha)}{N}$$

[If, K=22.34]

$$Tm = \frac{KE_{sy}(1.40+0.6242\alpha)Cos(\theta-\alpha)}{N} \quad (13)$$

Equation 12 provides the steady state general equation of commutatorless DC shunt motor. The load angle leads the parameter of X_q (Eq.7), X_d (Eq. 8) and I_{DC} (Eq. 9). Here, the speed of commutatorless DC shunt motor is dependent on the value of the load angle, D.C link voltage and firing angle of the inverter. The machine torque depends on load angle (α).

Part−2 (Transient Analysis)

Here we derive the transient analysis as performance equations from steady state equation, where the transient time is one second [13]. The total transient consists of two parts: sub-transient (20% of total transient time) and transient (80% of total transient time).

Sub-transient time (time duration 0.20 Sec.) [13]:

$\alpha_{ST} = [\alpha + 0.1875\ \alpha\ Sin(\omega t)e^{-1.63t}]$ (14)
When the load is applied on the motor
Where, α_{ST} = Sub transient load angle in electrical degree.
$\alpha_{ST} = [\{(\alpha - \alpha_r) - (0.1875\ \alpha_r)\}\ Sin(\omega t)e^{-1.63t}]$ (15)
When the load is removed from the motor
Where, α_r = removed load angle
$I_{DC} = 1.40 + 0.6242\ \alpha_{ST}$ (16)
$f = 50 - 0.25\ \alpha_{ST}$ (17)

Transient time (time duration 0.8 Sec.) [13]:
$\alpha_{ST} = [\alpha + 0.125\ \alpha\ Sin(\omega t)e^{-2.14t}]$ (18)
When the load is applied on the motor

Where, α_T = Transient load angle in electrical degree.

$$\alpha_{ST} = [\{(\alpha - \alpha_r) - (0.125\ \alpha_r)\}\mathrm{Sin}(\omega t)e^{-2.14\,t}] \quad (19)$$

When the load is removed from the motor

Where, α_r = removed load angle

$$I_{DC} = 1.40 + 0.6242\ \alpha_{ST} \quad (20)$$

$$f = 50 - 0.25\ \alpha_{ST} \quad (21)$$

If I_{DC} of sub-transient and transient are applied in the general equation (12) & (13) of the steady state, the transient equations during load applied or load removed moment are derived.

4 Results and Discussion

The following transient characteristics of the drive are derived from the computed results during load applied or load removed moments. Firstly, the analytical transient characteristics of the commutatorless DC motor are shown in Fig.6 to 8 for an applied load.

i) Speed Vs time.
ii) DC Current Vs time.
iii) Torque Vs time.

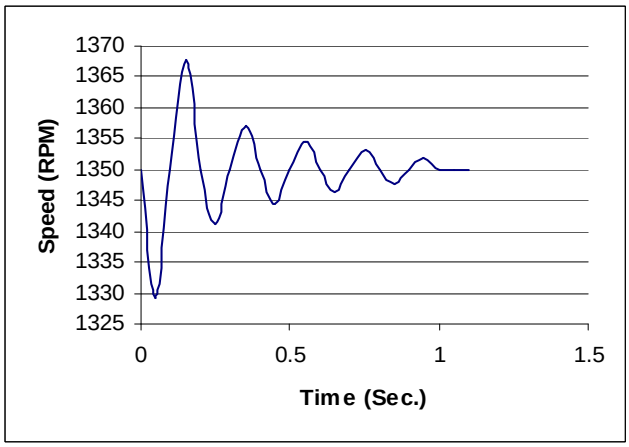

Figure 6: Speed Verses Time Characteristics

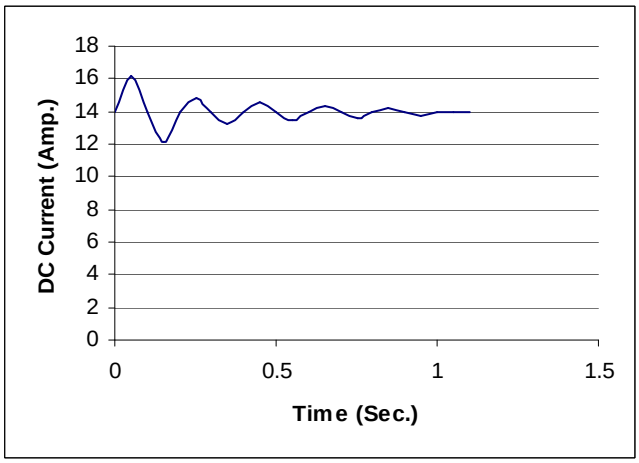

Figure 7: DC Current Verses Time Characteristics

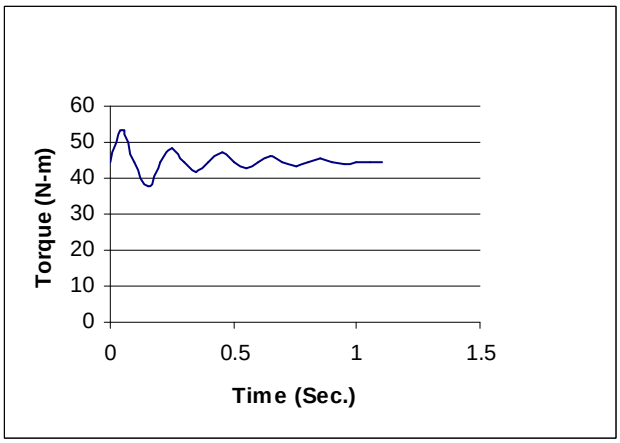

Figure 8: Torque Verses Time Characteristics

Secondly the analytical transient characteristics of the commutatorless DC motor are shown in Fig.9 to 11 for a removed load.

i) Speed Vs time.
ii) DC Current Vs time.
iii) Torque Vs time.

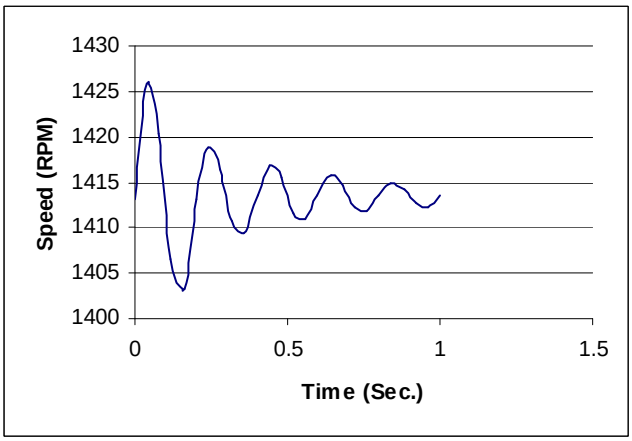

Figure 9: Speed Verses Time Characteristics

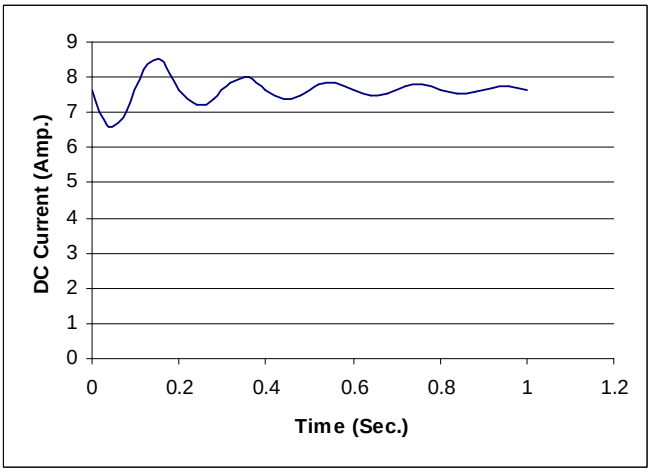

Figure 10: DC Current Verses Time Characteristics

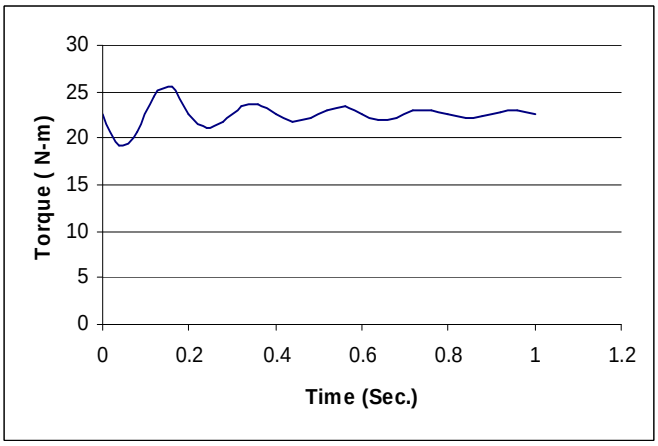

Figure 11: Torque Verses Time Characteristics

The salient feature regarding the performance of commutatorless DC shunt motor may be observed from the computed results during step changes or variation in load. The transient results are provided in Figs 6-11. Figs 6 and 9 represent the deviation (oscillation with time) of the speed of the commutatorless DC shunt motor. Figs 7 and 10 represent the deviation (oscillation with time) of the inverter input DC link current of the commutatorless DC shunt motor. Figs 8 and 11 represent the deviation (oscillation with time) of the torque of the commutatorless DC shunt motor.

5 Conclusions

The transient performance of the commutatorless DC shunt motor was computed using Fortran Power Station programming. The performance characteristic (its speed verses time, d.c. link inverter current verses time and torque verses time) of LCI fed synchronous motor in shunt mode is computed from the mathematical model and the transient characteristics of step changes load (either load applied or load removed). It is evident that transient performance of commutatorless D.C shunt motor is superior to the conventional D.C shunt motor.

References

[1] Muhammad Harunur Rashid, "Power Electronic," Prentice-Hall of India, 2003.

[2] PC Shen, "Power Electronics," Tata McGraw-Hill, 1987.

[3] A.F.Puuchstein, T.C.LIoyd, A.G.Conrad, "Alternating Current Machines," Third Edition, Charles E. TUTTLE Co, Tokyo, John Wiley & Sons, Inc, New York, 1954.

[4] Chrles S. Siskind, "Electrical Machines-Direct & Alternating current," Second edition, McGraw-Hill, 1966.

[5] A.E. Fitzgerald, Charlesn Kingsley. Jr. & Stephen D. Umans, "Electri Machinery", Second Edition, Tata McGraw-Hill, 2002.

[6] Kenji Watanabe, Katsuji Oyamori and Nriaki Sato, "Effect of magnetic saturation on the operation charteristics of series commutatorless motor," Electrical Engineering in JAPAN, vol.96, No.4 pp.349-355, July 1976.

[7] F.C. Brockhurt, "Performance Equation for D, C. commutatorless motor using Salient pole Synchronous Type Machine," *IEE Trans. On Industry Application*, Vol IA-16, No.3, pp.362-371, May/June 1980.

[8] Hoanglethy, Alain jakuboweiz and Robert perret, "A self controlied synchronous motor drive using terminal voltage system," *IEEE Trans. Industry applications*, Vol. Ia-18, no. 1, pp. 64-53, January/ February, 1982.

[9] Takeda, S, Morimoto and T, Hirasa, "Generalized Analysis for steady state characteristics of D.C. Commutatorless Motor," *IEE proceedings*, Vol 130, pt, B, No.6, pp. 373-380, November 1983.

[10] Chanrasekhar Namuduri and Paresh C.Sen, "Digital Simulation of an Inverter Fed self – controlled synchronous motor", *IEEE Trans. On Industrial Electronics*, Vol.-IF-34, No. 2pp.205-204, May, 1987.

[11] Ajay Kumar, R. Abarasu and B.P. Singh, "Steady State Performance of Series Commutatorless D.C. Motor, "*JIE (INDIA)*, Vol. 65, No. 6, pp.185, June 1985.

[12] F. Hareshima and T. Haneyoshi, "An Analysis of Commutatorless Motor with Salient Pole and D.C. Reactor of Finite Size", Electrical Engineering in Japan, Vol. 97, No. 6, pp. 36-44, November-December 1977.

[13] Gorislav Erceg, Ph.D Tomislav Idzotic, PhD, "Synchronous Generator Load Angle Measurement and Estimation," Faculty of Electrical Engineering and Computing Department of electrical machines, drives and automation Zagreb, Croatia

[14] D. Sumina, A. Sala, R. Malaric, "Determination of Load Angle for Salient-Pole Synchronous Machine." Faculty of Electrical Engineering and Computing, University of Zagreb, Unska 3, 10000 Zagreb, Croatia.

[15] John Rosa, "Utilization and Rating of machine commutated inverter synchronous motor drive," *IEEE Trans an Industry Application*, Vol 14-15, No.2, pp.155-164, March-April 1979.

Engr.Mohammad Abdul Mannan received B.Sc. Engg. (EE) from Ctg.Engg. College (Now CUET) in 1984 and M.Sc. Engg (CSE) from BUET in 1993. He is a Professor of EEE Dept, Dean of EEE faculty and Syndicate Member of DUET, Gazipur. He has published more than ten publications and five Professional System Design works. His reaserch interests include Renewable Energy Systems, High Tech Security Systems and Control and Automation Systems.

Md. Aminul Islam received B.Sc. Engg. (EEE) from BIT Dhaka (now DUET) in 1995 and M.Sc. Engg. (EEE) from DUET in 2005. He is presently undertaking a Ph.D in Electrical and Electronic Engineering, Dhaka University of Engineering & Technology (DUET). He is also the Deputy Chief Engineer (Electrical) in a private organization. His resarch interests include Energy Systems, Smart Grid and PLC Systems.

Performance Comparison of Different Software Fault Tolerance Methods

Md. Nasim Adnan, Mohammod Akbar Kabir, Lutful Karim, Nargis Khan

Abstract—A fault tolerance system is required for developing highly reliable computing systems that can function under adverse conditions, which is indispensable in safety critical applications. Fault tolerance is a major research issue in computing system designs because of the difficulty in producing error-free computing systems. This paper presents the recent development of software fault tolerance techniques and compares the performance of different software fault tolerant techniques and provides future research directions.

Keywords— Checkpoint, N version Programming, Recovery Blocks, Software Fault tolerance.

1 Introduction

FAULT tolerance is a major research area in computer system design because computers affect every aspect of modern life. Thus computing systems are required to operate without interruption for a long period of time. Fault tolerance makes systems capable of being operated in faulty conditions and protects against accidental or malicious destruction of information and generating erroneous output. It also ensures that confidential information cannot be divulged unintentionally. On the other hand, software is a key part of several critical applications, such as flight control systems and medical systems, as well as in real time systems. Therefore the researchers aim to develop fault tolerant software systems.

Despite the widespread use of software, it is extremely difficult to develop flawless software. In practice, at the end of the software testing phase, project managers assess software reliability (or quality) to fulfill a desired target. However, there is always the possibility that faults may be discovered later. This paper presents existing software techniques, identifies the limitations of these techniques and endeavours to provide solutions and further research directions in this area. Section 2 defines the important fault tolerant concept and terminology. In section 3, existing software fault tolerance techniques are presented. Section 4 discusses software fault detection techniques. In section 5 we identify certain limitations of existing fault detection and tolerance techniques, and present solutions and future research directions.

2 Terminology

Important terminology related to fault tolerance include [1]:

a) Fault

Fault is defined as an incorrect state of hardware or software resulting from physical defects, design flaws or operator error.

b) Fault Models

Depending on the system's behavior once a fault has occurred, the faults are characterized into different groups or classes.

c) Error

An error is part of a system state that may lead to a failure, or the manifestation of a fault.

d) Failure

When a system or a module is designed, its behavior is specified. When it is in service, we can observe its behavior. If the observed behavior differs from the specified behavior it is referred to as a failure. Failure is also the system level effects of an error.

e) Crash Failure

A process undergoes crash failure when it permanently ceases to execute its actions. This is an irreversible change, excluded from *napping* failures, where a process may play dead for a finite period of time before resuming operation. In *fail-stop* models, neighbors (processes) detect the faulty process, which crashes.

f) Omission Failure

Consider a transmitter process sending a sequence of messages to a receiver process. If the receiver does not receive some of the messages sent by the transmitter, an omission failure occurs.

g) Transient Failure

The agent inducing this failure may be temporarily active, but it can make a lasting effect on the global state. The failure can affect the global state in an arbi-

- *Assistant Professor, Department of Computer Science & Engineering, University of Liberal Arts, E-mail:nasim_1547@yahoo.co.uk.*
- *Assistant Professor, Department of Economics, University of Dhaka, E-mail: akbar_kabir03@yahoo.com.*
- *Research assistant to complete PhD from a University in Canada. E-mail: sumon_lk@yahoo.com.*
- *Lecturer, Department of Computer Science, Daffodil International University, Dhaka, Bangladesh, Email: nargis_ju@yahoo.com.*

Manuscript received on 30 July 2011 and accepted for publication on 27 October 2011.

© 2011 ULAB JSE

trary manner.

h) Byzantine Failure

A process behaves arbitrarily when a Byzantine failure occurs. It represents the weakest of all failure models as it allows every conceivable form of erroneous behavior.

i) Software Failure

In some cases, the execution of a program suffers from the degeneration of the run-time system due to 'memory leaks', leading to a system crash. There may be problems with the adequacy of specifications, as occurred during the 'Y2K' problem. Many of the failures, such as crash, omission, transient, or Byzantine can be caused by software bugs.

j) Temporal Failure

Real time systems require actions to be completed within a specific time period. When this timestamp is not met, a temporal failure occurs.

k) Software Reliability

According to ANSI's definition, software reliability is defined as the probability of failure-free software operation for a specified period of time, in a specified environment.

3 Software Fault Tolerance Techniques

In this section we present a number of software fault tolerance techniques [1], [2]. Software fault tolerance is basically divided into two groups: single version and multi-version software techniques. Single version techniques are concerned with single software by adding several types of mechanisms during the design phase, with a goal to detect, contain, and handle errors. Multi-version fault tolerance techniques use multiple versions of the same software in a structured way to ensure that design faults in one version do not cause system failure. Different software fault tolerance techniques are discussed below.

3.1 Single Version Software Fault Tolerance Techniques

Single-version fault tolerance is based on the use of redundancy applied to a single version of a piece of software to detect and recover from faults. Among others, single-version software fault tolerance techniques include considerations of program structure and actions, error detection, exception handling, checkpoint and restart, process pairs, and data diversity.

3.1.1 Software Structure and Actions

The software architecture provides the basis for the implementation of fault tolerance. Various types of software structure and actions are available. Among them, the most popular techniques include: Modularizing, Partitioning, System Closure, and Temporal Structuring. The use of modularizing techniques to decompose a problem into manageable components is as important to the efficient application of fault tolerance as it is to system design. Partitioning is a technique for providing isolation between functionally independent modules. System closure is a fault tolerance principle stating that no action is permissible unless explicitly authorized. Temporal structuring of the activity between interactive structural modules is also important for fault tolerance.

3.3.2 Checkpoint and Restart

For single-version software, there are few recovery mechanisms. The most useful mechanism is the checkpoint and restart mechanism. A restart or backward error recovery (Figure 1) has the advantage of being independent of the damage caused by a fault, applicable to unanticipated faults, general enough to be used at multiple levels in a system, and conceptually simple. There are two types of restart recovery: static and dynamic. A static restart recovery is based on returning the module of software to a predetermined state. This can be a direct return to the initial reset state, or to one of a set of possible states. The selection is based on the operational situation at the moment the error detection occurred. Dynamic restart uses dynamically created checkpoints that are snapshots of the state at various points during the execution. Checkpoints can be created at fixed intervals or at particular points during the computation, determined by an optimization rule.

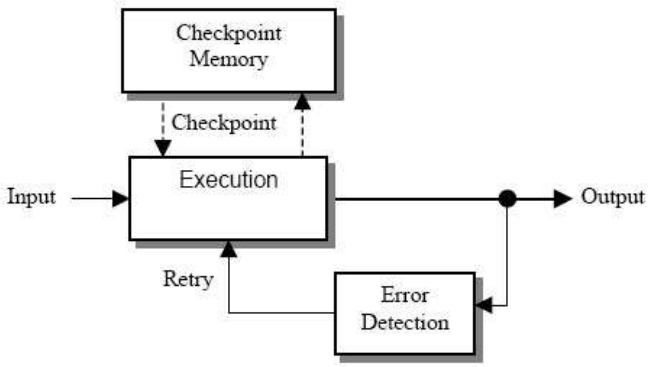

Figure 1: Logical Representation of Checkpoints and Restart

3.3.3 Process Pairs

A process pair uses two identical versions of software that run on separate processors (Figure 2). The recovery mechanism is checkpoint and restart. Two types of processors, namely primary and secondary processors, are used in this technique. Primary processors actively process the input and create output, as well as generating checkpoint information sent to the backup or secondary processors.

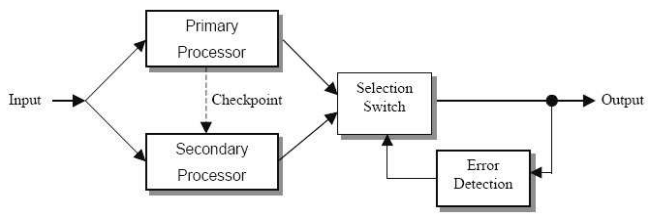

Figure 2: Logical Representation of Process Pairs

3.2 Multi-Version Software Fault Tolerance Techniques

Multi-version fault tolerance is based on two or more versions (or "variants") of a piece of software, executed either in serial or in parallel. The versions are used as alternatives (with a separate means of error detection) in pairs (to implement detection by replication checks) or in larger groups (to enable masking through voting).

3.2.1 Recovery Blocks

Fault tolerance techniques are alternate versions of a primary version of software used and the correct output (i.e. from all outputs of a primary version and alternative versions) is generated by a selection switch and an application dependent acceptance test. The recovery block technique increases the pressure on the specification to be specific enough to create multiple functional alternatives that are functionally the same.

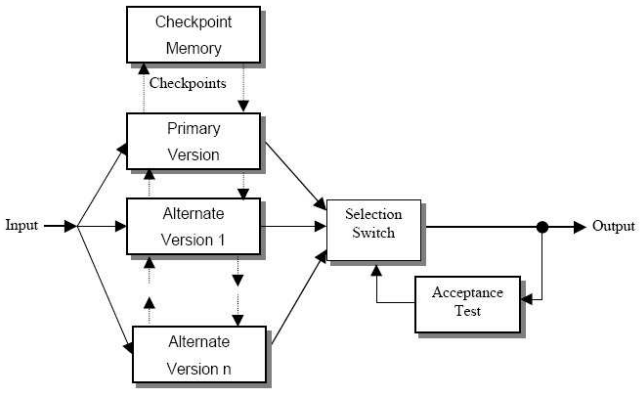

Figure 3: Recovery Block Model

3.2.2 N-Version Programming

N-Version programming [3] is a multi-version technique in which all versions are designed to satisfy the same basic requirements. The correctness of output is determined by comparing all outputs (Figure 4). The use of a generic decision algorithm (usually a voter) to select the correct output is a fundamental difference from the Recovery Blocks approach, which requires an application dependent acceptance test. This system can potentially overcome the design faults present in most software by relying on the design diversity concept.

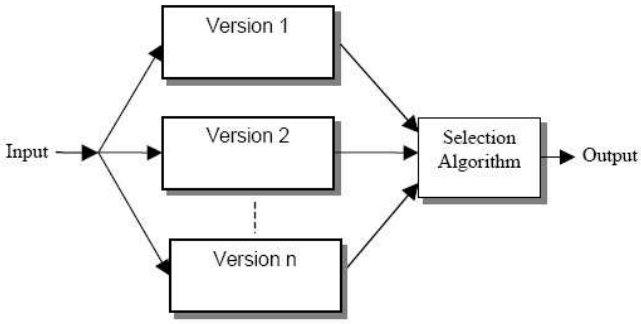

Figure 4: N Version Programming Model

3.2.3 N Self-Checking Programming

N Self-Checking programming uses multiple versions of software, combined with the structural variations of the Recovery Blocks and N-Version Programming. N Self-Checking programming using acceptance tests is shown in figure 5. Here, the versions and acceptance tests are developed independently from common requirements. The use of separate acceptance tests for each version is the main difference between the N Self-Checking model and the Recovery Blocks approach.

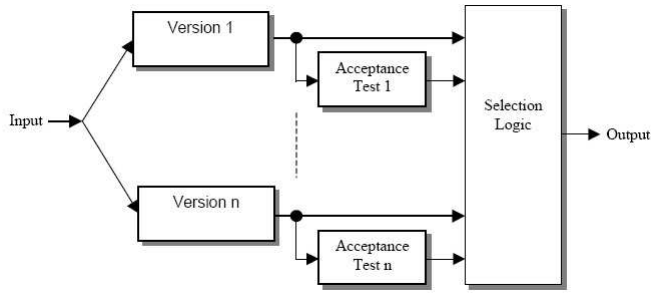

Figure 5: N Self-Checking Programming using Acceptance Tests

N self-checking programming using n-acceptance tests to compare the output for error detection is shown in figure 6. Like N-Version Programming, this model has the advantage of using an application independent decision algorithm to select a correct output. This variation of self-checking programming has a theoretical vulnerability of encountering situations where multiple pairs pass their comparisons, but with different outputs.

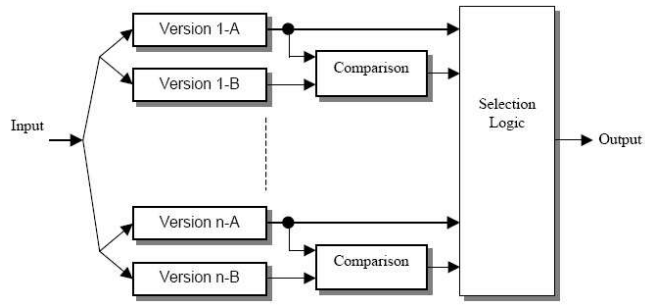

Figure 6: N Self Checking Programming using Comparison

3.2.4 Consensus Recovery Blocks

The Consensus Recovery Blocks (Figure 7) approach combines N-Version Programming and Recovery Blocks to improve the reliability achieved by using just one approach. The acceptance tests in the Recovery Blocks suffer from a lack of guidelines for development and a general tendency to design faults that are due to the inherent difficulty in creating effective tests. The use of voters, like in N-Version Programming, may not be appropriate in all situations, especially when multiple correct outputs are possible. In that case, a voter, for example, may result in failure when selecting an appropriate output. Consensus Recovery Blocks use a decision algorithm similar to N-Version Programming as a first layer of decision making. If this first layer finds a failure, a second layer using ac-

ceptance tests similar to those in the Recovery Blocks approach is invoked.

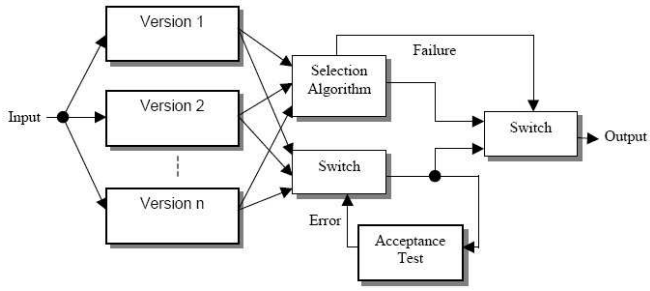

Figure 7: Consensus Recovery Blocks

4 SOFTWARE FAULTS DETECTION

In this paper [2], a number of techniques are proposed to detect and recover from transient faults. Transient faults (also known as soft errors), unlike manufacturing or design faults, do not occur consistently. To counter these faults, designers typically introduce redundant hardware such as RAID architecture, N-modular system, and error correcting code (ECC) to detect and recover from faults. However the hardware fault tolerant mechanisms are too expensive for many markets. On the other hand, software approaches to redundancy are attractive because they are essentially free of cost.

4.1 Error Detection by Duplication Instruction (EDDI)

EDDI [4] is a software-only fault detection system that operates by duplicating program instructions and using the redundant execution of programs to achieve fault tolerance. Program instructions are duplicated by the complier and are intertwined with the original program instructions. Each copy of the program, however, uses different registers and different memory locations so as to not interfere with one another. At certain synchronization points in the combined program code, the compiler makes sure that the original instructions inserts check instructions and their redundant copies agree on computed values. Since program correctness is defined by the output of a program, and if we assume memory-mapped I/O, then a program is executed correctly. Consequently, it is natural to use stored instructions as synchronization points for comparison. Unfortunately, it is insufficient to use the stored instructions as the only synchronization points, since misdirected branches may cause stored instructions to be skipped, incorrect stores to be executed, or incorrect values to feed a store. Therefore, branch instructions must also be synchronization points at which redundant values are compared.

4.2 Software Implemented Fault Tolerance (SWIFT)

SWIFT [4] is an efficient software-only, transient-fault detection technique. SWIFT efficiently manages redundancy by reclaiming unused instruction-level resources that are present during the execution of most programs. SWIFT makes several key refinements to EDDI and incorporates software only signature based control flow-checking scheme to achieve exceptional fault coverage. The major difference between EDDI and SWIFT is that while EDDI's SOR includes memory subsystems, SWIFT moves memory out of the SOR, as memory structures are already well-protected by hardware schemes such as parity and ECC, with or without scrubbing. SWIFT's performance greatly benefits from having only half of the memory subsystems.

5 ANALYSIS AND DRAWBACKS OF EXISTING SOFTWARE FAULT TOLERANCE TECHNIQUES

The methods discussed in the preceding sections are mostly used in critical and highly available systems. Fault tolerant techniques are highly reliable and available. However we found limitations in some software fault tolerance techniques. In the single version fault tolerant technique, reliability is achieved by sacrificing processing time [5]. On the other hand, in multi-version fault tolerance technique, the availability and reliability is achieved by using redundant components, which results in extra costs. Moreover, developing the multi-version software is more complex than for normal software [6],[7].

We note that software faults tend to be stated dependent and activated by particular input sequences. Although a component's reliability is an important quality measure for system level analysis, software reliability is hard to estimate and post-verification reliability estimation remains controversial. For some applications, software safety is more important than reliability and fault tolerance techniques used in those applications are aimed at preventing catastrophes. Single version software fault tolerance techniques include system structuring and closure, atomic actions, inline fault detection, exception handling, and checkpoint and restart. Process pairs exploit the state dependence characteristic of most software faults to allow uninterrupted delivery of services, despite the activation of faults. Similarly, data diversity aims to prevent the activation of design faults by multiple alternate input sequences. Multi-version techniques are based on the assumption that software built differently should fail differently, and thus, if one of the redundant versions fails, at least one of the others should provide an acceptable output. Recovery blocks, N-version programming [8], [9], N self-checking programming, consensus recovery blocks, and n / (n-1)-variant techniques were presented. However special consideration was given to multi-version software fault tolerance and output selection algorithms. Operating systems must be given special treatment when designing a fault tolerant software system because of the cost and complexity associated with their development, as well as their complexity for correct system functionality.

6 FUTURE WORK

Many techniques have been developed to achieve fault tolerance in software. Each technique must be tailored to the particular application. In this paper, some im-

portant fault tolerance techniques were reviewed and their characteristics identified. Future work may involve using this information to develop new and improved techniques. Attention ought to be paid to data diversity rather than design diversity.

7 Conclusion

This paper reviews existing software fault tolerance techniques and investigates the performance metrics of these techniques. We identified the characteristics of several software fault tolerance techniques. Finally, we analyzed the limitations of these techniques. The application of these techniques is relatively new to the area of fault tolerance. The differences between each technique provide some flexibility of application.

References

[1] W. Torres-Pomales, "Software Fault Tolerance: A Tutorial," *Langley Research Center, Hampton, Virginia,* October 2000.

[2] G. A. Reis, J. Chang, N. Vachharajani, R. Rangan and David I., *Proceedings of the International Symposium on Code Generation and Optimization (CGO'05), IEEE,* August 2005.

[3] A. S. Vilkomir, L. David Parnas, B. V. Mendiratta,and E. Murphy, "Availability evaluation of hardware/software systems with several recovery procedures," *Proc. 29th Ann. International Computer Software and Applications Conference, IEEE*, 2005

[4] N. Oh. P.P. Shirvani, and E.J. McCluskey, "Error detection by duplicated instructions in super-scalar processors," *IEEE Transactions on Reliability*, vol. 51, no. 1, pp.63-75, March 2002.

[5] C.Y Huang, C.T Lin, and C.C Sue, *Software Reliability Prediction and Analysis durng Operationa use*, 0-7803-8932, IEEE, 2005

[6] M. Reformat, E. Igbide, *Isolation of Software Defects: Extracting Knowledge with Confidence*, 0-7803-9093, IEEE, 2005

[7] X. Cai, M. R. Lyu, and M. A. Vouk, "An Experimental Evaluation on Reliability Features of N-Version Programming," *Proc. 16th IEEE International Symp. Software Reliability Engineering,* 2005.

[8] P. J. DENNING, "Fault Tolerant Operating Systems," *Computing Surveys*, vol. 8, no. 4, December 1976.

[9] A. Avizienis, *Toward Systematic Design of Fault- Tolerant Systems*, 0018-9162, IEEE, 1997.

Md. Nasim Adnan received M.Sc. in CSE from Bangladesh University of Engineering and Technology (BUET) and B.Sc. in CSE from Khulna University. He is currently working as an Assistant Professor in the department of Computer Science and Engineering, University of Liberal Arts Bangladesh (ULAB). He also served as a Deputy Director in ITOCD, Bangladesh Bank. His research interests include Software Engineering, Database Systems and E-commerce.

Mohammod Akbar Kabir received his M.Sc. and B.Sc. (Hons) in Computer Science from Dhaka University in 2000 and 1998 Repectively. Currently, he is working as an Assistant Professor in the dept. of Economics, University of Dhaka. He also served as an Assistant Director in ITOCD, Bangladesh Bank and as a Lecturer, Dept. of Computer Science, Dhaka City College, Dhaka. His research interests include VLSI design and E-commerce.

Lutful Karim has been a faculty member of Computer Science in several Internationally reputed universities in Bangladesh and abroad since 2000. He is currently working as a Research Assistant to complete PhD from a reputed university in Canada. He has authored several refereed conference publications and journals, and is a member of an organization committee and technical program committee in several international conferences. His research interests include Wireless Communications, Wireless Sensor Network, Fault Tolerance Computing Systems and E-commerce.

Nargis Khan worked as a faculty member in Daffodil International University (DIU) and University of Development Alternatives (UODA) in Bangladesh for about 4 years after completing a Bachelors degree in Computer Science and Engineering from Jahangirnagar University, Bangladesh in 2004. She has published several refereed conference and journal papers. Her research interests include Wireless Communications and Networks, Mobile Computing, Computer Networks and Security.

A Modified and Cost Effective Approach to Extractions of Intersections from High Resolution Satellite Imagery in Different Road Areas

Boshir Ahmed and Md. Fayzur Rahman

Abstract—Satellite images are rich in information, yet complex to analyze. For Geographic Information System (GIS), many features require fast and reliable extraction of roads and intersections. Satellite images provide useful data that is extracted from images of urban areas. Automatic extraction of road intersections in urban areas remains a challenging task. This is due to the fact that high resolution satellite images contain multiple layers representing roads, buildings and other high density objects. Our goal is to automatically separate the road layer from other layers and then to extract the road intersections. Traditional image processing methods fail to achieve satisfactory performance in cases of high resolution satellite images. This paper proposes a modified and cost effective method for road extraction from high resolution satellites images. In order to find the precise road intersection of urban areas, we divided the whole process into two sequential modules. Firstly, the extraction of road lines using different morphological direction filtering automatically eliminates the other layers. Secondly, the extraction of road intersections determines road orientation and interconnectivity. The accuracy of road network extraction reaches 96.12%, which is significantly higher than existing road extraction methods.

Keywords—Automatic road extraction, High resolution satellite image, Intersection detection, Remote sensing, Geographic Information System (GIS), Urban area, Semi urban area, Morphology

1 Introduction

GEOGRAPHIC Information System (GIS) is becoming increasingly popular, thanks to the attractiveness of the internet and satellite images. Google, Yahoo and Virtual Earth are examples of exhibiting high resolution satellite images [9]. For Geographic Information System (GIS), many features require fast and reliable extraction of roads and intersections. Information about urban and rural road areas is useful for resource management, security monitoring, urban development. With the availability of high resolution satellite data and processing technologies, the integration of digital image analyzing systems with advanced GIS systems permit compositing data sources and foster a partnership between human and machine[7]. Satellite images offer opportunities in many areas, such as security monitoring, communication industry, rural microclimate and transportation navigation, landscape planning and visualization. Road extraction from remotely sensed images remains a challenging issue for image processing [2].

An early road extraction approach focuses on low-resolution aerial images. A road detector considering local and global criteria has been proposed (Fischler et al 1980). Road tracing step exploits local criteria calculated by low level processing. The method of line extraction is based on differential geometry is presented (Steger 1996). For each pixel in the image convoluted with the Gaussian kernel, the image profile along the principal direction is examined. Line points that are the first and second derivations of the profile have a vanishing and minimum respectively, and are detected and connected [4].

Automation is considered the most effective means of removing obstacles to labour intensive manual processes and reducing the cost and turnaround of spatial database updates [5]. Road layers are usually presented in single or double line format, depending on the image sources [1]. Our scheme considers a road as a group of "similar" pixels [6]. Traditional road extraction methods have certain disadvantages, such as long computational times, the existence of residual objects in the image that are not classified as roads and an inability to detect roads in every directions [3]. Most existing extraction methods for high resolution images rely on road boundaries as key hints for road extraction [6]. Our proposed methods avoid such disadvantages by performing automatic segmentation and various morphological operations in first steps. Various intersections aligned with non regular intervals in second steps are detected in the road's intersection points.

- *F.A. Author, Department of Computer Science & Engineering, Rajshahi University of Engineering & Technology (RUET), Bangladesh. E-mail:boshir_bd@yahoo.com.*
- *S.B. Author, Department of Electrical & Electronic Engineering, Rajshahi University of Engineering & Technology (RUET), Bangladesh. E-mail:mfrahman3@yahoo.com*

Manuscript received on 21 August 2011 and accepted for publication on 31 October 2011.

© 2011 ULAB JSE

2 Related works

Existing approaches to road extraction cover a wide variety of strategies, using different resolution aerial or satellite images. An extensive overview of the approaches is provided [11, 12]. Overall, schemes are divided into two groups: semi-automatic and automatic. Semi-automatic schemes require human interaction to utilise prior knowledge during the process of extraction, such as identifying road areas. Based on information provided by users, roads are extracted using methods such as profile matching [13], cooperative algorithms [14], and dynamic programming [15]. For automatic methods, we frequently extract hypotheses for road segments through edge and line detection, before establishing connections between road segments to form road networks. When data from multiple sources is combined [16] reliability improves. Depending on the type of image, some schemes deploy contextual information to guide the extraction of roads [17]. For uncluttered images, reducing the resolution helps to identify roads as lines [18]. However many proposed methods share the common assumption of relatively simplistic road models. The methods also require roads that are easily identifiable in images, such as constant intensity or straight and smooth road edges. As a result, sensitivity to interferences such as cars, shadows or occlusions is high and therefore consistent and reliable results often cannot be provided [10].

3 Proposed Approach

To determine the precise road intersection in urban areas, the entire process was divided into two sequential modules. The first is the extraction of road lines using different Morphological direction filtering, which automatically eliminates non-road layers. The second involves the extraction of road intersections to determine road orientation and interconnectivity.

The inputs of the method are high resolution satellite images. The proposed method is based on two steps. The first is to utilize an automatic segmentation algorithm to remove background pixels based on the difference in the luminosity level. We then obtain foreground pixels, which contain the entire information layer of the satellite image. The smoothing filter (median filter) is then used to remove salt and pepper noise, such as small objects that remain in the automatic segmentation step. Next, different morphological operation, dilation and boundary extraction are performed on existing objects to eliminate excess parts of image objects [9]. In the second part, various intersections are detected in the models, which are classified as three types of cross-roads; T-junctions and Y-junctions [4]. Finally, roads are extracted by connecting road intersections using the road tracking method.

Figure 1 illustrates the general process of extracting the road intersection from satellite images in rural areas.

3.1 Automatic Road Extraction

Applying the automatic road extraction algorithm to disconnected road segments is difficult, due to the poor visibility of roads in the original image. Roads are often divided into several short segments, or are completely missing from the image. To overcome this problem, we fit Gaussian models to image points, which represent the likelihood of being road points. These models are evaluated recursively to determine the correlation between neighboring points. The iterative process consists of finding the connected road points, fusing them with the previous image, passing them through the directional line filter set and computing new magnitudes and orientations. The road segments are updated, and the process continues until there are no further changes to the roads extracted. We combine the following steps for automatic road extraction processes.

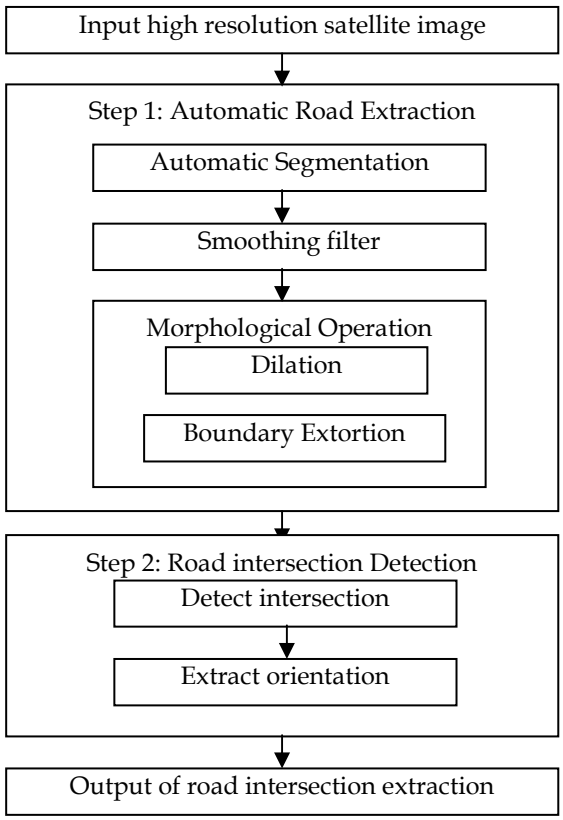

Figure 1: Overall approach to extract road intersections

3.1.1 Automatic segmentation

Segmentation is the process of grouping an image into units that are homogeneous in terms of one or more characteristics [20]. The common technique, segmentation, is used to automatically separate the foreground from background pixels. The color information from RGB values is first discarded by converting the original input image to an 8 bit grayscale with 256 color levels. We then use a threshold value to convert the grayscale image into a binary image. Segmentation uses the threshold to segment the foreground pixels from background pixels. Threshold assumes that images are composed of regions with different gray level ranges; the histogram of an image can be separated by a certain number of peaks, where each corresponds to one region with a seed value that

separates two adjacent peaks [21]. The gray scale and binary images are shown in Figure 3 and 4.

Figure 2: Input high resolution satellite image [8]

Figure 3: Gray scale image

Figure 4: Binary image

3.1.2 Smoothing filter

Median filters are particularly effective in the presence of both bipolar and unipolar impulse noise. A median filter is a nonlinear digital filtering technique, which is often used to remove random and salt-and-paper noise. Noise reduction is a common preprocessing step that improves subsequent processing results [9]. The replacement of a pixel by the median filter of the gray level in the neighborhood of that pixel is given by:

$$\hat{f}(x,y) = \underset{(s,t)\in S_{xy}}{median}\{g(s,t)\}$$

The original value of the pixel is included in the computation of the median filter.

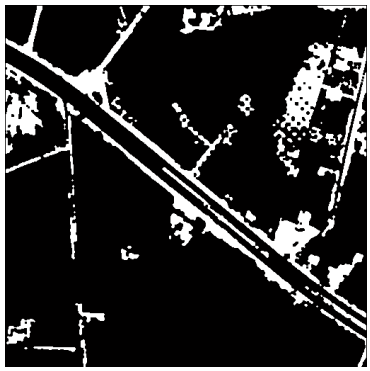

Figure 5: Median filtered image

3.1.3 Morphological operation

There are two Morphological operations: Dilation and Boundary extortion. Dilation operations are used for filling small holes and connecting disjoint object. The dilation processes are performed by laying the structuring element B on the image A. The structuring element can be square, rectangular, a circular disc, or any other shape [3].

Dilation:

$$A \oplus B = \left\{z \mid \left[\left(\hat{B}\right)_z \cap A\right] \subseteq A\right\}$$

Erosion:

$$A \Theta B = \left\{z \mid (B)_z \subseteq A\right\}$$

Where z is a displacement of the structuring element.

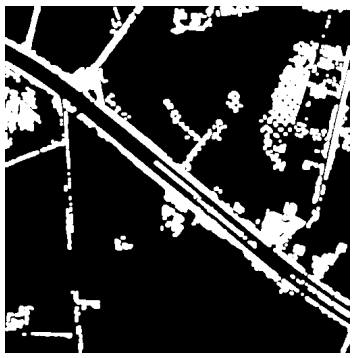

Figure 6: Image after dilation

The dilation operation is followed by the Morphological thinning operation. The binary thinning operation automatically extracts road intersections. Thinning operations are performed using hit-and-miss transform. The thinning of set A by structuring element B is denoted by $A \otimes B$ and can be defined by the terms of hit-and-miss transform [9].

$$\begin{aligned} A \otimes B &= A - (A \circledast B) \\ &= A \cap (A \circledast B)^c. \end{aligned}$$

The hit-and-miss transform is a general binary morphological operation used to identify particular patterns

of foreground and background pixels within an image. Binary masks are used to scan over the input binary images. If the masks match with the pixels, it is a "hit"[9]. If the mask does not match, it is a "miss."

Figure 7: Image after boundary extraction

3.2 Road intersection Detection

To discover a road intersection, we first detect the intersection candidate before extracting road orientation. The road seed is a high density pixel denoting the road object. We now consider the steps described below.

3.2.1 Detecting intersection

A road seed is a binary image, with a white pixel denoting a high probability of a road-like object. As extraction errors arising from certain pixels on roof buildings or soil have a similar spectral response to roads and general morphological operator, the combination with closing, thinning and 8-neighbour pattern matching does not work particularly well. This is due to the high sensitivity to noise. Therefore, stronger constraints and further knowledge about intersections are required. We consider three types of intersections. The Crossroads represents the intersection of two road portions, while the Three-forked road has three road segments. Each branch has a different direction. The third is the T-Intersection, consisting of one straight road and a connected branch [4].

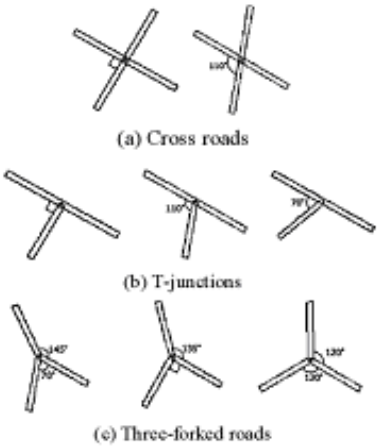

Figure 8: Types of road intersections [4].

Consider matching the above models to road seed and calculating matching value between the models and road seed. The model is rotated and positioned over the binary image. The matching measure is defined as follows,

$$M\theta_{(x,y)} \equiv \begin{cases} \mu(s)-\mu(B), if & \min\limits_{n=1,2,.....N} \mu(S_n) > k_1 \\ 0 \quad , & otherwise \end{cases}$$

3.2.2 Extracting Road orientation

Road layers are connected by constricting branches of each intersection. Road tracking methods are available for the hypothesis. A structure of road curve-linear is modeled as ternary tree [4]. The directions of the tracking are given by center point and the direction at each branch of the intersection. The road orientation is extracted in the following equation,

$$E(a) = \mu(A_{in}) - \mu(A_{out}), \qquad a \in A$$

Where A is the set of edge of the road tree. A_{in} and A_{out} are respectively inside and outside regions around road edges.

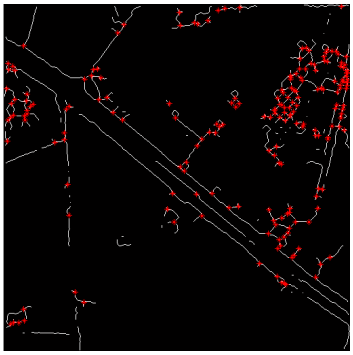

Figure 9: Cross points denote road intersections

4 Experimental Result and Performance Analysis

Our proposed method was tested on three sources of high resolution satellite images in urban, semi urban and rural areas. The road layers are a mixture of different small roads, buildings, grounds, and trees with many driveways connected to the road network. The distribution of buildings ranges from sparse to very close. The area contains many trees, with a number of large trees that are close to roads. The other layers, excluding the road layer, are difficult to remove using existing techniques. However the proposed approach demonstrates an ability to overcome these problems. Almost all roads in the network were successfully extracted and intersection points detected. The resulting images from our experiment are shown in Figure 9. In the figure, the red cross (X) represents the road intersection point extracted by the proposed method. On the other hand, our approach can extract intersections accurately and does not extract buildings as roads, even in suburban areas. The results indicate that we can construct road networks with a high degree of accuracy. The experimental achieved precisions with elapsed time comparisons are shown in Table 1. The

accuracy of our proposed method is fairly similar to the existing road intersection model, but our elapsed time is much shorter than every other method.

TABLE 1: ACCURACY OF DIFFERENT ROAD AREA FOR PROPOSED METHOD

Source information	MS (Multi Scale Snake) Method	Existing Road Intersection Model	Proposed Road Intersection Model
Accuracy Developed Suburban Area	57.9%	95.5%	96.12%
Accuracy Developed Urban Area	69.7%	95.7%	95.5%
Accuracy Developed Rural Area	98.4%	90.9%	92.82%
Elapsed Time Developed Suburban Area	40.5	15.2	1.0624 sec
Elapsed Time Developed Urban Area	46.6	16.5	1.2256 sec
Elapsed Time Developed Rural Area	20.2	14.4	4.1114 sec

Extracting the road intersections from various high resolution satellite images on an Intel Core2Duo 1.83 GHZ Dual Processors with 2 GB memory took less than one minute.

5 CONCLUSION AND OBSERVATIONS

The above results show that mathematical morphology is of significant interest to Very High Resolution Spatial image interpretation. The neighborhood relations are a significant advantage. The experiments indicate that the proposed methodology is particularly worthwhile. Thus a modified and cost effective method for road intersection from high resolution satellite images is presented in this paper. This modified method is performed in two steps; firstly, global segmentation and morphological direction filtering using a structuring element [3]. The second step detects various intersections aligned with non regular intervals, such as the cross-road, T-junction and Y-junction [4]. Our proposed method assumes that background pixels are separable, as the luminosity level of the background and foreground pixels vary. Foreground pixels contain larger values than background pixels [9]. The paper's main contribution to the field is a modified and cost effective method that automatically and efficiently extracts road intersections from high resolution satellite images. Our approach does not require former information of the input satellite image. We applied the proposed approach to three different satellite images: urban, semi-urban and rural. The images were obtained online from Google Map and we successfully extracted road intersection points to identify geographical information. The approach achieved maximum accuracy with a time lapse lower than other existing methods. The proposed method efficiently detected single, multiple, intersected and branched roads.

REFERENCES

[1] Yao-Yi Chiang, Craig A. Knoblock, and Ching-Chien Chen, "A tomatic Extraction of Road Intersections from Raster Maps", *Geoinformatica archive*, Volume 13 , pp. 121-157, June 2009, ISSN:1384-617

[2] Renaud P´eteri, Julien Celle and Thierry Ranchin "Detection And Extraction Of Road Networks From High Resolution Satellite Images" *Remote Sensing & Modeling Group,* Ecole des Mines de Paris B.P. 207-06904 Sophia Antipolis cedex, France.

[3] T. M. Talal1, M. I. Dessouky2, A. El-Sayed2 , M. Hebaishy1 and F. E. Abd El-Samie2 "Road Extraction from High Resolution Satellite Images by Morphological Direction Filtering and Length Filtering", *National Authority of Remote Sensing and Space Science*, Cairo (Egypt).2 Faculty of Electronic Engineering, Menoufia University, Menouf, Egypt.

[4] Go Koutakia, Keiichi Uchimuraa, Zhencheng Hub "Road Updating From High Resolution Aerial Imagery Using Road Intersection Model", Graduate School of Science and Technology, Faculty of Engineering, Kumamoto University, 2-39-1 Kurokami, Kumamoto, 860-8555 Japan.

[5] Xiangyun Hu C. Vincent Tao, "Automatic Extraction Of Main-Road Centerlines From High Resolution Satellite Imagery Based On Perceptual Grouping", *York University Annual Conference Proceedings*, May 2003 E Anchorage, Alaska.

[6] Yan Li and Ronald Briggs "Automatic Extraction of Roads from High Resolution Aerial and Satellite Images with Heavy Noise," *World Academy of Science, Engineering and Technology,* 54, pp. 416-422, 2009.

[7] Erick López-Ornelas "High Resolution Images: Segmenting, Extracting Information and GIS Integration", *World Academy of Science, Engineering and Technology*, 54, pp. 172-177, 2009.

[8] Yun Zhang and Ruisheng Wang "Multi-resolution and multi-spectral image fusion for urban object extraction", Department of Geodesy and Geomatics Engineering University of New Brunswick . XX ISPRS Congress.

[9] Boshir Ahmed, Md. Ali Hossain and Md. Ariful Islam "Automatic extractions of road intersections from satellite imagery in urban areas," *6th International Conference on Electrical and Computer Engineering (ICECE) 2010*, pp. 686-689, 18-20 December 2010.

[10] Yan Li and Ronald Briggs "Automatic Extraction of Roads from High Resolution Aerial and Satellite Images with Heavy Noise" *World Academy Science*, Engineering and Technology, 54, 2009.

[11] J.B. Mena," State of the Art on Automatic Road Extraction for GIS Update: a Novel Classification", *Pattern Recognition Letters*, 24(16):3037-3058, 2003.

[12] M.-F. Auclair-Fortier, D. Ziou, C. Armenakis, and S. Wang, "Survey of Work on Road Extraction in Aerial and Satellite Images", Technical Report 241, Département de mathématiques et d'informatique, Université de Sherbrooke, 1999.

[13] G. Vosselman, J.D. Knecht."Road Tracking by Profile Matching

and Kalman Filtering", *Workshop on Automatic Extraction of Man-Made Objects from Aerial and Space Images*, pp. 265-274, 1995.

[14] D.M. Mckeown, J.L. Denlinger, "Cooperative Methods for Road Tracking in Aerial Imagery", *Workshop Computer Vision Pattern Recognition*, pp. 662-672, 1988.

[15] A. Gruen, H. Li., "Semi-automatic Linear Feature Extraction by Dynamic Programming and LSB-Snakes", *Photogrammet Eng. Remote Sensing*, 63, pp. 985-995, 1997.

[16] S.B. Hinz, A. Ebner"Modeling Contextual Knowledge for Controlling Road Extraction in Urban Areas", *IEEE/ISPRS Joint Workshop Remote Sensing Data Fusion over Urban Areas*, 2001.

[17] T. Ohlhof, T. Emge, W. Reinhardt, K. Leukert, C. Heipke, K. Pakzad," Generation and Update of VMAP data using satellite and airbone imagery", *Remote Sensing*, vol. 33, pp. 763-768, 2000.

[18] A. Baumgartner, C.T. Steger, C. Wiedemann, H. Mayer, W. Eckstein, and H. Ebner, "Update of Roads in GIS from Aerial Imagery: Verification and Multi-Resolution Extraction", *Proceedings of International Archives of Photogrammetry and Remote Sensing*, XXXI B3/III:53–58, 1996.

[19] Erick López-Ornelas, 'High Resolution Images: Segmenting, Extracting Information and GIS Integration

[20] R. Gonzalez, and R. Woods, *Digital Image Processing*, Addison-Wesley, 1993.

[21] A. Marion, *Introduction aux techniques de traitement d'images*, Ed. Eyrolles, 1987.

Boshir Ahmed, Head, Department of Computer Science & Engineering, Rajshahi University of Engineering & Technology. Research interests include Digital Image Processing, Microprocessor based system design, Digital Logic Design, Digital Signal Processing, Computer Networking and Digital Communication. Total number of published publications: 26 in which the number of journals: 05, number of conference papers: 18, number of published books: 03.

Md. Fayzur Rahman received the B.Sc. Engineering degree in Electrical & Electronic Engineering from Rajshahi University of Engineering & Technology in 1984 and M. Tech. degree in Industrial Electronics from S. J. College of Engineering, Mysore, India in 1992. He received his Ph.D. in energy and environment electromagnetic field from Yeungnam Unversity, Taegu, South Korea, in 2000. He serves as a Professor in Electrical & Electronic Engineering. His research interests include high voltage discharge application covering the control of non termal plasma, Ozone generation system, Image processing, dc drive and machine control. He is a fellow of IEB, Bangladesh and member of Korean Institute of Illuminating and Electrical Installation (KIIEE) and Korean Institute of Electrical Engineers (KIEE), Korea.

Design and Development of Microcontroller Based Digital pH Meter

M. A. A. Mashud, M. A. Masud, Md. Serajul Islam

Abstract— A Microcontroller based digital pH meter was designed and developed to measure the value of pH (acidity or alkalinity) for any type of solution. Two op-amps of high input impedance and low output impedance were used to design the pH meter: one is used as a buffer and the other as a summing amplifier. The output of the summing amplifier is connected to the microcontroller as an input. The pH value of a solution microcontroller provides the output value. A microcontroller PIC12F675 was used to control the developed system's function. A C language program was developed to control the function of the microcontroller, using the PCWH Compiler. The output of the microcontroller is displayed as a pH value that ranges from 0.0 to 14.0 in the three seven segment display.

Keywords— microcontroller, PCWH, Ulcer, Gastric, pH probes, clinic, patients.

1 Introduction

A pH meter is an electronic instrument that measures a liquid's pH. A typical pH meter consists of a special measuring probe (a glass electrode) [1] which is connected to an electronic meter that measures and displays the pH reading. Typical applications include ulcer and gastric tests in clinics, purification of drinking water, manufacturing of sugar, pharmaceuticals and cosmetics industries, effluent treatment plants, dyes and chemicals plants, biotechnology laboratory, electroplating centers, food and beverage industries, circuit board etching laboratories, flue gas scrubbers, boilers and cooling towers, pulp and paper manufacturing industries and fermentation (wine, beer, alcohol) centers.

A pH meter measuring the gastric of patients is explained in D. Meiners et.al [2]. S.J. Taylor et.al [3] explains how to test a pH for a nasogastric tube. For improved performance, pH probes are used to measure the intragastric of patients, which is explained in R.L. Levine et.al [4] and A. Baghaie et.al [5]. However the above systems are quite costly and complex and involve fabrication processes.

This paper's objective is to develop a typical pH meter, which is a microcontroller based digital pH meter. The output of the microcontroller is displayed as a pH value by the seven segment display throughout BCD to the seven segment decoder. The pH probe technique for intragastric pH measurement appears to be straightforward in a technical sense and it is applicable for patients at risk of stress ulcer bleeding.

1. *M. A. A. Mashud is with the Department of Applied Physics, Electronics and Communication Engineering, Islamic University, Kushtia-7003, Bangladesh. E-mail: ms.mashud@yahoo.com*
2. *M. A. Masud is with the Department of Computer Science and Information Technology, Patuakhali Science and Technology University, Dumki, Patuakhali, Bangladesh*
3. *Md. Serajul Islam is with the Institute of Electronics, Atomic Energy Research Establishment, Savar, Dhaka, Bangladesh*

Manuscript received on 30 July 2011 and accepted for publication on 31 October 2011.

2 Design

The system is divided into six parts: the low voltage power supply, sensor circuit, buffer amplifier, summing amplifier, microcontroller unit and display circuit. Low voltage power supply produces 5 volts for the buffer amplifier circuit, summing amplifier and microcontroller. The signal from pH electrode goes to the buffer amplifier circuit. The amplified signal is the input of the summing amplifier, which goes to the microcontroller. The output of the microcontroller operates the display circuit. The block diagram and the complete circuit diagram of the developed system are shown in Figure 1 and Figure 2 respectively.

2.1 Low voltage power supply

The microcontroller, BCD to seven segment decoder and other electronic components are used in designing the complete pH meter, and require a dc voltage (+5v & -5v). A highly stable regulated dc power supply was designed for this purpose. The complete circuit of a regulated dc power supply is shown in Fig 2, using IC1 and IC2 as a voltage-regulating device [6]. It contains four diodes, D1, D2, D3 and D4, which are connected to the a.c. supply [7] for +5V. Similarly, D5, D6, D7 and D8 are connected to the a.c. supply for -5V.

2.2 Buffer Amplifier

The buffer amplifier [8] circuit consists of IC3 and VR1. The signal from the pH electrode is connected to pin 3 of IC3. VR1 is connected between pin 1and 5 for a null setting.

© 2011 ULAB JSE

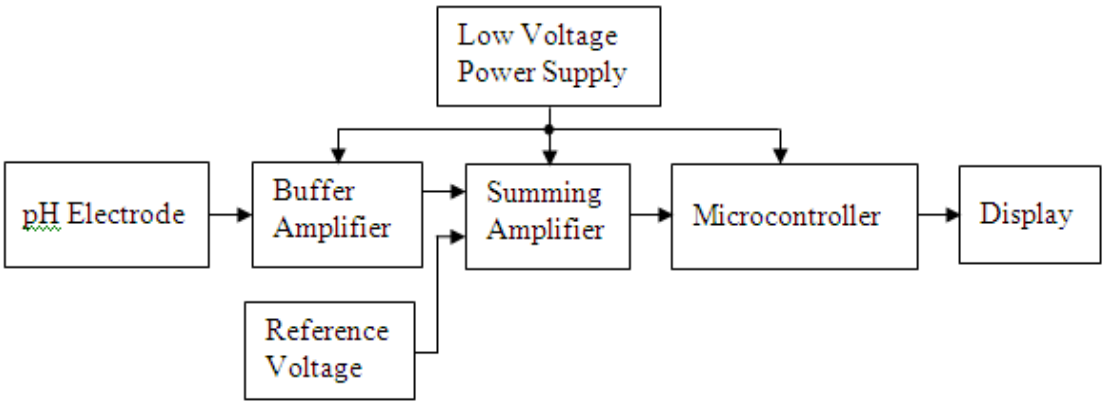

Figure 1: Block diagram of the developed system

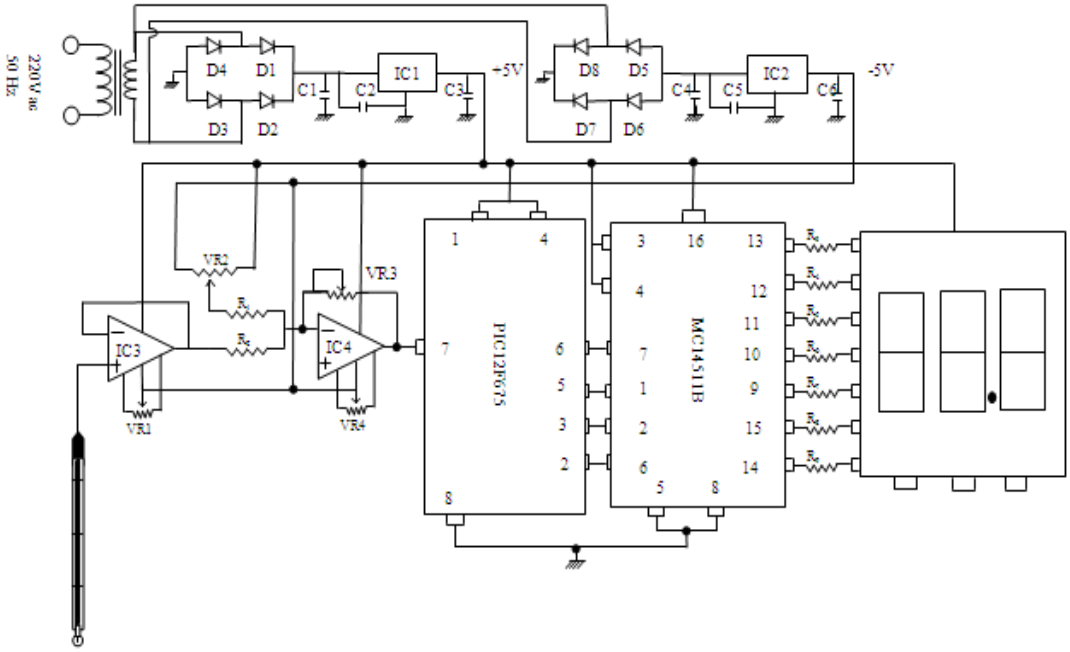

Figure 2: Complete circuit diagram of the developed system

2.3 Summing amplifier

The summing amplifier [9] consists of IC4, VR2, VR3, VR4, R1 and R2. The output of the summing amplifier is used as a microcontroller. This system uses two input summing amplifiers with inverting configuration.

2.4 Microcontroller Unit

The output of the summing amplifier is connected to microcontroller PIC12F675. The microcontroller converts data from analogue to digital, analyses data and displays data. Pin diagrams of microcontroller PIC12F675 are shown in Figure 3.

The PIC12F675 is an 8-pin package [10]. It has an A/D converter with 10-bit resolution. A "C" language program was developed to control the function of the microcontroller, using PCWH Compiler [11].

2.5 Display System

Three common cathode 7-segment LED modules display the pH value of the solution. Efficiently using the pin of PIC microcontroller allows for the display to be accomplished with a BCD 7-segment decoder (MCI4511B) [12]. The microcontroller sends the output signal to the input pins 7,1,2,6 of BCD to the seven segment decoder, whose

output pins 13,12,11,10,9,15,14 are connected to the input of common anode seven segment LED[13].

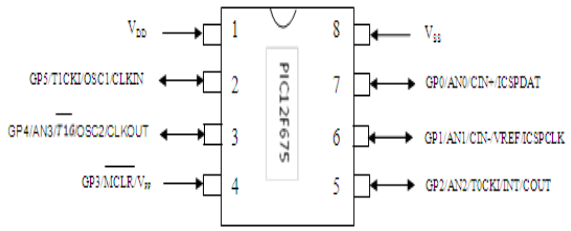

Figure 3: Pin diagram of microcontroller PIC12F675

3 System Program

The system program is depicted in the flow chart below:

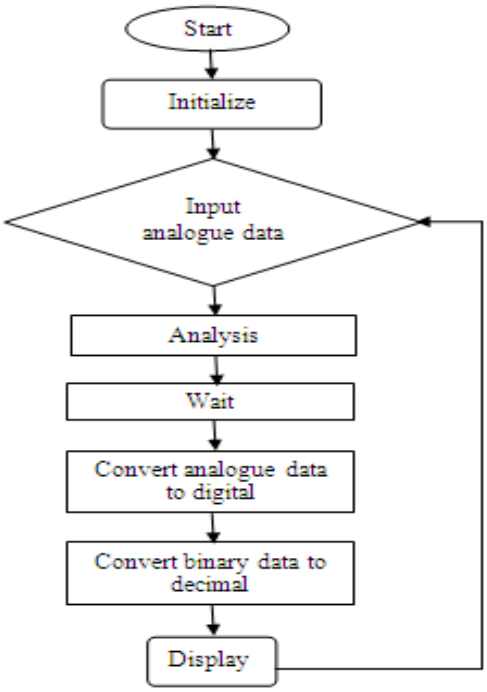

Figure 4: Flow chart of the system program

4 Results and Discussion

The microcontroller based digital pH meter was successfully designed and developed, as its performance was strong. The result of pH is compared with the actual result. The model of the laboratory pH meter is PHM83, with an accuracy of +/-0.1%. Figure 5 provides a graphic representation of the comparison between the designed system and the laboratory pH meter. The graph illustrates that the developed system has sound stability and accuracy.

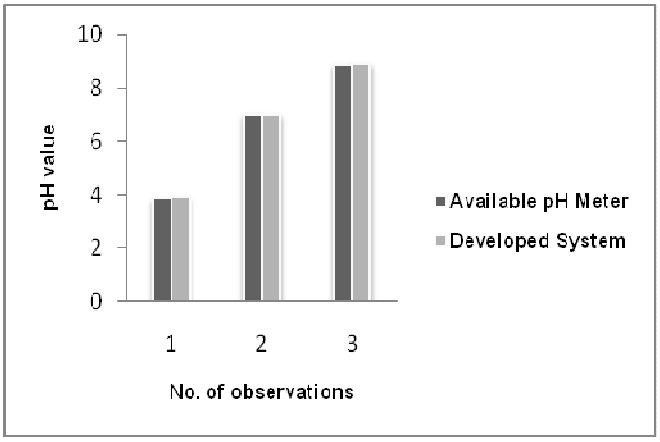

Figure 5: Graphic representation of a comparison of the two systems

Our designed pH meter was tested in the pathological unit of Gono Bishwabidyalay. Fifteen patients (seven male, eight female) took part in our study. The patients' demographics are contained in Table 1.

TABLE 1
PATIENTS' DEMOGRAPHICS

Patient No.	Gender	Age (Yr)	Weight (Kg)	'gastric pH
1	Female	23	59	3.1
2	Male	26	70	3.3
3	Female	28	62	2.9
4	Female	25	61	2.4
5	Female	53	69	1.7
6	Female	40	64	1.3
7	Male	67	60	3.1
8	Male	69	63	2.1
9	Male	60	59	2.3
10	Male	63	72	1.23
11	Female	56	68	0.99
12	Male	27	64	1.21
13	Female	25	60	1.05
14	Male	55	65	2.08
15	Female	46	70	1.53

If successful treatment depends on accurate intragastric pH measurement, the probe method may be preferable to the conventional aspiration method. A study by Lugo et al. concluded that gastric pH should be monitored by nanogastric pH probe and the dose of ranitidine adjusted accordingly [14].

The advantages include a reduction in the number of tubes passed into the stomach, improved patient comfort levels, and the possibility of decreased tube-related esophagitis. A single tube can provide long-term pH monitoring and gastric feeding/decompression. An additional advantage of the combination pH probe-NG tube is its ability to obtain measurements without handling gastric secretions. This decreases the exposure of hospital personnel to potentially infectious agents. The new technique for obtaining intra-gastric pH measurements appears technically simpler, clinically applicable, and potentially more accurate than conventional monitoring of gastric contents by aspiration and testing with pH paper. The technical specifications of the developed digital pH meter are provided in Table 2.

TABLE 2

SPECIFICATION OF THE DIGITAL PH METER

Technical Specifications	
Power Requirements	230 V ac ±10%, 50 Hz
Range	0.0 to 14.0 pH
Accuracy	+/- 0.1 pH
Probe	pH electrode
Display	Seven Segment Display
Relative Humidity	5 to 90% non-condensing

5 CONCLUSION

The price of electronic equipments has fallen significantly in recent times, though the cost of medical equipment remains expensive. However due to the rapid development of micro electronics, all the designed component and instruments are available at a lower price. The device is reliable in operation and it costs approximately U$100 for fabrication, whereas the price of a similar instrument in the international market is no less than U$500. Moreover, the comparison of the features of the presently used system shows that the developed system is a better choice in terms of cost, portability and design. Therefore, the opportunity to use the designed instruments will be open to many users, particularly in developing countries.

REFERENCES

[1] www.clarksonlab.com/vAnas.pdf ; Cole-Parmer catalog 97- 98.

[2] D. Meiners, S. Clift and D. Kaminski, "Evaluation of various techniques to Monitor Intragastric pH," Arch Surg 117(3): 288 291, 1982.

[3] S.J. Taylor, R. Clemente, "Confirmation of nasogastric tube position by pH testing," J Hum Nutr Diet, 18(5):371- 375, 2005.

[4] R.L. Levine, RE Jr. Fromm and M. Mojtahedzadeh, "Equivalence of litmus paper and intragastric pH probes for intragastric pH monitoring in the intensive care unit," Crit Care Med, 22(6): 945-948, 1994.

[5] A.A .Baghaie, M. Mojtahedzadeh and RL. Levine, "Comparison of Intermittent administration and continuous infusion of famotidine on gastric pH in critically ill patients: results of a prospective, randomized, crossover study," Crit care Med, 23(4):687-691, 1995.

[6] "Farnell Semiconductor Data CD-ROM," Data sheet 2143.pdf, 7805IC, 7905IC, Issue 7 January 2000.

[7] V.K. MEHTA, "Principles of Electronics," Revised edition, page-150.

[8] R.F. Coughlin and F. F. Driscoll "Operational Amplifiers and Linear Integrated Circuits," Second Edition

[9] R. A. Gayakward, "Op-Amps and Linear Integrated Circuits," Fourth Edition.

[10] http://www.microchip.com/downloads/en/devicedoc/41190c.pdf

[11] PCWH Compiler®IDE, Version 3.43, www.ccsinfo.com

[12] "Farnell Semiconductor Data CD-ROM,"Data sheet 6365001. Issue 7 January 2000.

[13] R.S International Electronic Cataloge, March 2003. R.A. Lugo AM. Harrison, J. Cash, "Pharmacokinetics and pharmacodynamics of ranitidine in critically ill children," Crit Care Med, 29(4):759-764, 2001.

M. A. A. Mashud was born on Nov.15, 1980 in kushtia, Bangladesh. He received the B.Sc. (Hons) degree in Applied Physics, Electronics and Communication Engineering (AECE) from Islamic University, Kushtia, Bangladesh in 2003, and M.Sc degree from the same department in 2004. He was a Lecturer in the department of Medical Physics and Biomedical Engineering at Gono Bishwabidyalay, Bangladesh from 2008 to 2010. He is currently a Lecturer in the department of AECE, Islamic University, Bangladesh. His current interest is microprocessor / microcontroller applications in control, automation, medical instruments, environmental monitoring, low cost electronic systems and assessment.

M. A. Masud was born on Nov. 08, 1982 in Meherpur, Bangladesh. He received the M.Sc. degree in Information and Communication Engineering from Islamic University, Kushtia, Bangladesh in 2004. He is an Assistant Professor in the department of Computer Science & Information Technology, Patuakhali Science and Technology University, Bangladesh. He works currently as a Ph.D. student in the School of Shinawatra University, Thailand.

Md. Serajul Islam was born in Panchagar, Bangladesh. He received the M.Sc. degree in Physics from Rajshahi University, Bangladesh. He was a Chief Scientific Officer and Director in the Institute of Electronics, AERE, Atomic Energy Commission, Savar, Bangladesh. Now he is retired. His work is design, development and analysis of electronic instruments and reactor control. His work has produced nearly 65 peer-reviewed scientific papers and 02 patents.

Fast Holographic Image Reconstruction using Graphics Processing Unit

Mohammad Shorif Uddin, Madeena Sultana, Md. Ziarul Islam

Abstract— Although recent holographic image capturing technology produces high resolution and high-fidelity images, reconstruction technology is yet to be fully developed. Digital reconstructions of optically captured holograms are highly expensive in terms of computation time. This paper describes a fast holographic image reconstruction process using NVIDIA's Compute Unified Device Architecture (CUDA) enabled Graphics Processing Unit (GPU). This parallel processing technique speeds up computation to perform faster Fourier transform for the reconstruction of digital holographic images. Our method on CPU and GPU platforms is measured and compared in terms of its efficiency. The experimental results demonstrate its improved performance over a factor of 3, as compared with CPU for a holographic image of size (512×512) pixels.

Keywords—Digital Holography, Computer Holography, CUDA, FFT, GPU, Hologram Reconstruction

1 Introduction

DIGITALLY reconstructing holographic images involves acquiring and processing holographic measurement data, which is recorded by CCD cameras or similar devices. It has a broad spectrum of applications, including high-resolution imaging, information processing, holographic interferometry and vibration analysis. Digital holography includes the numerical realization of the diffracted integral, unlike an optical reconstruction. The process of optical recording of the holograms onto photoplates or photothermoplastic film, and optical reconstruction is highly complex and time-consuming. Therefore, digitally recording primary holograms and digitally reconstructing recorded data provides a significant advantage to holographic metrology.

Digital holography for large volumes of 3D objects was first proposed by Kreis and Jüptner's research team [1]-[3]. A holographic method for depth measurement of small particles distributed in 3D space was proposed by Murata and Yasuda [4]. E. Cuche, P. Marquet, and C. Depeursinge [5] proposed a technique where off-axis holograms are numerically reconstructed with a calculation of scalar diffraction in the Fresnel approximation. A digital micro-mirror device (DMD) was used for real-time display of interferometric fringes in hologram reconstruction by Thomas Kreis, Petra Aswendt, and Roland Höfling [6]. B. Javidi and E. Tajahuerce [7] presented a technique of digital holography to obtain three-dimensional (3D) pattern recognition. A technique for controlling the size of amplitude and phase images, reconstructed from digital holograms using Fresnel-transform method was proposed by Ferraro et al. [8]. An algorithm that allows for the reconstruction of digital color holograms with adjustable magnification is proposed and demonstrated by Fucai Zhang, Ichirou Yamaguchi, and L. P. Yaroslavsky [9]. Nicola et al. [10] developed a new technique based on the angular spectrum of plane waves for numerically reconstructing digital holograms on tilted planes.

Due to high computational requirements, different approaches for accelerating the hologram computation were employed. Fast hardware is exploited, along with accelerated algorithms. A number of algorithms, such as a different approximation for computing the light field in Fourier and Fresnel holograms [11], the use of horizontal parallax for display applications [12], the special formulas for fast calculation of optical diffraction on tilted planes [13] and a large number of heuristics methods [14], [15] were proposed to accelerate computation. Specialized and general purpose hardware has been used to speed up computation. For example, Watlington et al. [16] at MIT employed a hardware architecture, Satake et al. [17] used a 128 processor machine, Ito et al. [18] exploited FPGA-based HORN architecture and Haist et al. [19] began to use graphic processing units (GPUs) for fast computation of holograms. Since 2007, the use of GPUs to accelerate computation became especially interesting, as NVIDIA introduced CUDA (Compute Unified Device Architecture) enabled GPUs. This provided massive parallel computation power. The exciting new technology leverages the parallel computation more efficiently than a CPU [20]. A significant amount of research is currently exploiting this processing power for faster computation of hologram reconstruction [21]-[23].

This paper describes the implementation of fast digital hologram generation on a central processing unit (CPU) and a CUDA enabled graphics processing unit (GPU).

- *Mohammad Shorif Uddin, Computer Science and Engineering Department, Jahangirnagar University, Savar, Dhaka, Bangladesh. E-mail: shorifuddin@gmail.com.*
- *Madeena Sultana, Computer Science and Engineering Department, University of Liberal Arts Bangladesh, Dhanmondi, Dhaka, Bangladesh. E-mail: madeena.sultana@ulab.edu.bd.*
- *Md. Ziarul Islam, Computer Science and Enginering, Daffodil International University, Dhaka, Bnagladesh.*

Manuscript received on 30 July 2011 and accepted for publication on 31 October 2011.

© 2011 ULAB JSE

2 HOLOGRAPHIC IMAGE AND RECONSTRUCTION

The simple and effective 3D imaging technique, digital holography, is based on interference patterns between scattered and unscattered light. It has diverse applications in particle image velocimetry (PIV) to 3D microscopic imaging. Fig. 1 shows an in-line digital holographic experimental setup.

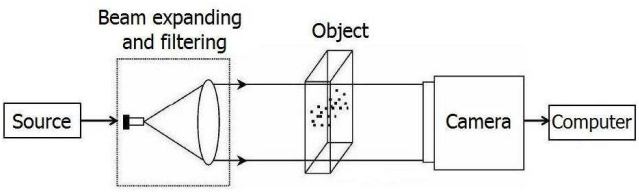

Figure 1: In-line digital holographic experimental setup.

The aperture can be expressed as:

$$g(\xi,\eta)=\begin{cases}1 & \text{for aperture}\\ 0 & \text{otherwise}\end{cases} \tag{1}$$

The light amplitude, h at an arbitrary point on the plane x-y is expressed in the following equation:

$$h(x,y)=\frac{1}{j\lambda}\int_{-\infty}^{\infty}\int_{-\infty}^{\infty} g(\xi,\eta)\frac{e^{j(2\pi/\lambda)L}}{L}d\xi d\eta \tag{2}$$

The distance L between an arbitrary pair of points on an aperture and a screen can be expressed as:

$$L=\sqrt{z^2+(x-\xi)^2+(y-\eta)^2} \tag{3}$$

Here, λ is the wavelength of illuminating light and j denotes the imaginary unit. In order to obtain reconstructed images from a hologram, numerous computations for the Fresnel diffraction are required. The Fresnel diffraction formula can be expressed as:

$$h(x,y,z;g(\xi,\eta))=\frac{1}{j\lambda z}e^{j(2\pi/\lambda)(z+(x^2+y^2)/2z)}$$

$$\int_{-\infty}^{\infty}\int_{-\infty}^{\infty} g(\xi,\eta)e^{j(2\pi/\lambda)((\xi^2+\eta^2)/2z)}e^{j(2\pi/\lambda)((\xi x+\eta y)/z)}d\xi d\eta \tag{4}$$

The interference fringes are expressed in the following equation:

$$I_d = h_d h_d^* \tag{5}$$

Where I_d is light intensity and h_d is light amplitude on the hologram plane and the asterisk represents the complex conjugate. h_d can be expressed as:

$$h_d = h(x,y,d;g(\xi,\eta)) \tag{6}$$

Fig. 2 depicts the recording and reconstruction stages of in-line holography.

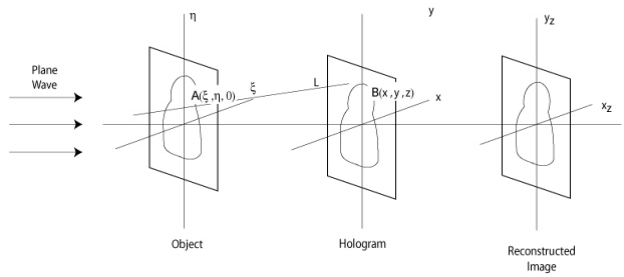

Figure 2: Recording and reconstruction of in-line digital holographic image.

According to Kreis et al. (4) it can be expressed as follows:

$$h(x,y,d;g(\xi,\eta))$$

$$=\int_{-\infty}^{\infty}\int_{-\infty}^{\infty} g(\xi,\eta)\frac{1}{j\lambda\pi}e^{j(2\pi/\lambda)(z+(\xi-x)^2+(\eta-y)^2/2z)}d\xi d\eta$$

$$=\int_{-\infty}^{\infty}\int_{-\infty}^{\infty} g(\xi,\eta)g_F(x-\xi,y-\eta)d\xi d\eta$$

$$=F^{-1}[F(g)F(g_F)] \tag{7}$$

The above approach requires one Fourier transform and one inverse Fourier transform. In our approach, $F(g_F)$ is computed numerically. Fig. 3 depicts the reconstruction of a full volume holographic image [4].

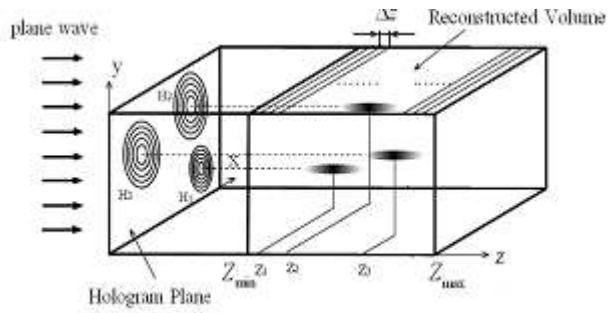

Figure 3: Full volume digital holographic reconstruction.

Our computation considers, λ=0.6328 μm, pixel resolution, dx=dy= 2 nm. We varied the reconstruction depth z from 4116 μm to 4250 μm with an interval of 1 μm. Thus, there are 135 z-sections.

The most significant limitation of digital holography is the enormous processing power, memory and storage requirements for holographic reconstructions. This is because each hologram requires the reconstruction of a 3D volume of about a thousand different z-sections. Usually, Fresnel diffraction computation is accelerated by the FFT. However real-time reconstruction from a hologram is extremely challenging, even when a faster CPU is utilised. For this reason, a real-time computation system is a critical necessity. Graphics processing unit (GPU) [24], [25] can overcome this problem. GPU uses a multiple-threading technique to achieve computation in parallel.

By overcoming this limitation, digital holography will replace the most expensive confocal microscopy for biological imaging in the cellular level. Fig 4. depicts a block diagram of the computation algorithm for holographic reconstruction.

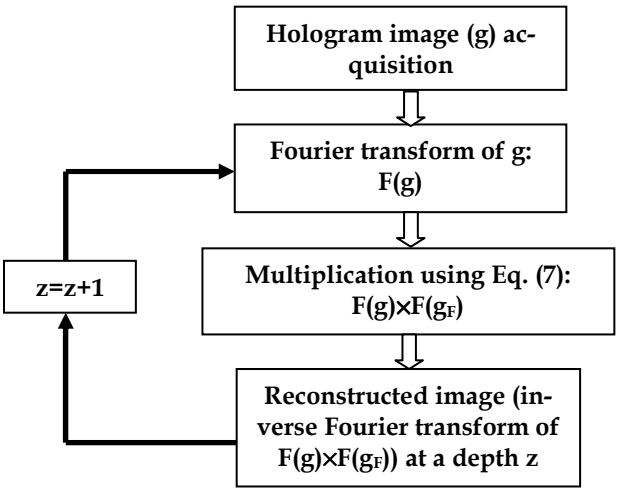

Figure 4: Computation algorithm.

3 CUDA Overview

The CUDA platform is currently the focus of much attention, due to its tremendous potential for parallel processing. In November 2006, NVIDIA introduced CUDA with a new parallel programming model and instruction set architecture to solve the many complex computational problems [20]. Each CUDA complainant device contains a set of multiprocessor cores, and each core possesses SIMT (Single Instruction, Multiple Thread) architecture. Today four quad-core CPUs can run only 16 threads concurrently, whereas the smallest executable parallel unit on a CUDA device is comprised of 32 threads. All CUDA enabled NVIDIA GPUs support at least 768 concurrently active threads per multiprocessor. Moreover, some GPUs support 1,024 or more active threads per multiprocessor [20].

The performance of recent NVIDIA GPUs is comparable with a supercomputer. For example, NVIDIA GTX280 GPU has 240 processing cores, with 1 TFlops (10^{12} floating point operations per second) of computation power with 1GB onboard device memory. The 240 cores of GTX280 are grouped into 30 multiprocessors, each comprising 8 cores [24]. A parallel implementation of an application on a GPU can achieve more than 100 times speedup than CPU execution [25].

SIMT architecture of CUDA allows a portion of a parallel application to be executed independently many times on different data, with many threads running on different processors, at any given clock cycle. This parallel portion can be isolated into a function known as kernel. A kernel is organized as a set of thread blocks. Each thread block is, in turn, organized as a three-dimensional array of threads. Typically, each thread block may contain 128 threads, 256 threads, 512 threads, or as many as 768 threads. Threads within the same block efficiently cooperate through shared memory and synchronize with each other. Each thread has a unique thread ID, which is defined by the three thread indices: threadIdx.x, threadIdx.y and threadIdx.z. Each block is identified by a unique, two-dimensional coordinate given by CUDA specific keywords blockIdx.x and blockIdx.y. Each block must have an equal number of threads that are organized in exactly the same manner. The use of multidimensional identifiers simplifies memory addressing of multidimensional data. The block and grid dimensions, collectively known as execution configuration, can be set at run-time.

A kernel is executed as a grid of parallel threads. Typically, each grid contains thousands to millions of lightweight GPU threads per kernel invocation. This facilitates a large amount of data parallelism. The hierarchy of grid, blocks and threads is depicted in Fig. 5.

GPU memory referred as device memory includes three types: global memory, constant memory and texture memory. Microprocessors of GPU have 4 types of on-chip memory: registers, shared memory, constant cache and texture cache. Cached shared memory enables the threads within a block to cooperate with each other. However, a major limitation is the lack of similar mechanisms for block cooperation. On the other hand, global memory is uncached. Therefore, accessing global memory is costly. CUDA programming requires a single program which encompasses both host and device codes written in C/C++ with some extensions [20]. The portions that exhibit little or no data parallels are implemented in the host code, whereas portions containing rich amounts of data parallelism are implemented in the device code.

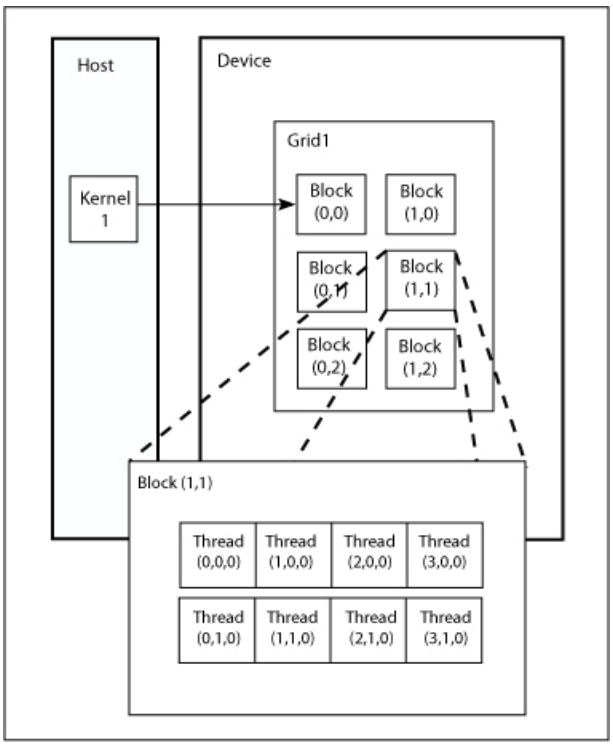

Figure 5: Hierarchy of grid, threads, and blocks.

During compilation, the NVIDIA C compiler (nvcc) separates the host code and device code. The host code is then compiled with the host's standard C compilers and runs as an ordinary CPU process. The device code is further compiled by the nvcc and executed on a GPU device.

4 Computation on CUDA

The holograms are computed on NVIDIA GeForce 8 platform, using GPUmat [26]. GPUmat is a freeware developed by GP-You Group, and allows users to directly access GPU's parallel computing power in MATLAB. GPUmat library [27] is designed to be integrated with MATLAB and provides basic functions for handling calculations on GPU. With the aid of GPUmat, programs are easily converted to run on the GPU.

We employed CUFFT [28] library to perform the Fourier transforms. The CUFFT library provides a simple interface for computing parallel FFTs on NVIDIA GPUs. The CUDA library is exceptionally fast for FFT computation. For the two dimensional complex 512×512 FFTs, performance improves at a factor of more than 100 when using CUFFT library.

5 Results and Discussion

Digital in-line holography suffers from a high computational burden, as thousands of z-sections are required for 3D reconstruction. To overcome the burden, GPU was employed to compute FFT and IFFT for 135 z-sections to reconstruct a 3D hologram image. Table 1 illustrates the overall computation speedup in GPU over CPU, while Table 2 provides a comparison of reconstruction time for CPU and GPU with an increasing number of iteration. Fig. 6 contains a graphic representation of Table 2.

TABLE 1
Computation Time Speedup

	CPU (seconds)	GPU (seconds)	Speedup
Total computation time (for 135 z-sections)	18.1595	5.3020	3.425028
FFT (for 1 z-section)	0.0546	0.0262	2.083969
IFFT(for 1 z-section)	0.0430	0.0135	3.185185

TABLE 2
Comparison of Reconstruction Time on CPU and GPU with Increasing No. of Iterations

No. of Iteration	CPU time (seconds)	GPU time (seconds)	Speedup
14	1.9229	0.7078	2.716728
27	3.6516	1.1943	3.057523
68	8.8188	2.7300	3.230330
135	18.1595	5.3020	3.425028

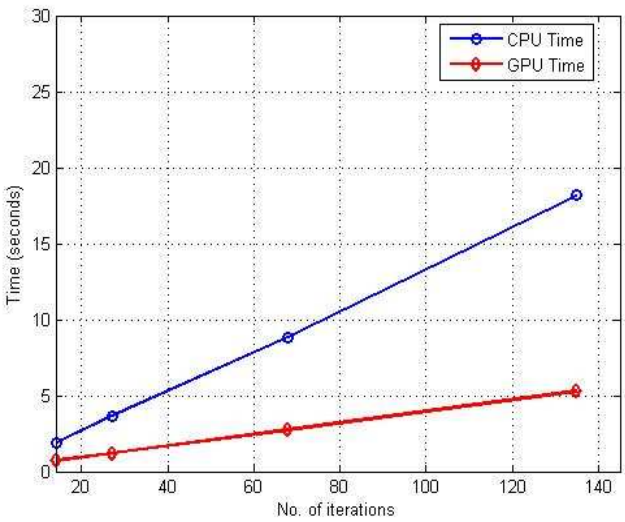

Figure 6: Computation time comparison for increasing the numbers of iterations.

Fig. 7 presents the hologram input image and reconstructions at different depths, z. Here, the image size is (512×512) pixels and the hologram images are reconstructed at different depths, from 4116 µm to 4236 µm, with an interval of 1 µm. A speedup of 3.5x was achieved over CPU computation.

The main drawback of GPU computation is the transfer time required between the host memory and device memory. Copying data from the host's memory to GPU's global memory requires a large fraction of the total execution time. Therefore, the data transfer time is excluded from execution time, a significant speedup is achieved with a large database. A further limitation is that only the more recent NVIDIA GPUs support double precision arithmetic. We used NVIDIA GeForce 8500GT, which supports single precision computation. Since MATLAB's default is double precision, it was necessary to convert data before and after each data transfer. This added an overhead to our application. However the accuracy of the algorithm for single-precision and

double-precision arithmetic is evaluated. The quality of the reconstruction from the algorithm using single-precision arithmetic on GPU is comparable with the quality from the double-precision arithmetic on CPU. Thus the implementation using single-precision arithmetic on a GPU platform can be used for holographic reconstruction.

6 Computation Environment

Each test was executed on Intel Pentium 4 (host) and NVIDIA GeForce 8500GT (device). Tables 3 and 4 list the host and device specifications, respectively.

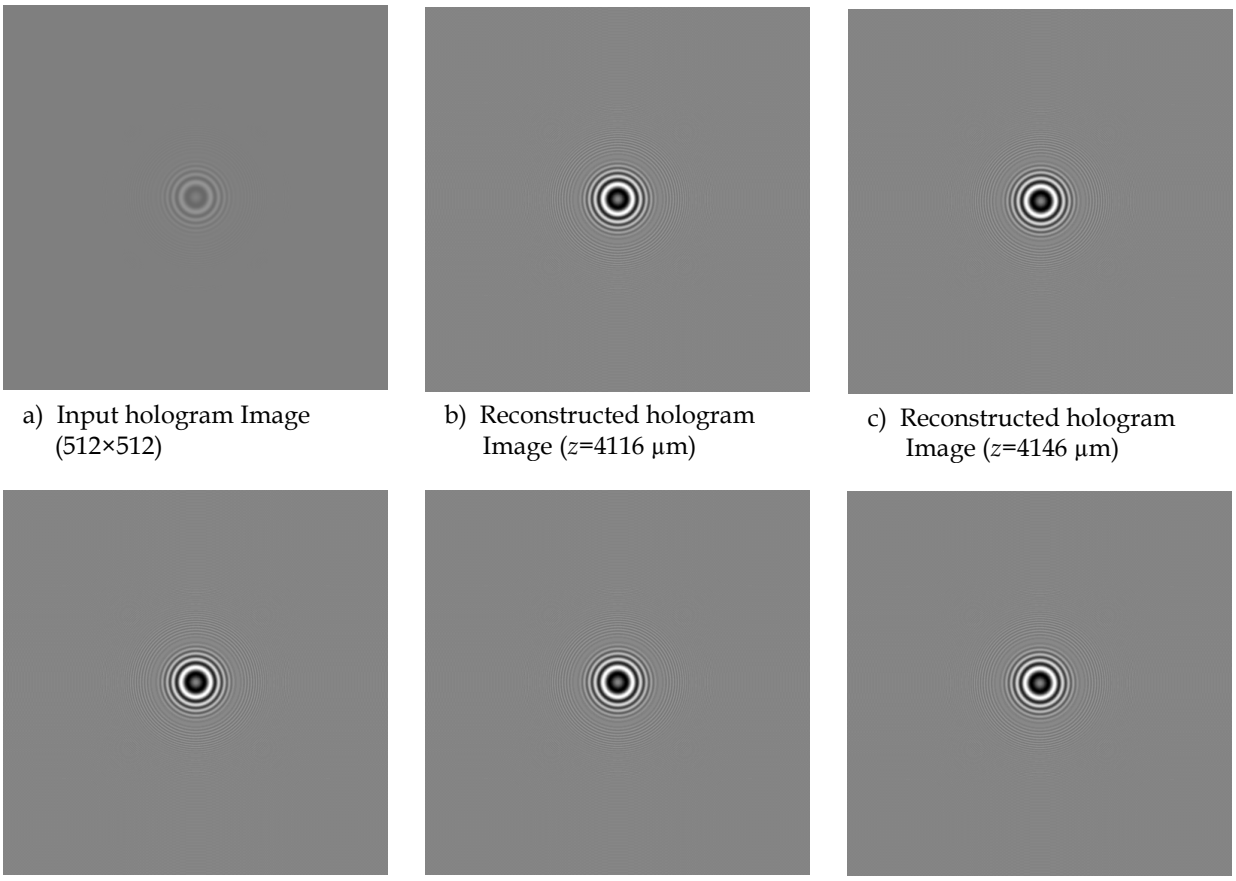

a) Input hologram Image (512×512)

b) Reconstructed hologram Image (z=4116 μm)

c) Reconstructed hologram Image (z=4146 μm)

d) Reconstructed hologram Image (z=4176 μm)

e) Reconstructed hologram Image (z=4206 μm)

f) Reconstructed hologram Image (z=4236 μm)

Figure 7: Hologram input image and reconstructions at different depths, z.

TABLE 3
HOST SPECIFICATION

Processor	Intel Pentium 4, 3.00 GHz
No. of Cores in processor	1
No. of Threads in processor	2
Memory	512 MB, 268.0 MHz, DDR2
Motherboard	Gigabyte Technology Co. Ltd, 945 GZM-S2

TABLE 4
DEVICE SPECIFICATION

Processor	NVIDIA GeForce 8500GT
Cores	16
Maximum threads per block	512
Total global memory	512 MB
Shared memory per block	16 K
Registers per block	8192
Wrap size	32
Total constant memory	64 K

7 CONCLUSIONS

Efficient hologram computations are essential to diversified applications. Although numerically efficient image reconstruction algorithms currently exist, real time reconstruction is unfeasible on standard CPUs. This paper presents a GPU based 3D hologram reconstruction. Our experimental results demonstrate that the hologram computation with iterative Fourier transform is faster using the GPU than the CPU. Our GPU based computation is approximately 3.5 times faster than CPU computation. In addition, this technique could be further extended on a multi-GPU platform. Due to the high speed of calculations, we propose that the ideas presented in this paper may have widespread applications in these areas.

ACKNOWLEDGMENT

The authors wish to thank Professor S. Murata of Kyoto Institute of Technology, Kyoto, Japan for providing the hologram image of flow particles.

REFERENCES

[1] Thomas M. Kreis, Mike Adams, Werner P. O. Jüptner, "Methods of Digital Holography: A Comparison," Proc of *SPIE*, vol. 3098, pp. 224–233, 1997.

[2] M. Dams, Th. Kreis, and W. Jüptner, "Particle Size and Position Measurement with Digital Holography," *Proc. of European symposium on lasers and optics in manufacturing, Proc. of SPIE*, vol. 3098, pp. 234-240, 1997.

[3] U. Schnars and W. Jüptner, "Direct Recording of Holograms by a CCD Target and Numerical Reconstruction," *Appl. Opt.*, vol. 33, pp. 179-181, 1994.

[4] Shigeru Murata and Norifumu Yasuda, "Potential of Digital Holography in Particle Measurement," *Optics & Laser Technology*, vol. 32, Issues 7-8 pp. 567-574, Oct. 2000.

[5] E. Cuche, P. Marquet, and C. Depeursinge, "Spatial Filtering for Zero-Order and Twin-Image Elimination in Digital Off-Axis Holography," *Appl. Opt, vol.* 39, pp. 4070-4075, 2000.

[6] Thomas Kreis, Petra Aswendt, and Roland Höfling, "Hologram Reconstruction using a Digital Micromirror Device", *Opt. Eng.* vol. 40, issue 6, pp. 926-933; 2001.

[7] B. Javidi and E. Tajahuerce, "Three-dimensional Object Recognition by use of Digital Holography," *Opt. Lett.*, vol. 25, pp.610-612, 2000.

[8] Pietro Ferraro, Sergio De Nicola, Giuseppe Coppola, Andrea Finizio, Domenico Alfieri, and Giovanni Pierattini, "Controlling Image Size as a Function of Distance and Wavelength in Fresnel-transform Reconstruction of Digital Holograms," *Opt. Lett.* , vol. 29, pp. 854-856, 2004.

[9] Fucai Zhang, Ichirou Yamaguchi, and L. P. Yaroslavsky, "Algorithm for Reconstruction of Digital Holograms with Adjustable Magnification," *Opt. Lett.* , vol. 29, pp. 1668-1670, 2004.

[10] Sergio De Nicola, A. Finizio, G. Pierattini, P. Ferraro, and D. Alfieri, "Angular Spectrum Method with Correction of Anamorphism for Numerical Reconstruction of Digital Holograms on Tilted Planes," *Opt. Express,pp.* 13, pp. 9935-9940, 2005.

[11] M. L. Tachiki, Y. Sando, M. Itoh, and T. Yatagai, "Fast Calculation Method for Spherical Computer-Generated Holograms," *Appl. Opt.*, vol. 45, pp. 3527-3533, 2006.

[12] V. M. Bove, Jr., W. J. Plesniak, T. Quentmeyer and J. Barabas "Real-Time Holographic Video Images with Commodity PC Hardware," *Proc. SPIE* 5664A, 2005.

[13] K. Matsushima, H. Schimmel, and F. Wyrowski, "Fast Calculation Method for Optical Difraction on Tilted Planes by use of the Angular Spectrum of Plane Waves," *J. Opt. Soc.* Am. A 20, pp. 1755-1762, 2003.

[14] B. B. Chhetri, S. Yang, and T. Shimomura, "Stochastic Approach in the Efficient Design of the Direct-Binary-Search Algorithm for Hologram Synthesis," *Appl. Opt.*, vol. 39, pp. 5956-5964, 2000.

[15] J. -H. Li, K. J. Webb, G. J. Burke, D. A. White, and C. A. Thompson, "Design of Near-field Irregular Diffractive Optical Elements by use of a Multiresolution Direct Binary Search Method," *Opt. Lett.*, vol. 31, pp. 1181-1183, 2006.

[16] J. A. Watlington, M. Lucente, C. J. Sparrell, V. M. Bove, Jr., and I. Tamitani. "A hardware Architecture for Rapid Generation of Electro-holographic Fringe Patterns," *Proc. SPIE* 2406-23, pp. 172-183, 1995.

[17] S. Satake, H. Kanamori, T. Kunugi, K. Sato, T. Ito, and K. Yamamoto, "Parallel Computing of a Digital Hologram and Particle Searching for Microdigital-holographic Particle-tracking Velocimetry," *Appl. Opt.*, vol. 46, pp. 538-543, 2007.

[18] T. Ito, N. Masuda, K. Yoshimura, A. Shiraki, T. Shimobaba, and T. Sugie, "Special-purpose Computer HORN-5 for a Real-time Electro-holography," *Opt. Express, vol.* 13, pp. 1923-1932, 2005.

[19] Haist, T., Reicherter, M., Min Wu, Seifert L., "Using Graphics Boards to Compute holograms," *Computing in Science & Engineering*, vol. 8, pp. 8-14, 2006.

[20] "NVIDIA CUDA C Programming Guide 4.0," Available at http://developer.nvidia.com/cuda-toolkit-3.1-downloads, accessed July 02, 2011.

[21] H. Kang, F. Yaraş, and L. Onural, "Graphics Processing Unit Accelerated Computation of Digital Holograms," *Appl. Opt.*, vol. 48, pp. 137-143, 2009.

[22] Rick H.-Y. Chen and Timothy D. Wilkinson, "Computer Generated Hologram from Point Cloud using Graphics Processor," *Appl. Opt.* vol. 48, pp. 6841-6850, 2009.

[23] S. Bianchi and R. Di Leonardo, "Real-time Optical Micromanipulation using Optimized Holograms Generated on the GPU," *Computer Physics Communications*, vol. 181, issue 8, pp. 1444-1448, August 2010.

[24] "CUDA C Best Practices Guide," Available at http://developer.nvidia.com/cuda-toolkit-4.0-downloads, accessed July 01, 2011.

[25] David B. Kirk and Wen-mei W. Hwu, *Programming Massively Parallel Processors- A Hands-on Approach*, Elsevier Inc., USA, January 2010.

[26] "GPUmat: a GPU toolbox for MATLAB," Available at http://gp-you.org/, accessed July 01, 2011.

[27] "GPUmat user guide version 0.26," Available at http://gp-you.org/, accessed July 02, 2011.

[28] NVIDIA CUDA CUFFT library, http://developer.download.nvidia.com/compute/cuda./CUFFT-Library-3.0.pdf, accessed July 02, 2011.

Mohammad Shorif Uddin received his PhD in Information Science from Kyoto Institute of Technology, Japan, Masters of Education in Technology Education from Shiga University, Japan and Bachelor of Science in Electrical and Electronic Engineering from Bangladesh University of Engineering and Technology (BUET). He joined the Department of Computer Science and Engineering, Jahangirnagar University, Dhaka in 1992 and currently serves as a Professor of this department. He began his teaching career in 1991 as a Lecturer of the Department of Electrical and Electronic Engineering, Chittagong University of Engineering and Technology (CUET). He undertook postdoctoral research at Bioinformatics Institute, A-STAR, Singapore, Toyota Technological Institute, Japan and Kyoto Institute of Technology, Japan. His research is motivated by applications in the fields of computer vision, pattern recognition, blind navigation, bio-imaging, medical diagnosis and disaster prevention. He has published a remarkable number of papers in peer-reviewed international journals and conference proceedings. He holds two patents for his scientific inventions. He received the Best Presenter Award from the International Conference on Computer Vision and Graphics (ICCVG 2004), Warsaw, Poland. He is the co-author of two books. He is also a member of IEEE, SPIE, IEB and a senior member of IACSIT.

Madeena Sultana received her M.S. and B.Sc. in Computer Science and Engineering from Jahangirnagar University, Savar, Dhaka, in 2011 and 2008, respectively. In October 2010, she joined the Dept. of Computer Science and Engineering (CSE) at the University of Liberal Arts Bangladesh. She was a Lecturer at the Dept. CSE of Northern University Bangladesh from June, 2008 to July, 2009. She has published a good number of papers in peer-reviewed international journals and conference proceedings. Her research interests include Pattern Recognition, Digital Image Processing, Computer Vision, and GPU Computing. She is a member of the International Association of Computer Science and Information Technology (IACSIT), Singapore.

Md. Ziarul Islam received his B.Sc degree in Computer Science and Engineering from State University of Bangladesh, in 2010 and M.Sc degree in Computer Science and Engineering from Daffodil International University in 2011. His research interests include Digital Image Processing, Artificial intelligence, Genetic Algorithm, Ad-hoc Networks, Cooperative Communication and Wireless Sensor Networks.

Design and Development of Microcontroller Based Portable Digital Surface Contamination Monitor

M. A. A. Mashud, M. R. A. Bhuiyan, M. A. Masud, Md. Serajul Islam

Abstract—The microcontroller based portable digital surface contamination monitor serves as a guide for evaluating workplace hazards caused by surface contamination. It also assists physicians in determining whether special protective measures for workers are necessary in contaminated areas. The system's design concept is useful for measuring surface contamination. In this design, a Geiger Muller detector with an ultra-thin mica window detects β radiation as well as γ radiation. A microcontroller PIC16F676 controls system function. A C language program was developed to control the function of the microcontroller, using PCWH Compiler. The reading is displayed in a seven segment display. It is user-friendly for specialists and non-specialists alike, and the device is easily decontaminated. The device's many advantages include its smaller size, on-device display, lower cost and improved portability.

Keywords—β-γ radiation, PIC16F676 microcontroller, PCWH Compiler, GM detector, low-cost, digital, nuclear medicine, radioactive material

1 Introduction

CONTAMINATION is defined [1] as the presence of undesirable radioactivity, either in the context of health or for technical reasons, such as increased background or interference with tracer studies. Contamination may result from radioactive gasses, liquids or particles. Radioactive contamination may exist on surfaces or in volumes of material or air. The design concept of a Portable Surface Contamination Monitor is very convenient to detect the surface contamination in the Nuclear Medicine Centers, Nuclear Reactor, Radioisotope Laboratories, Radioactive Waste Management, Industrial Environment and any other places where radioactive material is used.

Several radiation monitoring systems are designed locally in Bangladesh. A portable radiation survey meter using GM detector is explained in S. Islam et.al [2]. However this option cannot obtain a statistical analysis of digitally stored data, or any other form of analysis. The device's battery backup time is approximately 150 hours. The sensitive radiation survey meter as β-γ radiation monitor using scintillation detector NaI(TI) is explained in S. Islam et.al [3]. This device's battery backup time is approximately 180 hours. The above two systems are fully analog and a large number of components were used. However these systems are quite costly and complex in design.

We developed an alternative approach: a microcontroller based digital surface contamination monitor. The developed system has one detector that measures β-γ radiations. The battery backup time for our developed system is over 220 hours. The analog outputs of the GM-detector will be analysed and converted to digital data using a microcontroller. The BCD converts the digital data to the corresponding decimal number and display. Using readily available components and simple circuitry, the system is portable, low-cost, simple in design and fully digital.

2 Experimental Methods

The system is divided into three parts: the detector circuit, the microcontrolling unit and the display circuit. The detector circuit contains the GM tube and regulated high voltage power supply.

The analog output of the detector is converted into digital data using the microcontroller and fed into the BCD 7-segment decoder for display. The block diagram of the overall system and complete circuit diagram of the developed system is depicted in Figure 1 and Figure 2 respectively.

- *M. A. A. Mashud is with the Department of Applied Physics, Electronics and Communication Engineering, Islamic University, Kushtia-7003, Bangladesh. E-mail: ms.mashud@yahoo.com*
- *M. R. A.Bhuiyan is with the Department of Applied Physics, Electronics and Communication Engineering,Islamic University, Kushtia-7003, Bangladesh.*
- *M. A. Masud is with the Department of Computer Science and Information Technology, Patuakhali Science and Technology University, Dumki, Patuakhali, Bangladesh.*
- *Md. Serajul Islam is with the Institute of Electronics, Atomic Energy Research Establishment, Savar, Dhaka, Bangladesh.*

Manuscript received on 30 July 2011 and accepted for publication on 31 October 2011.

© 2011 ULAB JSE

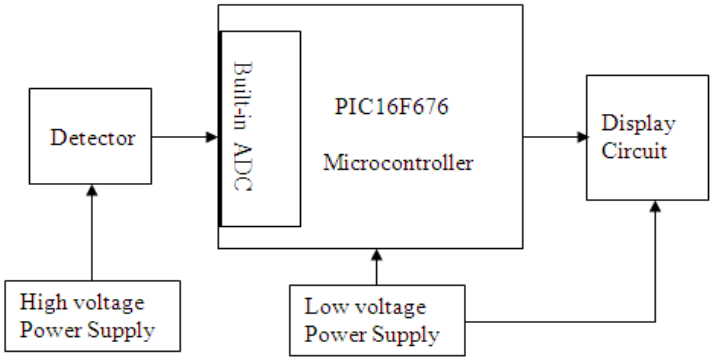

Figure 1: Block diagram of the developed system

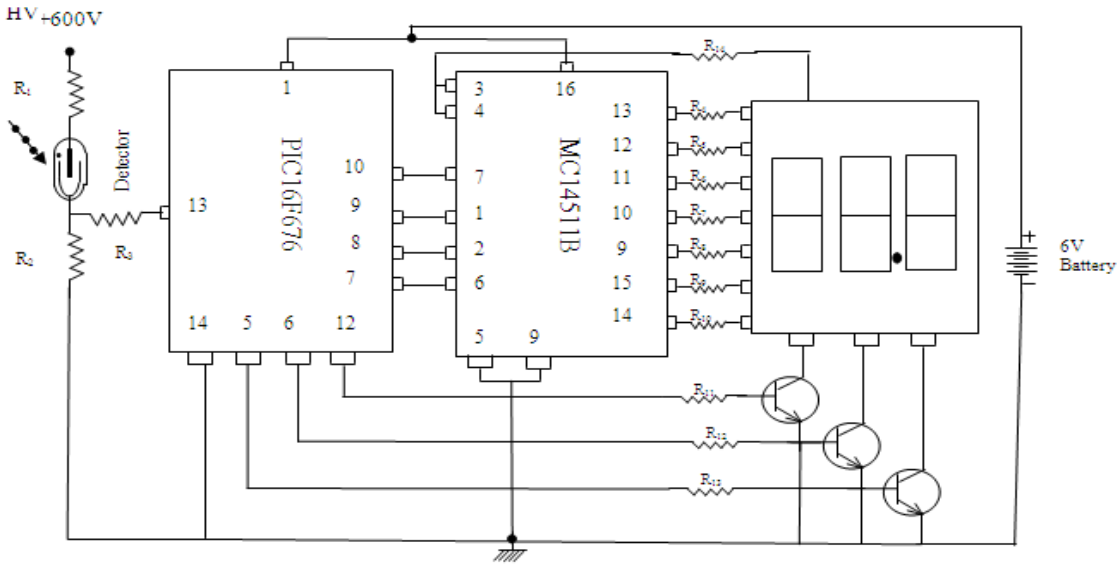

Figure 2: Complete circuit diagram of the developed system

2.1 The Detector Circuit

The common cathode detector [4] circuit was deployed in this work. The high voltage +600 volt [5] is connected to the anode of the detector through a current limiting resistor R_1. The resistor R_1 limits the current through the GM tube and assists advanced ionization to the quenched. The cathode of the detector is connected to the resistor R_2 and generated by the detection of radiation, which is fed to the microcontroller through resistor R_3.

2.2 Microcontroller Unit

The output of the detector is fed to the microcontroller PIC16F676 through resistor R_3. The microcontroller converts data from analog to digital, analysis data and display data. The pin diagram of the microcontroller is displayed in Figure 3.

The PIC16F676 is a 14-pin packages [6]. It has a 10-bit A/D converter and 32 MHz of processing speed [7], [8]. A "C" programming language was developed to control the microcontroller's function using PCWH Compiler [9].

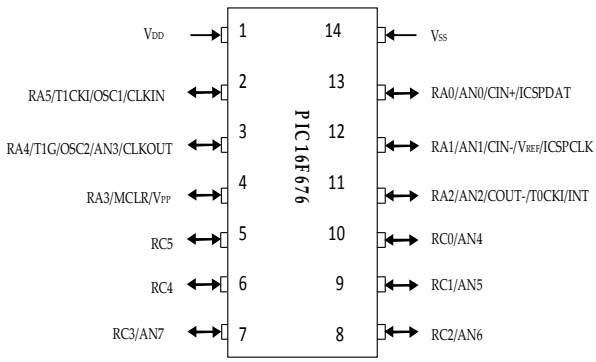

Figure 3: Pin diagram of PIC16F676 microcontroller

2.3 The Display Circuit

Three common cathode 7-segment LED modules display radiation value. When the pin of PIC microcontroller is used efficiently, the display is achieved by using a BCD 7-segment detector (MC14511B) [10]. The microcontroller sends the output signal to the input pins 7,1,2,6 of BCD-to- Seven-Segment Decoder, whose output pins13,12,11,10,9,15,14 are connected to the input of common cathode segment LED [11].

3 System Program

The system program and flow chart is depicted below:

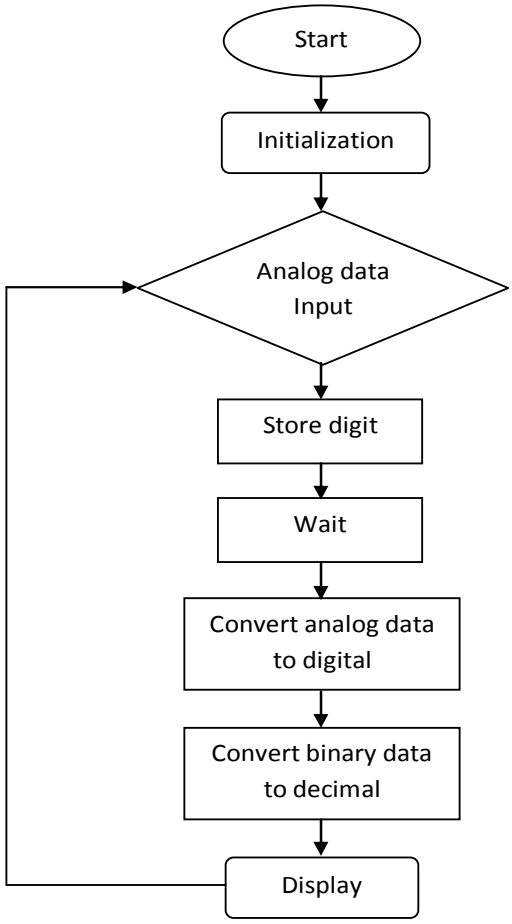

Figure 4: Flow chart of the system program

4 Results and Discussion

The system was successfully developed and its performance was strong. The system employed a local, low-cost PIC16F676 microcontroller. To avoid the complex comparator and A/D converter circuit, we used an internal comparator and A/D converter for the microcontroller. Furthermore, the internal frequency successfully avoided the external oscillator circuit. Thus the entire system function depends on the developed software. The circuit design is simple and compact.

Each output pulse from the GM tube was counted. Figure 5 depicts the counts per second and the corresponding Bq/cm² reading. The counts per second give an approximation of the radiation field.

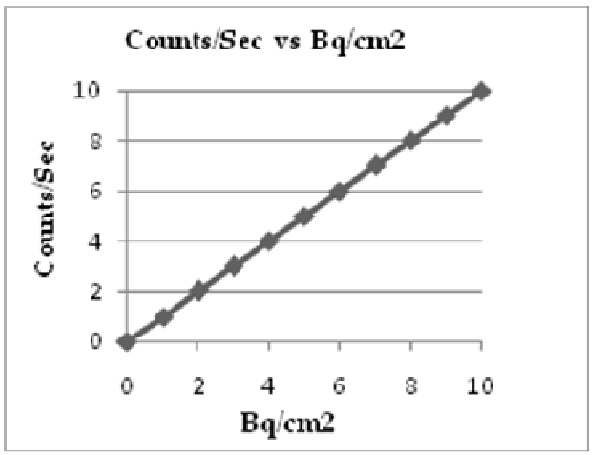

Figure 5: Counts/Sec vs Bq/cm^2 curve

The instrument underwent thorough tests, with satisfactory results. The system was calibrated using a radiation source from SSDL. Contamination linearly varies with count/s. The instrument detects the presence or absence of contamination on a sample surface.

The radiation survey meter currently being used in Bangladesh is fully analog and its cost is high. In contrast, our developed system is fully digital and its price is comparatively lower.

Several portable radiation survey meter devices available in the market were compared with the developed system, in terms of features, accuracy and cost. The comparisons are listed in Table 1.

TABLE 1

Comparison of other radiation monitoring devices with the developed system

	Portable Radiation Survey Meter[2]	Sensitive Radiation Survey Meter[3]	Developed System
Accuracy	± 10% of full scale deflection	± 10% of full scale deflection	± 2%
Module	Transistor	Transistor	Microcontroller
Measuring system	Analog	Analog	Digital
Battery life time for continuous use	Approx. 150 hours	Approx. 180 hours	More than 220 hours
Price (US$)	1500	1200	700

Table 1 demonstrates that the developed system is highly accurate. The cost is significantly lower than other systems with similar features. The specifications of the developed system are shown in Table 2.

TABLE 2
SPECIFICATIONS

Item	Description
Battery type	D-size, 1.5 volt (4 batteries)
Detector	CANBERA series 2000/8676
High Voltage	600 Volts dc
Measurement range	0 – 10 Bq/cm^2
Control system	Fully automatic control by micro-controller
Display	7-segment LED

5 CONCLUSION

In recent times, the cost of electronic equipment has fallen significantly, though nuclear equipment remains expensive. However due to the rapid development of micro electronics, all designed components and instruments are inexpensive. A Surface Contamination Monitor from the international market costs around US$ 2,000, while the price of the developed Portable Digital Surface Contamination Monitor is less than US$700. Moreover, when the features of the presently used system are compared with the developed system, the latter emerges as a better choice in terms of cost, portability and design. Particularly in developing countries, the use of the deigned instruments will be accessible for many users.

REFERENCES

[1] H. Cember "Introduction to Health Physics," second edition-revised and enlarge, Mc Graw-Hill, inc.332.

[2] S. Islam, H. Rahman and M. Aziz; Elect. Engg. Research Bulletin Vol. 4, No. 1, 15, 1988.

[3] S. Islam, A. Kiber and M. A. Taher; Nuclear Science and Applications, Vol. 1, No. 2, 12, 1989.

[4] Gerger Muller Tubes® Data Book, 36.

[5] S. Islam, Electronics For You, India, 113, 1989.

[6] DS40039C.pdf of Microchip Technology Inc.,PIC16F676 Datasheet, 1

[7] M. A. Mazidi, R. M. Kinlay & D. Causey; "PIC Microcontroller", Prentice Hall Inc., 24, 2008.

[8] J.B. Peatman; "Design with PIC microcontroller", Prentice Hall Inc., 2, 1997.

[9] PCWH Compiler IDE version 3.43, www.ccsinfo.com

[10] "Farnell Semiconductor Data CD-ROM," datasheet 6365001, Issue 7, January 2000.

[11] RS International Electronic Catalogue- March 2003.

M. A. A. Mashud was born on Nov.15, 1980 in kushtia, Bangladesh. He received the B.Sc. (Hons) degree in Applied Physics, Electronics and Communication Engineering (AECE) from Islamic University, Kushtia, Bangladesh in 2003, and M.Sc degree from the same department in 2004. He was a Lecturer in the department of Medical Physics and Biomedical Engineering at Gono Bishwabidyalay, Bangladesh from 2008 to 2010. He is currently a Lecturer in the department of AECE, Islamic University, Bangladesh. His current interest is microprocessor / microcontroller applications in control, automation, medical instruments, environmental monitoring, low cost electronic systems and assessment.

Dr. M. R. A. Bhuiyan was born on Dec.10, 1972 in Comilla, Bangladesh. He received the M.Sc. degree in Applied Physics and Electronics from Rajshahi University, Bangladesh in 1995, and Ph.D. degree from Islamic University, Kushtia, Bangladesh in 2008. He is currently an Associate Professor in the department of APE & Com. Engineering, Islamic University, Bangladesh. His current interest is thin-film solar cell and microcontroller based low cost electronic systems design. His work has produced nearly 25 peer-reviewed scientific International and National papers.

M. A. Masud was born on Nov. 08, 1982 in Meherpur, Bangladesh. He received the M.Sc. degree in Information and Communication Engineering from Islamic University, Kushtia, Bangladesh in 2004. He is an Assistant Professor in the department of Computer Science & Information Technology, Patuakhali Science and Technology University, Bangladesh. He works currently as a Ph.D. student in the School of Shinawatra University, Thailand.

Md. Serajul Islam was born in Panchagar, Bangladesh. He received the M.Sc. degree in Physics from Rajshahi University, Bangladesh. He was a Chief Scientific Officer and Director in the Institute of Electronics, AERE, Atomic Energy Commission, Savar, Bangladesh. Now he is retired. His work is design, development and analysis of electronic instruments and reactor control. His work has produced nearly 65 peer-reviewed scientific papers and 02 patents.

Performance Analysis of Different Propagation Models and the Correlation with Cellular Mobile Communication Systems

M. Mowrin Hossain and P. Mohan

Abstract—In this paper, the performance of different propagation models were analysed by calculating the variation of path loss with distances and frequencies. To correlate the propagation model with the wireless technique, a cellular communication system comprising five adjacent regions with actual population area and environmental conditions were considered. Path losses are increasing with the increase of distances and also depend on the systems where path losses are obtained from free spaces, flat earth and the ITU model. The value of path losses obtained from the Walfisch-Ikegami model is lower for the frequence of 900 MHz 1800 MHz. On the other hand, higher values of path losses were observed for Okumura-Hata and Lee's model. The Walfisch-Ikegami model is less dependent on distances and frequencies. The effective isotropic radiated power (EIRP) and coverage threshold was calculated using Hata-Okumura, Walfisch-Ikegami and Lee's model at 3 and 6 cell sectoring communication systems. The performance of the handoff mechanism was analyzed using the propagation model.

Keywords—Propagation model, Handoff, Path loss Eirp, coverage threshold.

1 Introduction

TODAY we live in the era of communication. The cellular concept of modern electronic communication was a major break through in solving spectral congestion and user capacity. It offers very high capacity in a limited spectrum allocation, without any major technological changes. It is essential for engineers to understand the propagation model in order to predict cellular communication systems[1]. The propagation model focuses on path losses between the transmitter and receiver during the period of propagating radio waves. Models are empirical in nature, which means they are developed by collecting extensive data for specific geographical and environmental scenarios.

Cellular mobile communication techniques are becoming increasingly popular. Cellular systems provide more channels per unit coverage area in terms of splitting and sectoring. The processing of handoffs is an important test in any cellular mobile radio system. Handoff must be performed as seldom as possible to avoid the "ping-pong" effect [2]. When a particular signal level is identified as the minimum acceptable range, it is established as the threshold at which handoff is made. The present work compares the performance of different propagation models. To correlate the propagation model with wireless techniques, the area comprising Rajshahi City Corporation and its adjacent upazila, Poba of Bangladesh was considered for developing a model as an example of cellular systems [3, 4]. The effective isotropic radiated power (EIRP) coverage threshold was calculated and the handoff strategies of this system were predicted using Hata-Okumura, Walfisch-Ikegami and Lee's model.

- *M. Mowrin Hassain, Dept. of Information & Communication Engineering, Rajshahi University, Rajshahi, E-mail: author@ boulder.nist.gov.*
- *P. Mohan, Dept. of Applied Physics, Electronics & Communication Engineering, Pabna Science & Technology University, Pabna. E-mail: author@colostate.edu.*

Manuscript received on 3 March 2011 and accepted for publication on 23 April 2011.

2 Analysis of Propagation Models

During the travelling of radio waves from transmitter to receiver, attenuation suffers as a result of propagation loss. Different propagation models are used to predict the above mentioned propagation loss. Different models were developed to understand propagation behavior in various environmental conditions [5].

Okumura-Hata, Walfisch-Ikegami and Lee's models are currently the most popular propagation model for predicting path loss. The Okumura-Hata model was developed in 1980 by Hata [6] and based on measurements reported by Okumura et al. [7] in 1968, and can be simplified for the use of a particular frequency [1] such as 900 MHz and the typical mobile antenna height of 1.5 meters to measure loss.

$$Loss = 146.8 - 13.82 \log h + (44.9 - 6.55 \log h) \log d \text{ -----} (1)$$

Digital mobile radio systems modify the model above for a typical frequency 1800 MHz [1] as follows:

$$Loss = 157.3 - 13.82 \log h + (44.9 - 6.55 \log h) \log d \text{ ----} (2)$$

Further progress was made by combining two separate models by Walfisch and Ikegami (COST-231). This involves an equation similar to the Okumura-Hata equa-

© 2011 ULAB JSE

tion, but also includes terms accounting for 'rooftop-to-street diffraction' and 'multi-screen diffraction'. The main advantage is that it retains validity even when the transmitting antenna is below the surrounding roof height. The predicted loss Walfisch-Ikegami model is demonstrated by the equation:

$$Loss = 42.6 + 20\log_{10}(f) + 26\log_{10}(d) \qquad \text{--------(3)}$$

Lee's path loss model was based on empirical data chosen as a flat terrain area. It is also known as "North American model" [10].

$$Loss = 107.7 + 38.4\log(d_1/1600) - 20\log(h_b/30) - 10\log(h_m/3) - g_{bs} - g_{mt} \qquad \text{----(4)}$$

Handoff initiation was also analyzed, using the above mentioned path loss models. The actual data for population and coverage area [3] were used for planning cellular systems in five different zones. The different parameters were calculated by considering 3 and 6 cell sectoring systems. The following simple link budget equation is used to calculate coverage threshold and effective isotropic radiated power (EIRP) [1];

$$Coverage\ \ Thershold\ \ (dBm) = EIRP - Path\ \ loss\ (dB) \qquad \text{-----(5)}$$

Traffic per subscriber is also calculated using the well known Erlang formula [8].

3 Results and Discussion

The performance of the free space, flat earth, ITU model, Egli model, ITU Terrain, and Young propagation models were analyzed by calculating path loss. Results demonstrate that the path loss is dependent on distance and system losses.

A comparison of the distance dependent path losses was obtained from calculated results produced by the Okumura-Hata, Walfisch-Ikegami and Lee's propagation models shown in figure-1 and figure-2 at 900 MHz and 1800 MHz respectively. The path loss dependent on the base and mobile station antenna height was also calculated.

It was found that the path loss increases with an increase in distance. On the other hand, it decreases when there is an increase in base and mobile station (antenna) height. Calculated results show that the path loss is totally dependent on environmental conditions and frequencies. The path loss is slightly dependent on frequency, in the case of the Walfisch-Ikegami propagation model. However it is heavily dependent on the frequency in Lee's model. The minimum propagation loss is obtained from the Walfisch-Ikegami model. It is approximately the same for Hata-Okumura and Lee's propagation model at the same distance and frequency (Fig-1, Fig-2).

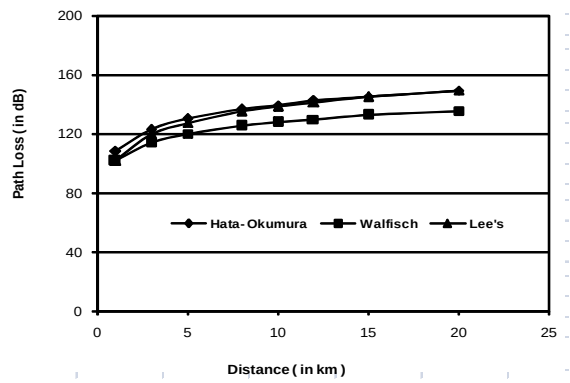

Figure 1: Performance analysis of distance dependent path loss at 900 MHz for Hata-Okumura, Walfisch-Ikagami and Lee's Model.

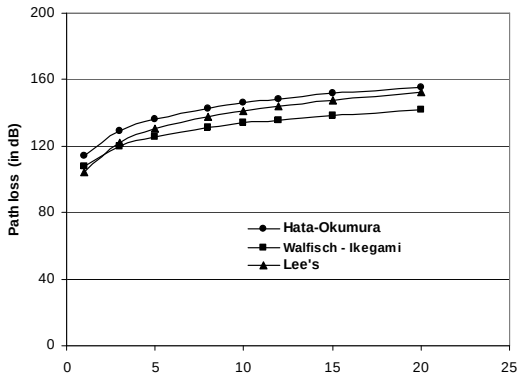

Figure 2: Performance analysis of distance dependent path loss at 1800 MHz for Hata-Okumura, Walfisch-Ikagami and Lee's Model.

An analysis of handoff initiation is contained in figure-3. The result was obtained using different path loss models, such as the Okumura-Hata, Walfisch-Ikegami and Lee's models. This figure shows that the Handoff occurs at a lower distance for Okumura-Hata model than Walfisch-Ikegami model. It occurs in Lee's model at a further distance than the other two models.

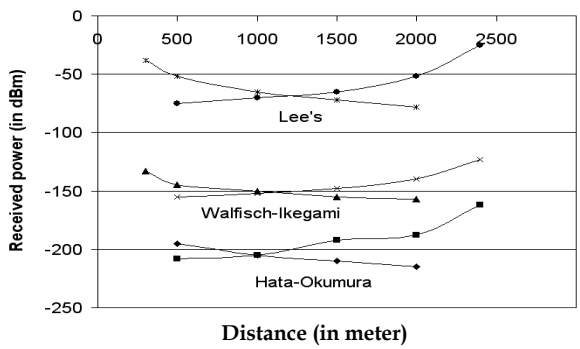

Figure 3: Performance analysis of handoff mechanism by using different propagation models

The method of analyzing path loss is vital for predicting the cellular communication system. It was observed that the effective isotropic radiated power (EIRP) and coverage threshold of the cellular system is easily calculated by using different propagation models. The path loss is also dependent on cell radius. The cell radius dependent path loss at three sectoring cellular system is shown in figure-4. The path loss was obtained by using different propagation models. Path loss increases as the radius increases. The path loss obtained from Walfisch-Ikegami and Lee's models are approximately the same. Conversely, the value is higher in the case of the Okumura-Hata model (Fig-4)

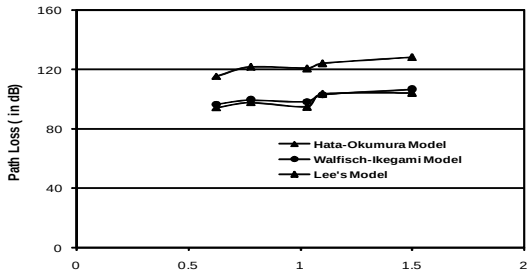

Figure 4: Perfomance analysis of cell radius dependent path loss at 3 cell clusters cellular system for Hata-okumura, Walfisch -Ikegami and Lee's model.

Cell-radius dependent effective isotropic radiated power (EIRP) is shown is figure-5 and figure-6 for three and six sectoring cellular systems respectively. It is evident from the results that the values of EIRP calculated by using Walfisch-Ikegami and Lee's propagation model is negligible within the cell-radius of 1.03 km for three sectoring system. On the other hand, it is within 0.88 km for six sectoring system.

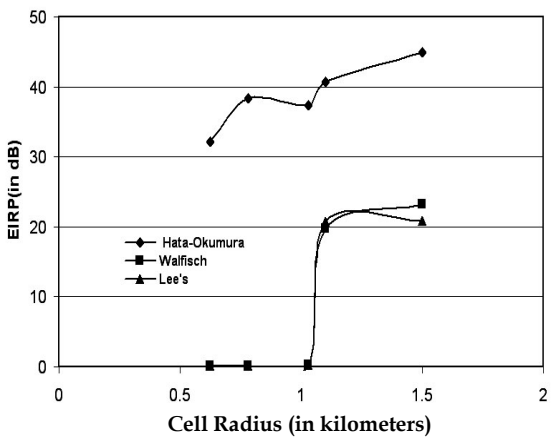

Figure 5: Performance analysis of cell radious dependent EIRP at 3 sector cellular system was calculated using Hata-okumura, Walfisch-Ikegami and Lee's model.

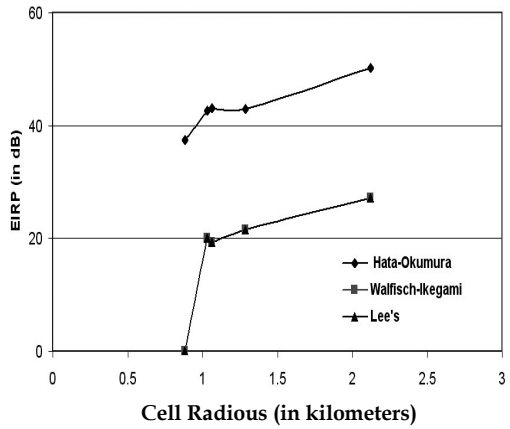

Figure 6: Performance analysis of cell radious dependent EIRP at 6 sector cellular system was calculated using Hata-okumura, Walfisch-Ikegami and Lee's model.

4 Conclusion

The path loss calculated using different propagation model varies with distance, frequency and environmental factors. The data analysis confirms that the path loss calculated by Walfisch-Ikegami model is lower and less dependent on distance. Lee's model is preferable for calculating long distance handoff mechanisms. By contrast, the Okumura-Hata model may be used for short distance communication systems. We may also conclude that the Hata-Okumura propagation model is appropriate for the region of cellular systems, as proposed in this paper. The effective isotropic radiated power (EIRP) and coverage threshold are dependent on the radius of the cell for mobile communication techniques.

References

[1] Christopher Haslett, "Essentials of Radio wave propagation," Cambridge University press, pp. 26-48, 2008.

[2] Kamil Sh. Zigangirov (2004) "Theory of code division multiple access communication", A Jonn Wiley and Son's, Inc. Publication.

[3] Population Census, "Community Series, Rajshahi", Bangladesh Bureau of Statistics, 2001.

[4] M. Mowrin Hossain, et. al. "A proposed cellular link for Bangladesh", *CMARS*, 9th-11th Dec. Jodhpur, India, pp. 120-121, 2008.

[5] M.M. Hossain et. al, "Analysis of Large-Scale propagation Models for Mobile communications in Arban Area," *International Journal of Computer Science and Information Security*, vol-7, no-1, pp. 135-139, 2010.

[6] Hata, M., "Empirical formula for propagation loss in land mobile radio service," *IEEE Transaction on Vehicular Technology*, 29, pp. 317-325, 1980.

[7] Okumura et. al., "Field strength and its variability in VHF and UHF land-mobile service," *Review of the Electrical Communication Laboratory*, 16, pp. 825-873, 1968.

[8] Parkinson, R, "Traffic Engineering Techniques in Tele Commu-

nication," Infotel systems Inc, 2005.

[9] Dongroo Har et. al, "comment on diffraction loss of roftop-to-street in COST 231-Walfisch-Ikogami model", *IEEE Transaction on Vehicular Technology*, vol. 48, no. 5, pp. 1451-1452,1999.

[10] Anderson, H.R, "A ray-tracing propagation model for digital broadcasting systems in urban areas", *IEEE Transaction on Broadcasting*, vol-93, no-3, pp. 309-317, 1993.

M. Mowrin Hossain has completed MSc and BSc in Information & Communication Engineering at University of Rajshahi, Rajshahi. Currently serves as a Lecturer of department of Computer Science, University of Information Technology & Science, Rajshahi Branch, Rajshahi.

U. P. Mohan has completed MSc and BSc in Information & Communication Engineering at University of Rajshahi, Rajshahi. Currently he is a Lecturer in the department of Applied Physics, Electronics & Communication Engineering at Pabna Science & Technology University, Pabna.

Feature Extraction Clustering in Text Mining using NMF Basis Probability

Paresh Chandra Barman, Md. Sipon Miah, Bikash Chandra Singh

Abstract—It is obvious that unlabeled document or text collections are becoming increasingly larger. However mining this data is a challenging task. Using the simple word-document frequency matrix as feature space makes the mining process more complex. As text documents are commonly represented as high dimensional, a few thousand sparse vectors have a sparsity of about 95 to 99%. This paper proposes the document feature extraction and clustering method, based on the probability of Non-negative Matrix Factorization (NMF) basis vectors. Due to the nature of part-based feature selection, NMF algorithm significantly reduces the dimension of the feature vectors of word-document frequency from a few thousand to a few hundred to successfully cluster the documents. The performance of the dimension deduction and clustering has been observed for the Classic3* dataset.

Keywords— NMF, CISI, MED, CRAN

1 INTRODUCTION

TEXT Miming discovers useful knowledge or patterns from unstructured or semi-structured text. The clustering or categorizing of text documents is a fundamental part of the text mining process. Over the last few years, the amount of textual information available on the World Wide Web, corporate intranets and news wires has grown exponentially. While the amount of textual data is constantly increasing, our ability to process and utilize this information remains largely unchanged. One of the greatest challenges facing information science and technology is to develop algorithms and software that can efficiently organize, access and mine such a vast amount of information.

Feature extraction from the huge amount of textual data is important for achieving an efficient algorithm to categorize unstructured text data. A large amount of research has focused on reducing the dimensions of the document feature vector. In this paper, we focus on reducing the document feature vector and clustering natural language documents into a pre-defined set of topical categories, commonly referred to as document clustering. Document clustering is an enabling technology that is essential for many information processing applications.

- *P C Barman, Associate Professor, Dept. of Information & Communication Engineering, Islamic University, Kushtia-7003. E-mail: head@iceiu.info.*
- *Md. Sipon Miah, Lecturer, Dept. of Information & Communication Engineering, Islamic University, Kushtia-7003. E-mail: mdsiponmiah@gmail.com.*
- *Bikash Chandra Singh, Lecturer, Dept. of Information & Communication Engineering, Islamic University, Kushtia-7003. E-mail: bikashsingh18@yahoo.com*

Manuscript received on 30 July 2011 and accepted for publication on 31 October 2011.

The NMF algorithm was successfully deployed for semantic analysis [1]. Xu et al. (2003) demonstrated that NMF outperforms other methods, such as singular value decomposition and it is comparable with graph partitioning methods, K-mean clustering [3-12], probabilistic clustering using the Naive Bayes or Gaussian mixture model [1, 9] etc. F Shahnaz et al. (2004) cluster text documents by imposing sparsity constraints into the NMF algorithm. This sparsity constraint creates a slow convergence of the algorithm.

Another related line of research is the simultaneous clustering approach. I. S. Dhillon et al (2003) compare the efficiency of one dimensional clustering and information theoretic co-clustering of joint probability distribution of two random variables or co-clustering, Zha et al., (2001) to reduce the dimensionality of feature vectors. Data instances and their attributes are simultaneously clustered to enhance the effectiveness of clustering and interpretability. However the simultaneous clustering approach focuses on a fixed set of documents, and therefore, strictly speaking, it fails to provide a generative model for arbitrary documents. Jia Li et al (2004) use the two-way Poisson mixture models to reduce the dimension of document feature vectors. A common approach associated with these methods is the consideration of the whole document collection. This provides a highly dimensional document feature vector as the starting point.

The general paradigm involves term-frequency document matrix to represent text documents. The elements of matrix $V = [v_{ij}]$ where v_{ij} is the term frequency i.e., the number of times word i occurs in document j. Each document in a collection is represented by an n-dimensional vector. For a collection of documents covering several topical classes, it commonly uses a large number of words, leading to a large vocabulary size, and all document vectors occupy a high-dimensional space. Alternatively, the number of distinct words in any single

© 2011 ULAB JSE

document is usually substantially less than the size of the vocabulary, leading to sparse document vectors and vectors with numerous zero components. High dimensionality and sparsity pose a challenge to many classification algorithms.

Our approach involves randomly selecting documents from the text collection and finding the term-frequency document matrix V as a starting point. Using NMF, we find a medium dimensional feature vector in each class. The term index of the basis vectors, as obtained by the NMF algorithm, is random probability distribution. By rearranging the term indices, we convert random distribution as Poisson probability distribution and calculate the probability rank of each NMF basis vector. Using a threshold on the rank of basis-probability, we selected the most significant basis vectors. As a result, very small dimensional feature vectors were obtained. The small dimensional feature vectors are used throughout the document collection for clustering or classification framework, again using the NMF algorithm.

2 Overview of the NMF Algorithm

Given a non-negative n x m matrix V; find non-negative factors, W, of n x r matrix, and H, r x m, such that: V ≈ WH or

$$V_{ij} \approx (WH)_{ij} = \sum_{a}^{r} W_{ia} H_{aj} \quad \text{.....(1)}$$

Where r is chosen as $r < nm/(n+m)$

- V is the word-frequency matrix
- W is basis feature matrix;
- H is encoded matrix and it is one-to-one correspondence with a sample of V.

The update of W & H are as follows [1],[8]

$$H_{kj}^{(n+1)} = H_{kj}^{(n)} Q_D\left([W^{T(n)}]_{ki}, \frac{V_{ij}}{[W^{(n)} H^{(n)}]_{kj}} \right)_{kj} \quad \text{.....(2)}$$

$$W_{ik}^{(n+1)} = W_{ik}^{(n)} Q_D\left(\frac{V_{ij}}{[W^{(n)} H^{(n+1)}]_{ij}}, [H^{T(n+1)}]_{jk} \right)_{ik} \quad \text{.....(3)}$$

$$W_{ik}^{(n+1)} \leftarrow \frac{W_{ik}^{(n+1)}}{\sum_i W_{ij}^{(n+1)}} \quad \text{.....(4)}$$

Where $Q_D(A,B)_{ij} = \sum_k A_{ik} B_{kj} = AB$, and all the $(.)_{ij}$ indicates that the noted division and multiplications are computed element by element.

2.1 Proposed NMF model

Our overall model is shown in figure 1. The text documents box represents the collection of raw documents. The preprocessing steps remove common words. NMF feature extractor step extracts the text features of a moderate dimension. The feature selection step selects significant features, based on their probability rank and so reduces the feature dimension. This small dimensional feature set is then used to extract features for the rest of the documents. Finally, the 2nd NMF step clusters the documents.

2.2 Text document

In order to justify the proposed approach, Classic3 document corpus is considered. The corpus consists of 3,891 abstracts of three separate journal articles. The distribution of the articles is as follows:

- MEDLINE: 1,033 abstracts from medical journal.
- CISI: 1,460 abstracts from information retrieval journal.
- CRANFIELD: 1,398 abstracts from aeronautical systems papers.

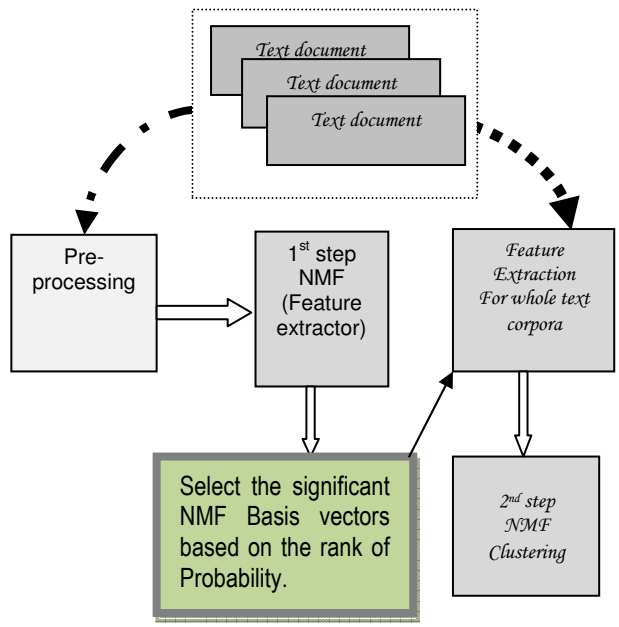

Figure 1: Text Document clustering process using NMF algorithms.

2.3 Pre-processing

This step involved filtered out certain English stop words (sample list [3]) such as "the" and "to." The numerical values and special characters include <, =, etc. After removing the words or characters, 301,808 words remained in the whole corpus.

2.4 NMF Feature extractor

This step involved randomly selecting 600 documents (around 200 documents from each type of journal) from 3,891 documents of the corpus. We then used the term-document frequency vector to represent each document. Let $wd = \{w_1, w_2, ..., w_m\}$ be the complete vocabulary set of the 600 documents. The term-document frequency

vector v_i of document d_i, is defined as $v_i = [v_{1i}, x_{2i}, ..., x_{mi}]^T$ where x_{ji} represents the frequency of the word j in document i. In this case m=7972 and i=1, 2, 3… 600. As we know, there are three types of documents. By using NMF, the vocabulary set was segmented into three basis feature vector W_c, as shown in figure 2. Basis vectors are random probability distribution of words or terms corresponding to the documents. $W_c = [w_{1c}, w_{2c}, ..., w_{mc}]^T$ where c= 1, 2, 3. w_{jc} be the jth word in the basis feature vector c. We rearranged each basis vector index j and normalized it to create a Poisson-like probability distribution to define NMF basis-probability distribution. Applying a threshold value on each basis-probability distribution, we found the indexes of the most probable words or terms for each cluster or class. Using these indexes, we created a reduced vocabulary set. Thus, we significantly reduced the dimension of each feature vector.

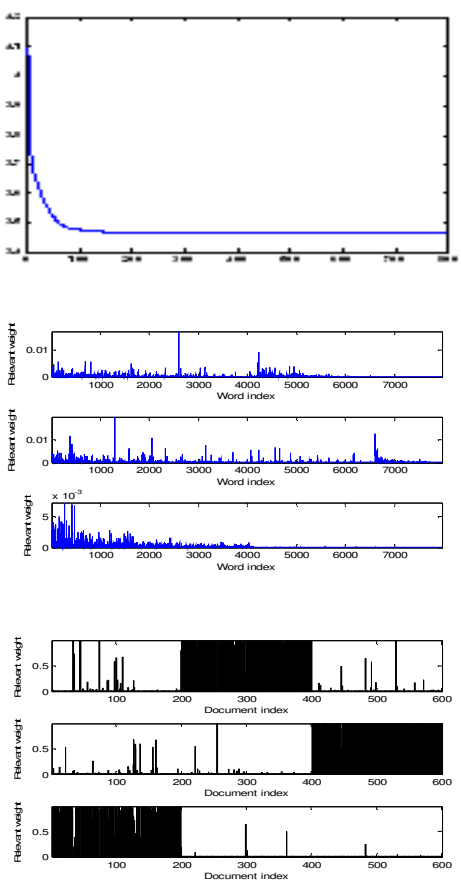

Figure 2: Prior to reducing the dimension of vocabulary size. The left figure shows the learning curves; X-axis represents the number of iteration (800); Y-axis the KL divergence value. The medial figure shows the basis feature for 600 documents; X-axis is the word index of the vocabulary set (7972); Y-axis is the relative weight or strength of the words corresponding with the feature vectors. The figure on the right shows the relevant strength of the documents to the clusters. X-axis is the documents indices and the Y-axis is the relative weight of the documents to the clusters.

2.5 Feature Extraction for whole text corpora

Using this reduced vocabulary set, we extract the word-document frequency feature matrix for the whole corpus in order to cluster whole documents or classify new documents, which is relevant to this document collection. Now the word-frequency vector V_i of document d_i, is defined as $V_i = [x_{1i}, x_{2i}, ..., x_{mi}]^T$ where x_{ji} represents the frequency of the word j in document i, in this case: i=1 to 3891, and j=1, 2… reduces vocabulary size.

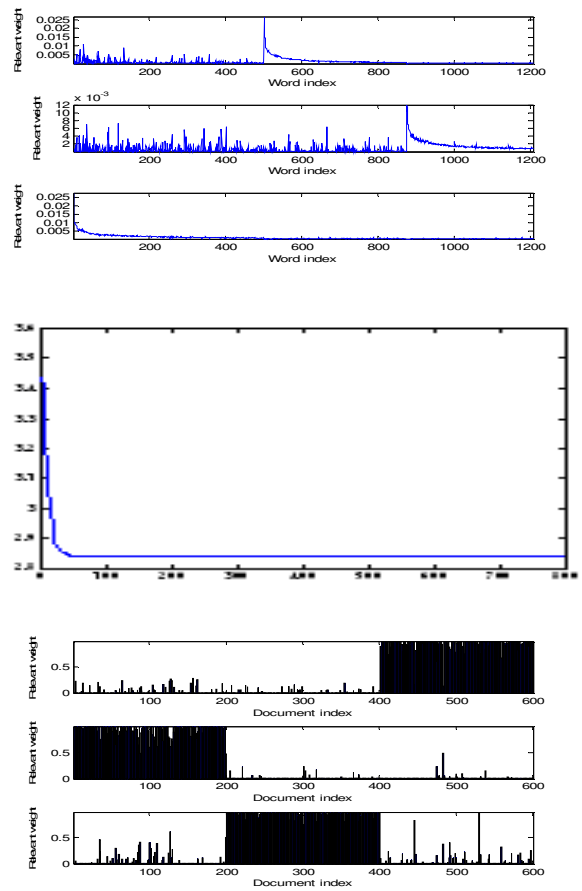

Figure 3: After the vocabulary size was reduced. The left figure shows the learning curves; X-axis represents the number of iteration (800); Y-axis the KL divergence value. The medial figure shows the basis feature for 600 documents; X-axis is the word index for the vocabulary set (1206); Y-axis is the relative weight or strength of the words corresponding to the feature vectors. The right figure shows the relevant strength of the documents to the clusters. X-axis is the documents indices and the Y-axis is the relative weight of the documents to the clusters.

2.6 Second step NMF (Clustering)

Here, we again factorize the new word-frequency matrix V into two factors: W (the basis weight matrix) and H (the encoding matrix). The encoding matrix H of dimension r×m, (where r is the number of clusters and m is the number of

documents) was used to cluster the documents. We normalize the encoding matrix H, as shown in the pseudo-codes of NMF. Each row depicts the relevant probability of documents corresponding with the cluster. This paper considers the maximum probability for clustering the documents.

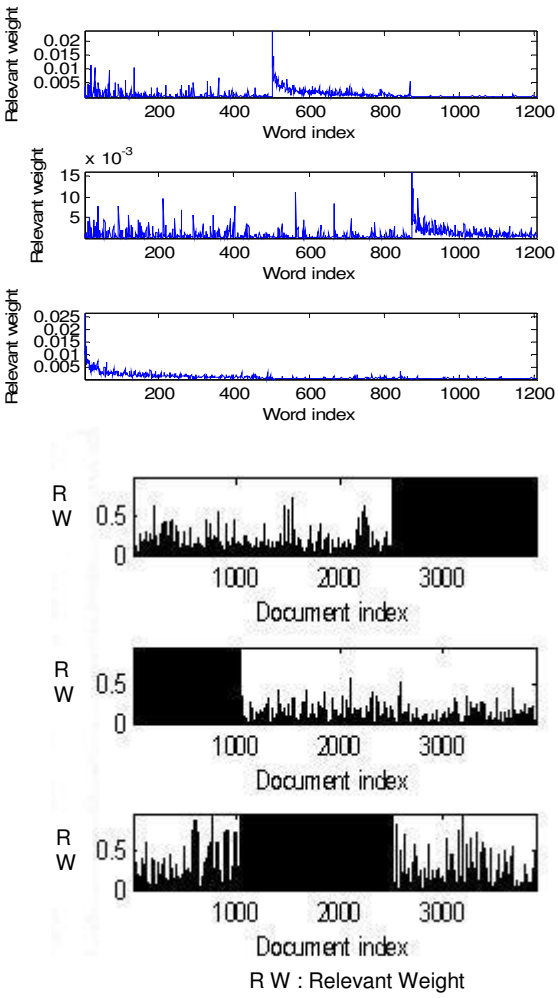

Figure 4: The top figure shows the three basis feature for whole documents. The X-axis represents the word index of the vocabulary set (1206); the Y-axis is the relative weighs or strength of the words corresponding to the feature vectors. The bottom figure illustrates the relevant strength of the documents to the clusters. The X-axis is the documents indices and the Y-axis is the relative weight of the documents to the clusters.

3 RESULTS

The graphic representation of learning curves, semantic feature W, and clustering or encoding matrix H are shown in figure 4. Clustering performance of the training documents are shown in Table-1.

TABLE 1

CLUSTERING RESULTS FOR 600 DOCUMENTS (200 FROM EACH CATEGORY) OF THE CLASSIC3 TEXT DATABASE

	Clustering before reducing the vocabulary set			Clustering after reducing the vocabulary set		
CISI	196	2	2	200	0	0
MED	11	182	7	3	197	0
CRAN	3	0	197	2	1	197
	Accuracy = 95.8%			**Accuracy = 99%**		

TABLE 2

THREE SEMANTIC FEATURES OF A TOTAL OF 1,206 WORDS, ONLY THE TOP 20 FOR EACH BASIS SEMANTIC FEATURE ARE SHOWN.

Semantic Feature for CRAN doc	**Semantic Feature for MED doc**	**Semantic Feature for CISI doc**
flow	patients	information
pressure	cells	library
boundary	cases	system
results	growth	research
theory	treatment	data
layer	normal	libraries
number	result	systems
method	present	can
mach	found	book
shock	during	retrieval
solution	case	science
heat	blood	scientific
obtained	cell	study
wing	human	problems
surface	disease	user
equations	effect	paper
temperature	changes	such
presented	renal	literature
effects	rats	subject
supersonic	cancer	between

TABLE 3

CLUSTERING RESULTS FOR THE CLASSIC3 TEXT DATABASE

	Clustering for all 3,891 documents		
CISI	1452	2	6
MED	35	993	5
CRAN	19	1	1378
	Accuracy = 98.25%		

Post-processing: In this step we attempt to determine the correlation among the documents and semantic features.

- A graphic representation of this correlation is shown in figure 5.
- Semantic feature or information: The three semantic features are shown in figure 2.
- Clustered documents are shown in table 3.

4. Conclusion and Future Works

As the feature of the text data is sparse, the majority of the word-frequency matrix is zero and mainly depends on the number of unique words in the vocabulary set.

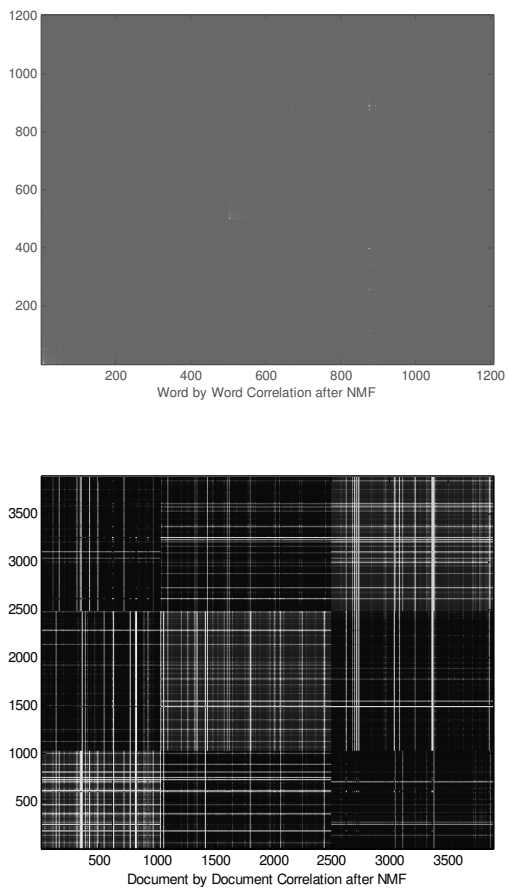

Figure 5.1: Correlation between different factors: the top figure represents the correlation among the words ($W \times W^T$); the bottom figure represents the correlation among the documents ($H^T \times H$).

The many non-significant words do not significantly contribute to clustering the documents. NMF is a simple and effective algorithm to reduce the dimension of feature vectors of text data. It is also a simple and adaptive algorithm for document clustering. The learning time and memory reduces significantly after reducing the dimension and increases clustering efficiency.

In this paper we present only hard-clustering. In future, we will include soft-clustering, which means that one document could be members of more than one cluster. We will also attempt sub-clustering (tree-like clustering) the documents. This paper has extracted only three semantic features, but in the near future we will extract further small parts of semantic features. We will also use text-base user identification to create an intelligent office-assistant system.

Acknowledgements

We are grateful to BSRC for its financial support for undertaking this work, and thank all Lab members of CNSL for their creative suggestions during lab-meetings and seminars.

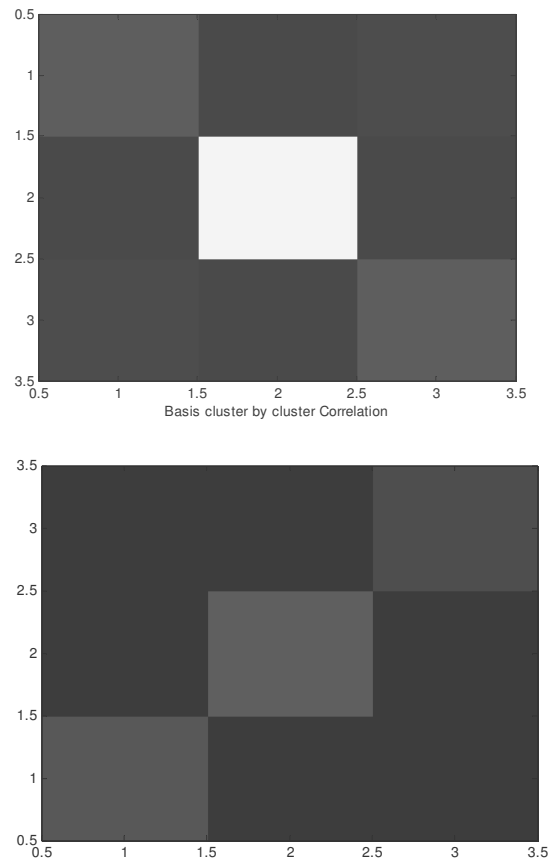

Figure 5.2: The top figure represents the correlation among the basis features ($W^T \times W$); and the bottom figure represents the correlation among the clusters ($H \times H^T$).

References

[1] D. D. Lee and H. S. Seung. **Learning the parts of objects by non-negative matrix factorization**. *Nature*, 401(6755):788–791, 1999.

[2] D. D. Lee and H. S. Seung. **Algorithms for non-negative matrix factorization**. In *Advances in Neural Information Processing 13 (Proc. NIPS*2000)*. MIT Press, 2001.

[3] http://www.perseus.tufts.edu/Texts/engstop.html

[4] Marti A. Hearst; Untangling Text Data Mining School of Information Management & Systems University of California, Berkeley 102 South Hall Berkeley, CA 94720-4600. *http://www.sims.Berkeley.edu/-hearst*

[5] Farial Shahnaz and Michael W. Berry; Document Clustering Using Nonnegative Matrix Factorization; Journal on Information Processing & Management; Elsevier-2004.

[6] W. Xu, X. Liu, and Y. Gong. Document-Clustering based on Non-Negative Matrix Factorization. In proceedings of SIGIR'03, July 28-August 1, pages 267–273, Toronto, CA, 2003.

[7] H. Zha, C. Ding, M. Gu, X. He, and H. Simon. Spectral relaxation for k-means clustering. In Advances in Neural Information Processing Systems, Volume 14, 2002.

[8] Inderjit S. Dhillon, Subramanyam Mallela, Dharmendra S. Modha; Information-Theoretic Co-clustering, SIGKDD '03, August 24-27, 2003, Washington, DC, USA.

Dr. Paresh Chandra Barman received a Bachelor's, Master's degree in Applied Physics & Electronics from Rajshahi University, Rajshahi, in 1994 and1995 respectively. He received the Ph.D. degree from the department of Bio and Brain Engineering from Korea Advanced Institute of Science and Technology (KAIST) in 2008. Currently, he is an Associate Professor at the Dept. of Information & Communication Engineering, Islamic University, Kushtia, Bangladesh. His research interests include Neural Network Theory & Application, Pattern Recognition, Artificial Intelligence & Expert Systems, Mathematics for Engineering, Statistics for Communication Engineering, Calculus & Differential Equations and Bioinformatics.

Md. Sipon Miah received a Bachelor's and Master's Degree from the Department of Information & Communication Engineering from Islamic University, Kushtia, in 2006 and 2007, respectively. He is currently a Lecturer at the department of ICE, Islamic University, Kushtia-7003, Bangladesh. Since 2003, he has served as a Research Scientist at the Communication Research Laboratory, Department of ICE, Islamic University, Kushtia, where he is a member of a spread-spectrum research group. He is pursuing research in internetworking in wireless communication. He has published eight papers in international journals and one in a national journal in the same areas. His areas of interest include database systems, optical fiber communication, Spread Spectrum and mobile communication.

Bikash Chandra Singh received the B.Sc and M.Sc degree in Dept. of Information & Communication engineering from Islamic University, Kushtia, Bangladesh, in 2005 and 2006 respectively. Currently, he is a Lecturer at the Dept. of Information & Communication Engineering, Islamic University, Kushtia, Bangladesh. He is pursuing research in the area of wireless communication. He has published eight international journal papers and one international Conference paper in communication field. His interests are in Wireless Communication, Network Security, WiMAX, and Sensor Network.